Report DCW-R-07-01

COMPUTATION OF TURBULENT BOUNDARY LAYERS ON CURVED SURFACES

by

D.C. Wilcox and T.L. Chambers

January 1976

Prepared under Contract No. NAS2-8884 by

DCW Industries
Sherman Oaks, California 91423

for

AMES RESEARCH CENTER
NATIONAL AERONAUTICS AND SPACE ADMINISTRATION

FOREWORDWORD

Results of research performed in Contract NAS2-8884 during the period June 1, 1975, through January 31, 1976, are presented. The study was sponsored by the NASA Ames Research Center; the NASA Technical Managers were M. Rubesin and J. Marvin. Study participants were D. C. Wilcox, principal investigator, T. L. Chambers and R. M. Traci. Manuscript preparation was accomplished by J. A. Jessup.

ABSTRACT

An accurate method has been developed for predicting effects of streamline curvature and coordinate system rotation on turbulent boundary layers. A new two-equation model of turbulence has been developed which serves as the basis of the study. In developing the new model, physical reasoning is combined with singular perturbation methods to develop a rational, physically-based set of equations which are, on the one hand, as accurate as mixing-length theory for equilibrium boundary layers and, on the other hand, suitable for computing effects of curvature and rotation. The equations are solved numerically for several boundary layer flows over plane and curved surfaces. For incompressible boundary layers, results of the computations are generally within 10% of corresponding experimental data. Somewhat larger discrepancies are noted for compressible applications, although the overall level of accuracy is obscured by uncertainties in the experimental data. Results of the study lend further confidence to the notion that curved streamline effects can be accurately predicted with second-order closure of the turbulent-flow equations of motion.

CONTENTS

NOTATION

SYMBOL	DEFINITION
B	Constant in the law of the wall
c_f	Skin friction
$c_D, c_m, c_p, c_w, c_\omega, c_1, c_2$	Parameters in turbulence model equations
e	Specific turbulent mixing energy
E	Nondimensional mixing energy
F	Nondimensional streamfunction (Eq. 12)
k	Roughness height
L	Reference length
M	Mach number
p	Static pressure
P_ω	Production term in dissipation-rate equation
R	Radius of curvature
$Re_x, Re_\theta, Re_{\delta^*}$	Reynolds number based on plate length, momentum thickness, displacement thickness
Re_T	Turbulent Reynolds number
S	Surface-roughness function
S_t	Stanton number
T	Static temperature
u	Velocity component in x direction
U_e, U_∞	Boundary-layer-edge velocity, freestream velocity
v	Velocity component in y direction

NOTATION (continued)

SYMBOL	DEFINITION
W	Nondimensional dissipation rate
x	Coordinate lying along a solid body
y	Coordinate normal to a solid body
α, α^*	Parameters in turbulence model equations
$\alpha_\infty, \alpha_\infty^*$	Values of α, α^* for fully turbulent flows
α_T	Similarity parameter in defect-layer solution
β, β^*	Parameters in turbulence model equations
β_T	Similarity parameter in defect-layer solution
δ, δ^*	Boundary-layer thickness, displacement thickness
ε	Kinematic eddy viscosity
ε_d	Dissipation function
η	Similarity variable for the defect layer
θ	Momentum thickness
κ	Karman constant
λ	Parameter in turbulence model equations
μ	Molecular viscosity
ν	Kinematic viscosity
ξ	Similarity variable for the defect layer
ρ	Fluid mass density
$\sigma, \sigma^*, \sigma_e, \sigma_z, \sigma_\varepsilon$	Parameters in turbulence model equations
σ_T	Similarity parameter in defect-layer solution

NOTATION (concluded)

SYMBOL	DEFINITION
ϕ	Angle from centerline for cylindrical body
$\bar{X}$	Parameter in turbulence model equations
ψ	Streamfunction
Ψ	Constant in initial profiles
ω	Turbulent dissipation rate
ω_T	Similarity parameter in defect-layer solution
Ω	Specific turbulent dissipation rate; angular velocity of a rotating coordinate system
ℓ	Turbulent mixing length

Subscripts

e	Boundary-layer edge
w	Body surface

1. INTRODUCTION

In a prior study, Wilcox and Chambers[1] found that the magnitude of streamline curvature effects on turbulent boundary layers can be predicted reasonably well with second order closure of the turbulent flow equations of motion. The study showed that streamline curvature and coordinate-system rotation effects can be understood on a fairly fundamental basis only by considering the interactions of the various components of the Reynolds stress tensor and the mean flow. Hence, most of the effort focused upon developing a turbulence model based on the Reynolds stress equation (RSE). The most important result of the Wilcox-Chambers study is the straightforward physical interpretation of streamline-curvature effects inferred from the analysis. As a brief review, the RSE model predicts that for boundary-layer flows the following things are true:

1. In equilibrium the Reynolds shear stress is proportional to the normal Reynolds stress perpendicular to the plane of shear, $\langle v'^2 \rangle$.

2. $\langle v'^2 \rangle$ is strongly affected by streamline curvature and system rotation.

3. The large changes in $\langle v'^2 \rangle$ occur mainly because of RSE transformation properties and pressure-strain correlation terms.

While other researchers have suggested that $\langle v'^2 \rangle$ plays a key role in curved-surface boundary layers, no one previously demonstrated that curvature effects can be accurately predicted by accounting for changes in $\langle v'^2 \rangle$ caused by curvature.

As a corollary result of the study, understanding of curvature/rotation effects gained from analyzing the RSE model led to improvement of the simpler Saffman[2] two-equation turbulence model. Because of its inherent simplicity (relative to the RSE model), the two-equation model appears to have the best potential for serving as an engineering design tool.

While these developments are most encouraging, results of numerical applications of the RSE model and the Saffman two-equation model leave something to be desired. For example, Figure 1 compares computed and measured[3,4,5,6] velocity profiles for two equilibrium boundary layers with adverse pressure gradients. Both the RSE and Saffman models yield inflected profiles in the defect-layer portion of the boundary layer. Since for equilibrium boundary layers the RSE model reduces almost identically to the Saffman model, it is unsurprising that both models yield the same curious inflections. With the models performing so poorly for equilibrium boundary layers, it is difficult to generate much confidence in model predictions for such complicated effects as those of curvature and rotation. In the present study, application of the RSE model to flow over a segmented spinning body (see Appendix) further demonstrates the RSE model's deficiencies in the defect layer.

The objective of the present study has been to identify and eliminate the source of inaccuracy in the Saffman model. Since the Saffman model serves as the foundation upon which the RSE model is built, elimination of deficiencies in the Saffman model should lead to improvement of the RSE model. The study consists of two segments. The first segment (Section 2) focuses primarily upon two-equation-model defect-layer structure and equilibrium (plane-surface) boundary-layer applications; a new baseline two-equation model is developed. Then, in Section 3, with suitable curvature-rotation modifications the baseline model equations are solved numerically for several boundary-layer flows over curved surfaces. Section 4 discusses study results.

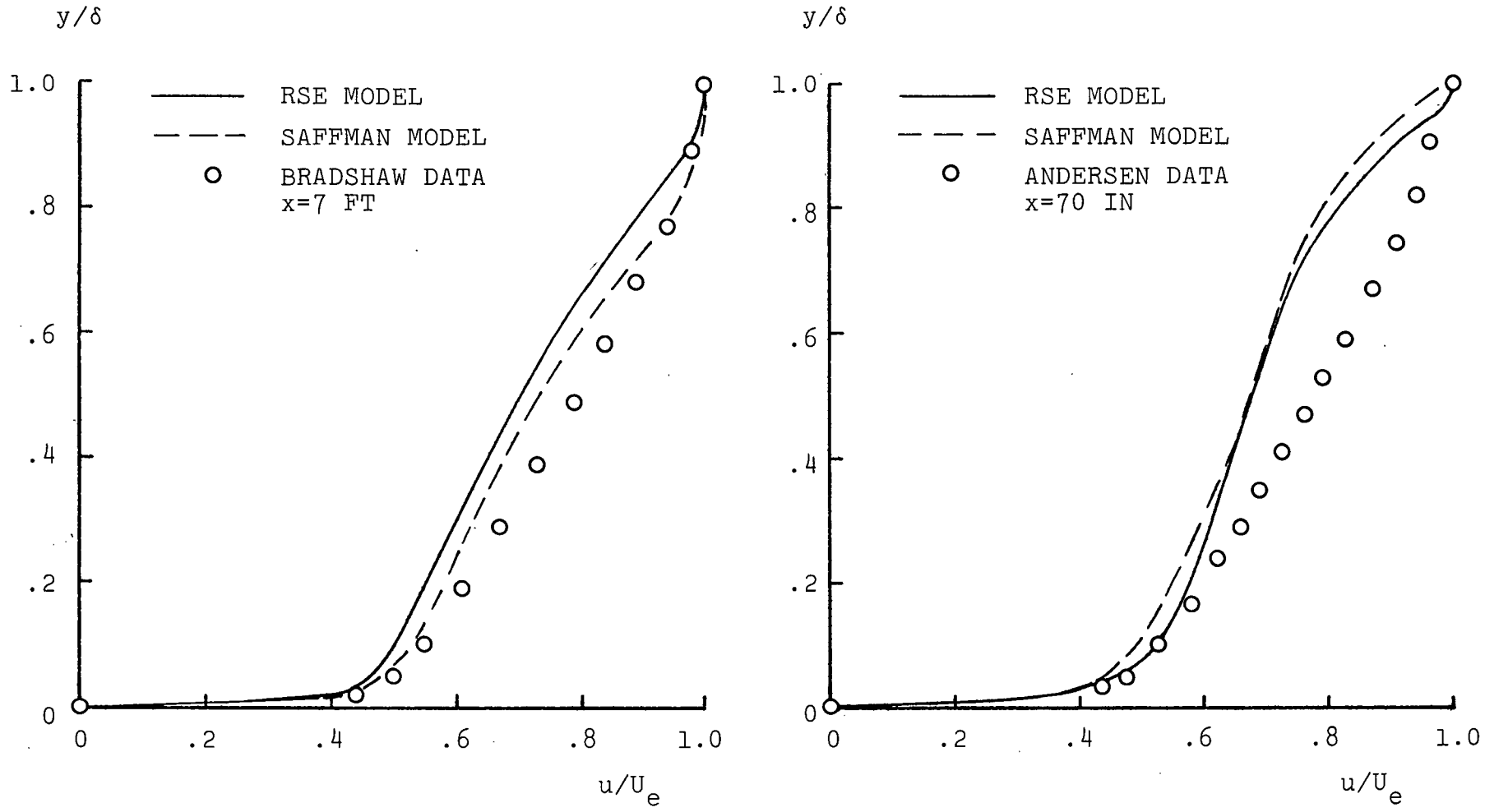

Figure 1. Comparison of computed and measured velocity profiles for turbulent boundary layers with adverse pressure gradient.

2. DEVELOPING A BASELINE MODEL

This section traces the evolution of a new two-equation model of turbulence. First, Saffman-model-predicted defect-layer structure for a flat-plate boundary layer (FPBL) is analyzed using singular-perturbation techniques. Next, a new model is postulated and is shown to yield defect-layer properties which are in much closer agreement with measurements than those of the Saffman model. The high Reynolds-number form of the Saffman model, the new model, and two other popular two-equation models are then compared by computing several boundary layers. Finally, with appropriate viscous modifications,† the new model is applied to equilibrium boundary-layer flows.

2.1 PERTURBATION ANALYSIS OF THE DEFECT LAYER

As discussed in the Introduction, the problems in Saffman and RSE model solutions apparently originate in the defect layer. In order to determine the nature of the models' deficiencies, a singular-perturbation analysis of Saffman-model-predicted defect-layer structure has been conducted for a zero pressure gradient FPBL. As a first step in the analysis, the Saffman equations are suitably scaled and simplified for the defect layer. Then numerical solutions are presented in which the boundary-layer edge conditions are parametrically varied. Finally, it is found that the Saffman model predicts a too-large peak value of the turbulent length scale, ℓ.

2.1.1 Formal Expansion Procedure

The Saffman model equations of motion for incompressible two-dimensional boundary layers are

† Viscous modifications are changes required to add molecular viscosity to the momentum and model equations, where appropriate, to permit integrating the equations through the viscous sublayer.

$$\frac{\partial u}{\partial x} + \frac{\partial v}{\partial y} = 0 \tag{1}$$

$$u\frac{\partial u}{\partial x} + v\frac{\partial u}{\partial y} = U_e\frac{dU_e}{dx} + \frac{\partial}{\partial y}\left[\left(\nu + \frac{e}{\omega}\right)\frac{\partial u}{\partial y}\right] \tag{2}$$

$$u\frac{\partial e}{\partial x} + v\frac{\partial e}{\partial y} = \left[\alpha^*\left|\frac{\partial u}{\partial y}\right| - \beta^*\omega\right]e + \frac{\partial}{\partial y}\left[\left(\nu + \sigma^*\frac{e}{\omega}\right)\frac{\partial e}{\partial y}\right] \tag{3}$$

$$u\frac{\partial \omega^2}{\partial x} + v\frac{\partial \omega^2}{\partial y} = \left[\alpha\left|\frac{\partial u}{\partial y}\right| - \beta\omega\right]\omega^2 + \frac{\partial}{\partial y}\left[\left(\nu + \sigma\frac{e}{\omega}\right)\frac{\partial \omega^2}{\partial y}\right] \tag{4}$$

where u and v are velocity components in the streamwise, x, and surface-normal, y, directions, respectively; U_e is the boundary-layer-edge velocity; ν is kinematic viscosity and the eddy viscosity is the ratio of turbulent mixing energy, e, and turbulent dissipation rate, ω. The six empirical parameters α, α^*, β, β^*, σ, σ^* are given by[5]

$$\left.\begin{aligned} \sigma = \sigma^* &= 0.50 \\ \beta = 0.15 \;,\; \beta^* &= 0.09 \\ \alpha^* &= 0.30 \\ \alpha = \beta/\alpha^* - 4\sigma\kappa^2 &= 0.1638 \quad \text{for} \quad \kappa = 0.41 \end{aligned}\right\} \tag{5}$$

where κ is Karman's constant.

Equations 1-5 must be solved subject to boundary conditions at the boundary-layer edge ($y\to\infty$) and at the surface ($y\to 0$). In the defect layer, we anticipate that the eddy viscosity is proportional to $U_e\delta^*$ where δ^* is displacement thickness, wherefore

$$\frac{\nu}{e/\omega} \sim \frac{\nu}{U_e\delta^*} = \frac{1}{Re_{\delta^*}} \tag{6}$$

where Re_{δ^*} denotes Reynolds number based on δ^*. Since $Re_{\delta^*} >> 1$ for turbulent boundary layers, molecular viscosity will be negligible in the defect layer. Consequently, defect-layer solutions must be subjected to boundary conditions as $y \to 0$ which are valid at the outer edge of the viscous sublayer, namely, the law of the wall. As shown by Saffman and Wilcox,[5] this means

$$\left.\begin{aligned} \frac{\partial u}{\partial y} &\to \frac{u_\tau}{\kappa y} \\ e &\to \frac{u_\tau^2}{\alpha^*} \\ \omega &\to \frac{u_\tau}{\alpha^* \kappa y} \end{aligned}\right\} \quad \text{as} \quad y \to 0 \tag{7}$$

Equations 7 are valid on the sublayer scale as $u_\tau y/\nu \to \infty$. Formally we are matching the outer (defect-layer) solution to the inner (sublayer) solution.

Finally, at the boundary-layer edge we impose the values of u, e and ω, viz:

$$\left.\begin{aligned} u &= U_e \\ e &= e_e \\ \omega &= \omega_e \end{aligned}\right\} \quad \text{as} \quad y \to \infty \tag{8}$$

Following Bush and Fendell,[26] we introduce the following nondimensional quantities:

$$\left.\begin{aligned} E &\equiv e/U_e^2 \\ W &\equiv \delta^* \omega / U_e \\ \xi &\equiv x/L \\ \eta &\equiv \frac{u_\tau}{U_e} \frac{y}{\delta^*} \end{aligned}\right\} \tag{9}$$

where L is a length typical of the distance from the plate leading edge. Note that the eddy viscosity becomes

$$\frac{e}{\omega} = U_e \delta^* \frac{E}{W} \tag{10}$$

and that the quantity $U_e\delta^*/u_\tau$ is the Clauser thickness. It is convenient to work with the streamfunction, ψ, defined by

$$\frac{u}{U_e} = \frac{\partial \psi}{\partial y} \quad ; \quad \frac{v}{U_e} = -\left[\frac{\partial \psi}{\partial x} + \frac{1}{U_e}\frac{dU_e}{dx}\psi\right] \tag{11}$$

Finally, we introduce the scaled streamfunction, F, given by

$$F \equiv \frac{1}{\delta^*}\frac{u_\tau}{U_e}\psi \tag{12}$$

In terms of the transformation defined in Equations 9-12, the equations of motion become (neglecting molecular viscosity):

Momentum

$$\left(\frac{u_\tau^2/U_e^2}{\delta^*/L}\right)\frac{\partial}{\partial\eta}\left[\frac{E}{W}\frac{\partial^2 F}{\partial\eta^2}\right] + \left(mF + \frac{\partial F}{\partial\xi}\right)\frac{\partial^2 F}{\partial\eta^2} - \frac{\partial F}{\partial\eta}\frac{\partial^2 F}{\partial\xi\partial\eta} + \frac{1}{U_e}\frac{dU_e}{d\xi}\left[1 - \left(\frac{\partial F}{\partial\eta}\right)^2\right] = 0 \tag{13}$$

Mixing Energy

$$\left(\frac{u_\tau^2/U_e^2}{\delta^*/L}\right)\frac{\partial}{\partial\eta}\left[\sigma^*\frac{E}{W}\frac{\partial E}{\partial\eta}\right] + \left(mF + \frac{\partial F}{\partial\xi}\right)\frac{\partial E}{\partial\eta} - \frac{\partial F}{\partial\eta}\frac{\partial E}{\partial\xi} + \left\{\alpha^*\left(\frac{u_\tau/U_e}{\delta^*/L}\right)\left|\frac{\partial^2 F}{\partial\eta^2}\right| - \beta^*\left(\frac{1}{\delta^*/L}\right)W - \frac{2}{U_e}\frac{dU_e}{d\xi}\frac{\partial F}{\partial\eta}\right\}E = 0 \tag{14}$$

Dissipation Rate

$$\left(\frac{u_\tau^2/U_e^2}{\delta^*/L}\right)\frac{\partial}{\partial\eta}\left[\sigma\frac{E}{W}\frac{\partial W^2}{\partial\eta}\right] + \left(mF + \frac{\partial F}{\partial\xi}\right)\frac{\partial W^2}{\partial\eta} - \frac{\partial F}{\partial\eta}\frac{\partial W^2}{\partial\xi} + \left\{\alpha\left(\frac{u_\tau/U_e}{\delta^*/L}\right)\left|\frac{\partial^2 F}{\partial\eta^2}\right|\right.$$

$$\left. - \beta\left(\frac{1}{\delta^*/L}\right)W - 2\left(\frac{1}{U_e}\frac{dU_e}{d\xi} - \frac{1}{\delta^*}\frac{d\delta^*}{d\xi}\right)\frac{\partial F}{\partial\eta}\right\} W^2 = 0 \qquad (15)$$

where the quantity m is defined by

$$m \equiv \frac{2}{U_e}\frac{dU_e}{d\xi} + \frac{1}{\delta^*}\frac{d\delta^*}{d\xi} - \frac{1}{u_\tau}\frac{du_\tau}{d\xi}$$

Also, the boundary conditions (Equations 7 and 8) transform to

$$\frac{\partial F}{\partial\eta} \to 1 \quad , \quad E \to \frac{e_e}{U_e^2} \quad , \quad W \to \frac{\delta^*\omega_e}{U_e} \quad \text{as} \quad \eta \to \infty \qquad (16)$$

$$\frac{\partial^2 F}{\partial\eta^2} \to \frac{u_\tau/U_e}{\kappa\eta} \quad , \quad E \to \frac{u_\tau^2/U_e^2}{\alpha^*} \quad , \quad W \to \frac{u_\tau^2/U_e^2}{\alpha^*\kappa\eta} \quad \text{as} \quad \eta \to 0 \qquad (17)$$

To solve these equations, we assume that the velocity deviates only slightly from the freestream velocity which is expressed by writing a perturbation expansion in powers of $u_\tau/U_e << 1$ as follows:

$$F = \eta - \frac{u_\tau}{U_e}F_1 + O\left(\frac{u_\tau}{U_e}\right)^2 \qquad (18)$$

Similarly, the scaling for E and W follows from Equation 17 so that we write

$$E = \frac{1}{\alpha^*}\frac{u_\tau^2}{U_e^2}E_o + O\left(\frac{u_\tau}{U_e}\right)^3 \qquad (19)$$

$$W = \frac{1}{\alpha^*}\frac{u_\tau^2}{U_e^2}W_o + O\left(\frac{u_\tau}{U_e}\right)^3 \qquad (20)$$

Then introducing

$$u_1 \equiv \partial F_1/\partial\eta \tag{21}$$

and assuming $u_\tau^2/U_e^2 \sim \delta^*/L$, the momentum equation becomes, to leading order

$$\frac{\partial}{\partial\eta}\left\{\frac{E_o}{W_o}\frac{\partial u_1}{\partial\eta} + \frac{m\delta^*/L}{u_\tau^2/U_e^2}\eta u_1\right\} - \left[\frac{3}{U_e}\frac{dU_e}{d\xi} + \frac{1}{\delta^*}\frac{d\delta^*}{d\xi}\right]\frac{\delta^*/L}{u_\tau^2/U_e^2}u_1$$

$$= \frac{\delta^*/L}{u_\tau^2/U_e^2}\frac{\partial u_1}{\partial\xi} \tag{22}$$

Equation 22 will have self-similar solutions (i.e., independent of ξ) provided the following four quantities are independent of ξ:

$$\alpha_T \equiv \frac{\delta^*/L}{u_\tau^2/U_e^2}\frac{1}{\delta^*}\frac{d\delta^*}{d\xi} = \frac{U_e^2}{u_\tau^2}\frac{d\delta^*}{dx} = \frac{2}{c_f}\frac{d\delta^*}{dx} \tag{23}$$

$$\beta_T \equiv -\frac{\delta^*/L}{u_\tau^2/U_e^2}\frac{1}{U_e}\frac{dU_e}{d\xi} = -\frac{\delta^*}{u_\tau^2}U_e\frac{dU_e}{dx} = \frac{\delta^*}{\tau_w}\frac{dp}{dx} \tag{24}$$

$$\sigma_T \equiv \frac{1}{2}\frac{\delta^*/L}{\xi u_\tau^2/U_e^2} = \frac{1}{2}\frac{\delta^*}{x}\frac{2}{c_f} = \frac{\delta^*}{xc_f} \tag{25}$$

$$\omega_T \equiv \frac{1}{2}\frac{\delta^*/L}{u_\tau^2/U_e^2}\frac{1}{u_\tau}\frac{du_\tau}{d\xi} = \frac{1}{2}\frac{U_e^2}{u_\tau^2}\frac{\delta^*}{u_\tau}\frac{du_\tau}{dx} = \frac{\delta^*}{c_f u_\tau}\frac{du_\tau}{dx} \tag{26}$$

where c_f is skin friction, τ_w is shear stress at the wall, and p is pressure. Substituting Equations 23-26 into Equation 22 yields

$$\frac{\partial}{\partial\eta}\left[\frac{E_o}{W_o}\frac{\partial u_1}{\partial\eta} + (\alpha_T - 2\beta_T - 2\omega_T)\,\eta u_1\right] + \left[3\beta_T - \alpha_T\right]u_1 = \sigma\sigma_T\, 2\xi\frac{\partial u_1}{\partial\xi} \quad (27)$$

Similarly, the E_o equation simplifies to the following:

$$\frac{\partial}{\partial\eta}\left[\sigma^*\frac{E_o}{W_o}\frac{\partial E_o}{\partial\eta} + (\alpha_T - 2\beta_T - 2\omega_T)\,\eta E_o\right]$$

$$+ \left\{\alpha^*\left|\frac{\partial u_1}{\partial\eta}\right| - \alpha^* W_o - (\alpha_T - 2\beta_T + 2\omega_T)\right\}E_o = \sigma_T\, 2\xi\frac{\partial E_o}{\partial\xi} \quad (28)$$

while the equation for W_o becomes:

$$\frac{\partial}{\partial\eta}\left[\sigma\frac{E_o}{W_o}\frac{\partial W_o^2}{\partial\eta} + (\alpha_T - 2\beta_T - 2\omega_T)\,\eta\, W_o^2\right]$$

$$+ \left\{\alpha\left|\frac{\partial u_1}{\partial\eta}\right| - \frac{\beta}{\alpha^*}W_o + (\alpha_T - 6\omega_T)\right\}W_o^2 = \sigma_T\, 2\xi\,\frac{\partial W_o^2}{\partial\xi} \quad (29)$$

As shown by Bush and Fendell,[6]

$$\omega_T = o(1) \quad \text{as} \quad Re_{\delta^*} \to \infty$$

while the momentum integral equation shows that if self-similar solutions exist, α_T and β_T are related as follows:

$$\alpha_T = 1 + 3\beta_T$$

Hence, assuming that α_T and β_T are constant, the defect-layer equations are:

Momentum

$$\frac{d}{d\eta}\left[\frac{E_o}{W_o}\frac{du_1}{d\eta}\right] + (1+\beta_T)\,\eta\,\frac{du_1}{d\eta} + \beta_T u_1 = 0 \qquad (30)$$

Mixing Energy

$$\frac{d}{d\eta}\left[\sigma^*\frac{E_o}{W_o}\frac{dE_o}{d\eta}\right] + (1+\beta_T)\eta\,\frac{dE_o}{d\eta} + \alpha^*\left[\left|\frac{du_1}{d\eta}\right| - W_o\right]E_o = 0 \qquad (31)$$

Dissipation Rate

$$\frac{d}{d\eta}\left[\sigma\frac{E_o}{W_o}\frac{dW_o^2}{d\eta}\right] + (1+\beta_T)\,\eta\,\frac{dW_o^2}{d\eta} + \left[\alpha\left|\frac{du_1}{d\eta}\right| - \frac{\beta}{\alpha^*}W_o + 2(1+2\beta_T)\right]W_o^2 = 0 \qquad (32)$$

which must be solved subject to

$$u_1 \to 0\ , \quad E_o \to \frac{\alpha^* e_e}{u_\tau^2}\ , \quad W_o \to \frac{2\alpha^*}{c_f}\frac{\omega_e \delta^*}{U_e} \quad \text{as } \eta\eta \to \infty \qquad (33)$$

$$\frac{\partial u_1}{\partial \eta} \to -\frac{1}{\kappa\eta}\ ; \quad EE_{oo} \to 11\ ; \quad WW_{oo} \to \frac{11}{\kappa\eta} \quad \text{as} \quad \eta \to 0 \qquad (34)$$

2.1.2 Numerical Solution of the Defect-Layer Equations

Equations 30-34 were solved using an implicit, second-order accurate, time-marching, finite-difference code. Only the zero-pressure-gradient case (β_T=0) was considered. To achieve converged solutions, we found it necessary to impose the boundary-layer-edge conditions at a sharp turbulent-nonturbulent interface.† This is unsurprising as Saffman[2] has shown that the model equations predict the existence of such interfaces when e and ω approach zero in the freestream. The interface structure remains unaltered when e and ω have finite values in the freestream. That

†The sharpness manifests itself as a discontinuity in ∂u/∂y and ∂ω/∂y.

is, as a generalization of the analysis by Saffman, upon approaching a turbulent-nonturbulent interface ($y=\delta$) from the turbulent side, the solution behavior is

$$\left.\begin{aligned} e - e_e &\sim (\delta - y)^2 \\ \omega - \omega_e &\sim (\delta - y) \\ u - U_e &\sim (\delta - y) \end{aligned}\right\} \quad \text{as} \quad y \to \delta$$

provided $\sigma = \sigma^* = 1/2$.

Several computations were done to determine solution sensitivity to e_e, ω_e, σ, and σ^*. Figure 2 shows velocity profiles for a set of computations in which solution sensitivity to e_e was examined. In the computations, the following experimental boundary condition was implemented in an attempt to eliminate solution dependence upon ω_e:

$$\frac{\partial \ell}{\partial y} = 0 \quad \text{at} \quad y = \delta \tag{35}$$

where

$$\ell \equiv e^{1/2}/\omega \tag{36}$$

As shown in the figure, the model predicts only a very weak "wake" component. The computed velocity profile deviates significantly from Coles' composite "wall-wake" profile. Values of $\alpha^* e_e/u_\tau^2$ less than 0.01 (corresponding to a turbulence intensity of about 0.3%) have little effect on the solution. Larger values of $\alpha^* e_e/u_\tau^2$ cause the solution to deviate from Coles' profile even more than the $e_e \to 0$ solutions. Since Coles' profile provides a fairly accurate representation of experimental data, the model apparently is quite inaccurate in the defect layer.

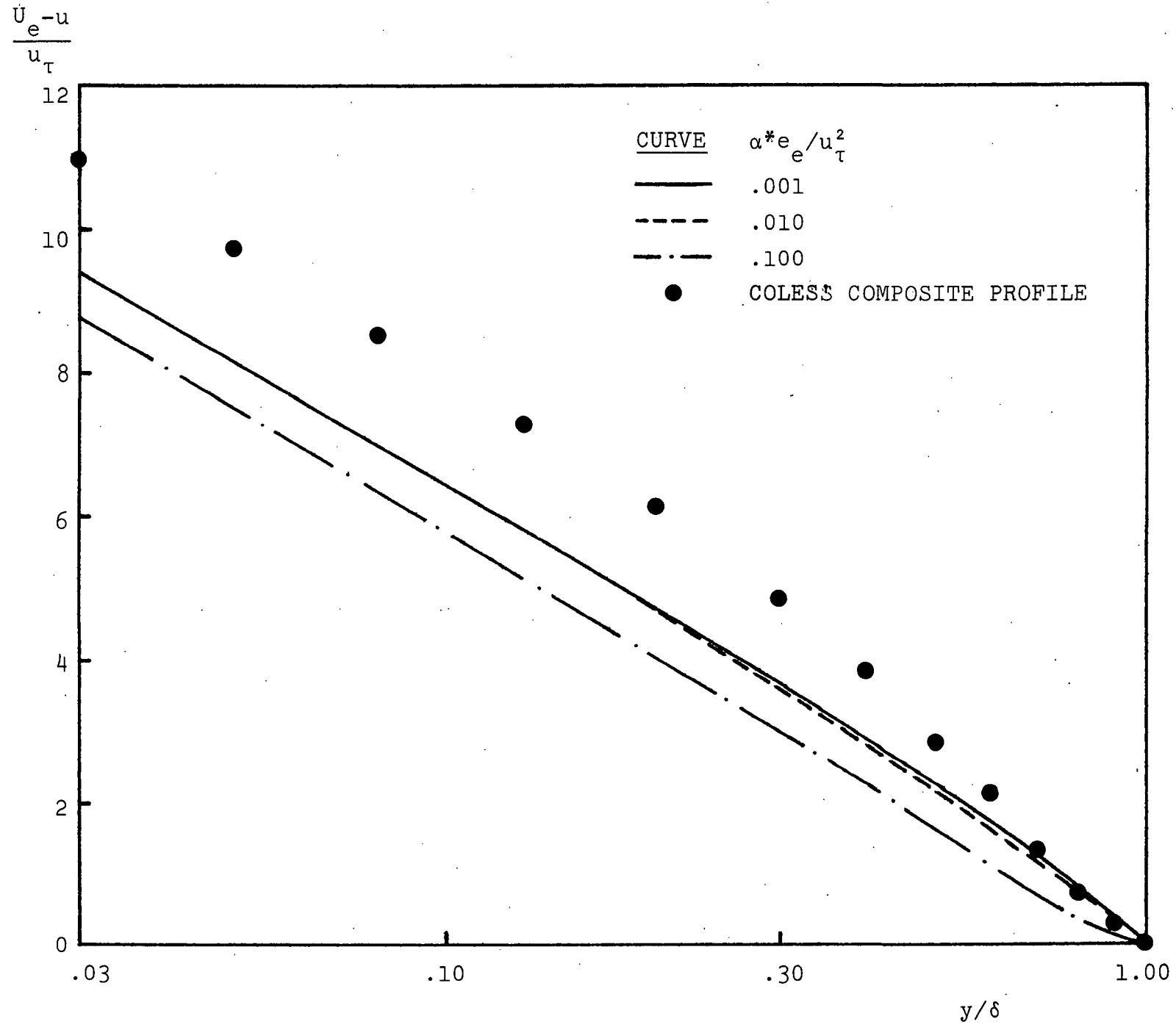

Figure 2. Comparison of computed Saffman-model velocity profiles with Coles' composite wall-wake profile.

No combination of σ, σ^*, e_e, and ω_e was found which would give more accurate defect-layer velocity profiles. The source of the difficulty can be seen by inspection of the computed length-scale, ℓ, profile. In terms of ℓ, the eddy viscosity, $\varepsilon = e/\omega$, can be written as

$$\varepsilon = e^{1/2}\,\ell \tag{37}$$

As shown by Ng and Spalding[7] (who use Equation 37), $\ell/\sqrt{\alpha^*}$ should be nearly equal to the standard mixing length provided e is close to the turbulent energy, as it is for the Saffman-model solution. Figure 3 compares the computed length-scale profile with the mixing-length profile deduced by Klebanoff.[8] The peak value of the mixing length is between 0.09δ and 0.10δ. By contrast, the peak value of $\ell/\sqrt{\alpha^*}$ predicted by the Saffman model is about 0.17δ.

Further numerical experimentation showed that the peak value of ℓ/δ can be suppressed somewhat by using extremely large values of ω_e. This is generally accompanied by severe numerical difficulties and by little improvement in the velocity profiles. A second means for reducing the peak value of ℓ/δ is to reduce the value of σ; the reduction is slight, however. The value of σ^* has virtually no effect on $(\ell/\delta)_{max}$ although the value of δ depends strongly upon σ^*.

Hence, the Saffman model inherently predicts too large of a value of $(\ell/\delta)_{max}$ in the defect layer. Consequently, since e is computed with reasonable accuracy, the eddy viscosity is overestimated as can be seen by noting that the Saffman model typically predicts

$$\frac{\varepsilon_{max}}{U_e \delta^*} \sim 0.035 \tag{38}$$

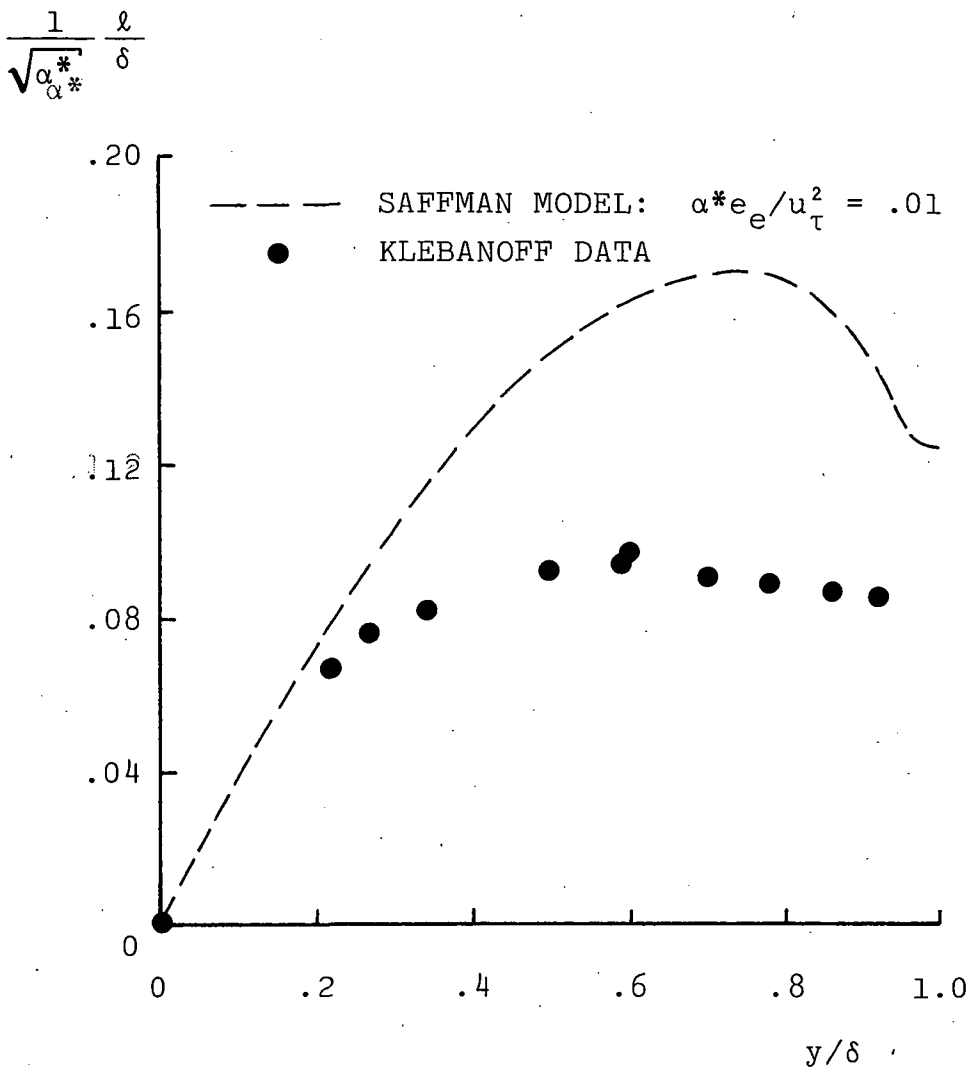

Figure 3. Comparison of computed length-scale profile with mixing-length profile deduced from measurements.

a value more than double that assumed (0.0168) in the mixing-length/eddy-viscosity formulation. The large peak values of ℓ/δ and $\varepsilon/U_e\delta^*$ predicted by the Saffman model cause the curious inflected velocity profiles we have so often obtained with the model (see Figure 1). Consistent with the defect-layer analysis presented above, accurate skin friction, shape factor, etc., can only be obtained by using unreasonably large values of ω at the boundary-layer edge with an attendant distortion of the velocity profiles.

2.2 A NEW TWO-EQUATION TURBULENCE MODEL

After obtaining numerical solutions to the defect layer equations and discovering the exaggerated peak value of ℓ/δ, the next logical step was to find the specific cause of the inaccuracy. In order to do this, we examined the Jones-Launder[9] and Ng-Spalding[7] turbulence models, both of which predict more-realistic peak values of ℓ/δ. As shown by Wilcox and Chambers,[1] these two models can be written in terms of the Saffman variables (e,ω) as follows:

Jones-Launder

$$\frac{d\omega^2}{dt} = c_\omega\left(\frac{\partial u}{\partial y}\right)^2\omega - \beta\omega^3 + \frac{\partial}{\partial y}\left[\sigma\sigma^*\frac{\partial\omega^2}{\partial y}\right]$$

$$- 2\sigma\left[\frac{\partial \ell}{\partial y} - \frac{1}{2}\ell\frac{\partial e/\partial y}{e}\right]\left[\frac{\partial \ell}{\partial y} + \frac{3}{2}\ell\frac{\partial e/\partial y}{e}\right]\omega^3$$

$$+ 2(\sigma - \sigma^*)\frac{\omega^2}{e}\frac{\partial}{\partial y}\left[\varepsilon\frac{\partial e}{\partial y}\right] \qquad (39)$$

Ng-Spalding

$$\frac{d\omega^2}{dt} = c_\omega\left(\frac{\partial u}{\partial y}\right)^2\omega - \beta\omega^3 + \frac{\partial}{\partial y}\left[\sigma\,\varepsilon\frac{\partial\omega^2}{\partial y}\right]$$

$$- 6\sigma\left(\frac{\partial \ell}{\partial y}\right)^2\omega^3 + 2c_w\left(\frac{\ell}{y}\right)^6\omega^3 \qquad (40)$$

If we (ⓐ) assume that $\frac{\ell}{e}\frac{\partial e}{\partial y} << \frac{\partial \ell}{\partial y}$, (ⓑ) ignore the term proportional to $(\sigma-\sigma^*)$ in the Jones-Launder model, and (ⓒ) denote the production term by P_ω, we can write the following single equation which approximates the three (including Saffman's) models:

$$\frac{d\omega^2}{dt} = P_\omega - \beta\omega^3 + \frac{\partial}{\partial y}\left[\sigma\,\varepsilon\,\frac{\partial \omega^2}{\partial y}\right] - \chi\,\sigma\left(\frac{\partial \ell}{\partial y}\right)^2\omega^3 \qquad (41)$$

where

$$\bar{\chi} = \begin{cases} 0 & , \text{ Saffman model} \\ 2 & , \text{ Jones-Launder model} \\ 6 - 2\dfrac{C_w}{\sigma}\dfrac{(\ell/y)^6}{(\partial\ell/\partial y)^2} & , \text{ Ng-Spalding model} \end{cases} \qquad (42)$$

Equations 41 and 42 show that the Jones-Launder and Ng-Spalding models have an additional dissipation term proportional to $\omega^3(\partial\ell/\partial y)^2$. This term has the effect of augmenting ω^2 dissipation near a surface where $\partial\ell/\partial y$ is largest; by contrast, in the defect-layer where $\partial\ell/\partial y$ is smallest, the net dissipation of ω^2 will be smaller than near the surface. The effect of this term is hence consistent with the notion that the most intense dissipation occurs in the smallest eddies which appear nearest a solid boundary. In the defect layer only large eddies are present wherefore dissipation will be smaller than near the surface.

Because the Jones-Launder and Ng-Spalding models predict more-realistic peak values of ℓ/δ, the possibility exists that the Saffman-model might be improved if such a term is added to the ω^2 equation. A value for χ can be chosen by noting that, in the wall layer

$$\left(\frac{\ell}{y}\right)^2 = \alpha^*\kappa^2 \qquad (43)$$

Hence with $c_w = 702$, $\kappa = 0.41$, $\alpha^* = 0.3$, $\sigma = 1$, we obtain

$$6 - 2\frac{c_w}{\sigma}\frac{(\ell/y)^6}{(\partial\ell/\partial y)^2} = 6 - 2\frac{c_w \alpha^{*2} \kappa^4}{\sigma} = 2.43 \qquad (44)$$

It thus appears that χ should lie between about 2.0 and 2.5.

With such a modification, we postulate the following new baseline model for incompressible boundary layers,

Baseline Model

$$u\frac{\partial e}{\partial x} + v\frac{\partial e}{\partial y} = \left\{\alpha^*\left|\frac{\partial u}{\partial y}\right| - \beta^*\omega\right\}e + \frac{\partial}{\partial y}\left[\left(\nu + \sigma^*\frac{e}{\omega}\right)\frac{\partial e}{\partial y}\right] \qquad (45)$$

$$u\frac{\partial \omega^2}{\partial x} + v\frac{\partial \omega^2}{\partial y} = \left\{\alpha\left|\frac{\partial u}{\partial y}\right| - \left[\beta + \chi\sigma(\partial\ell/\partial y)^2\right]\omega\right\}\omega^2 + \frac{\partial}{\partial y}\left[\left(\nu + \sigma\frac{e}{\omega}\right)\frac{\partial \omega^2}{\partial y}\right] \qquad (46)$$

$$\left.\begin{aligned} \sigma = \sigma^* &= 1/2 \\ \beta = 0.15 \;,\; \beta^* &= 0.09 \\ \alpha^* &= 0.3 \\ \alpha = \beta/\alpha^* &- (4 - \chi)\sigma\kappa^2 \end{aligned}\right\} \qquad (47)$$

Figure 4 presents the computed ℓ/δ profile for χ=2. The peak value of ℓ/δ is much closer to the Klebanoff mixing-length data than that obtained with the Saffman model. Computed velocity profiles are presented in Figure 5. As shown, excellent agreement between the numerical profiles and Coles' wall-wake profile is obtained. Additionally, the mixing energy is in somewhat closer agreement with the measured RMS vertical velocity fluctuation data of Klebanoff[10] (see Figure 6). Using χ=2.5 causes only slight changes in computed profiles.

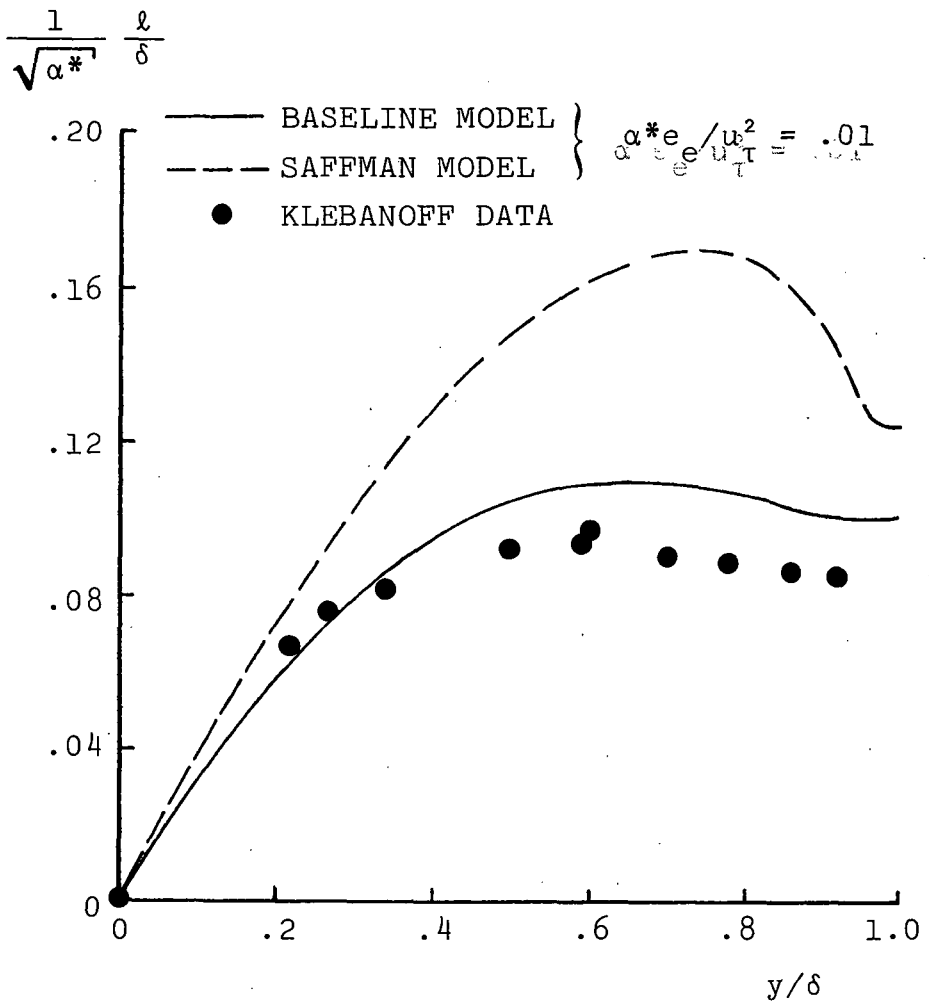

Figure 4. Comparison of computed length-scale profiles with mixing-length profiles deduced from measurements.

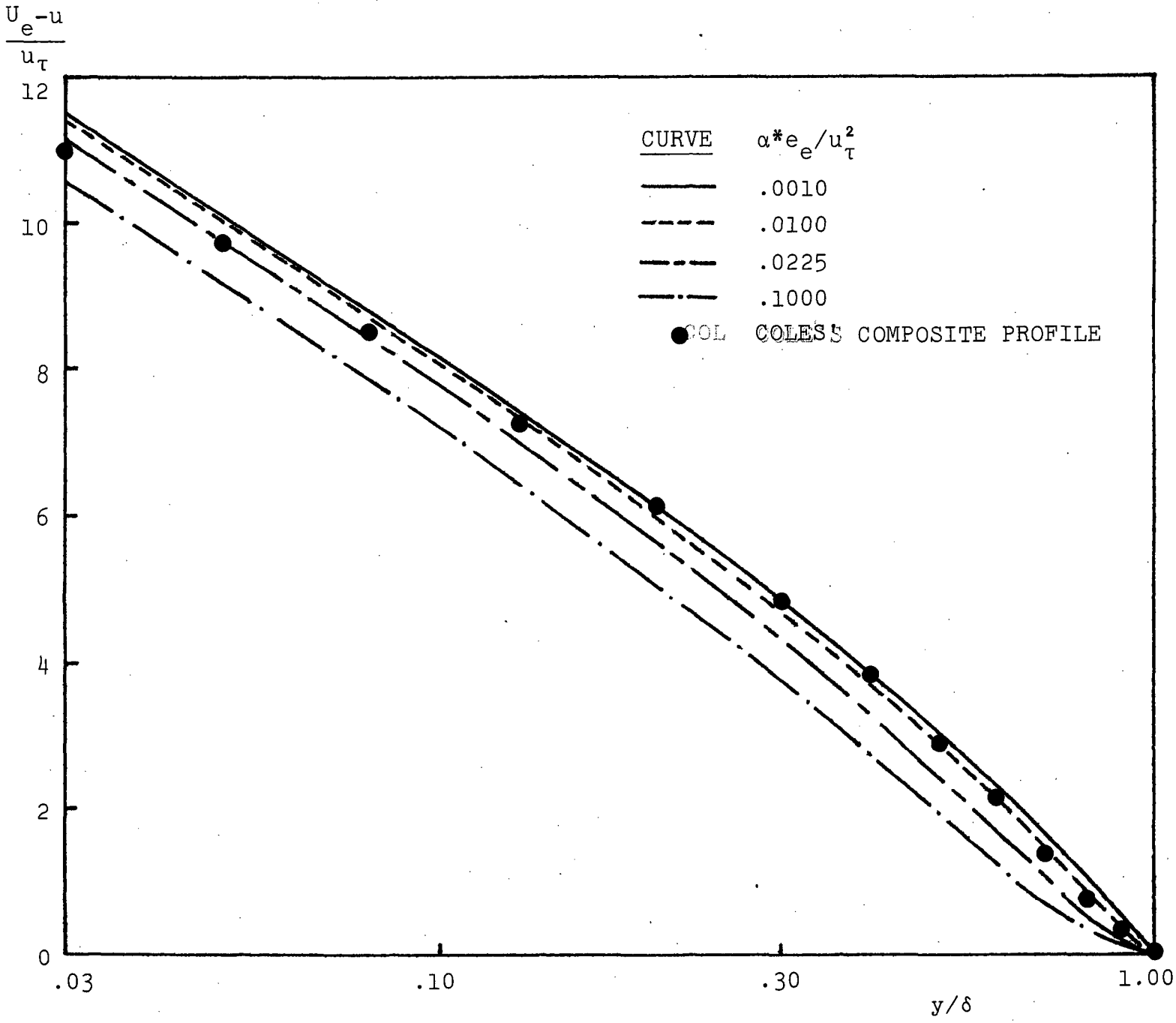

Figure 5. Comparison of computed Baseline-model velocity profiles with Coles' composite wall-wake profile.

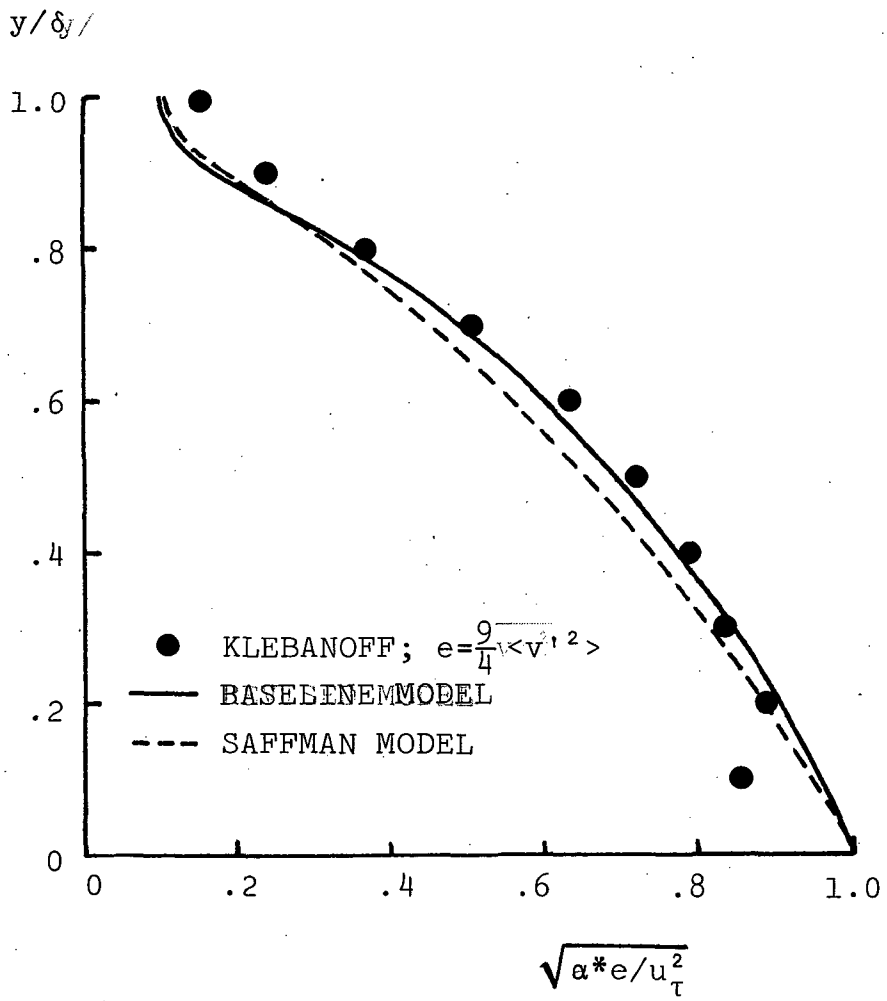

Figure 6. Comparison of computed turbulent mixing energy profiles with Klebanoff's RMS vertical velocity fluctuation data.

It is possible to obtain skin friction from the perturbation solution. Matching demands that as $\eta \to 0$, the defect-layer solution must equal the limiting form of the sublayer solution as $u_\tau y/\nu \to \infty$. Now, inspection of the velocity profiles in Figures 2 and 5 shows that

$$u \to U_e - u_\tau \left[-\frac{1}{\kappa} \log \eta + A \right] \quad \text{as} \quad \eta \to 0 \tag{48}$$

where A is a constant which can only be determined as part of the solution (note that Bush and Fendell mistakenly demand that A=0). In terms of the sublayer variables, Equation 48 can be rewritten as

$$\frac{u}{u_\tau} \to \frac{1}{\kappa} \log \frac{u_\tau y}{\nu} + \left\{ \frac{U_e}{u_\tau} - \frac{1}{\kappa} \log \mathrm{Re}_{\delta *} - A \right\} \quad \text{as} \quad \eta \to 0 \tag{49}$$

Finally, from the sublayer solution,

$$\frac{u}{u_\tau} \to \frac{1}{\kappa} \log \frac{u_\tau y}{\nu} + B \quad \text{as} \quad \frac{u_\tau y}{\nu} \to \infty \tag{50}$$

where $B \doteq 5.5$ is the standard constant in the law of the wall. Matching yields the following condition:

$$\frac{U_e}{u_\tau} = B + A + \frac{1}{\kappa} \log \mathrm{Re}_{\delta *} \tag{51}$$

wherefore the relation between skin friction, $c_f = 2u_\tau^2/U_e^2$ and $\mathrm{Re}_{\delta *}$ becomes

$$\frac{1}{c_f} = \frac{1}{2\kappa^2} (\log \mathrm{Re}_{\delta *})^2 + \frac{A+B}{\kappa} \log \mathrm{Re}_{\delta *} + \frac{(A+B)^2}{2} \tag{52}$$

Figure 7 compares skin friction for $\chi=0$ and $\chi=2$ with the Hopkins-Inouye correlation,[11] in which we have assumed the shape factor to be 1.30 wherefore

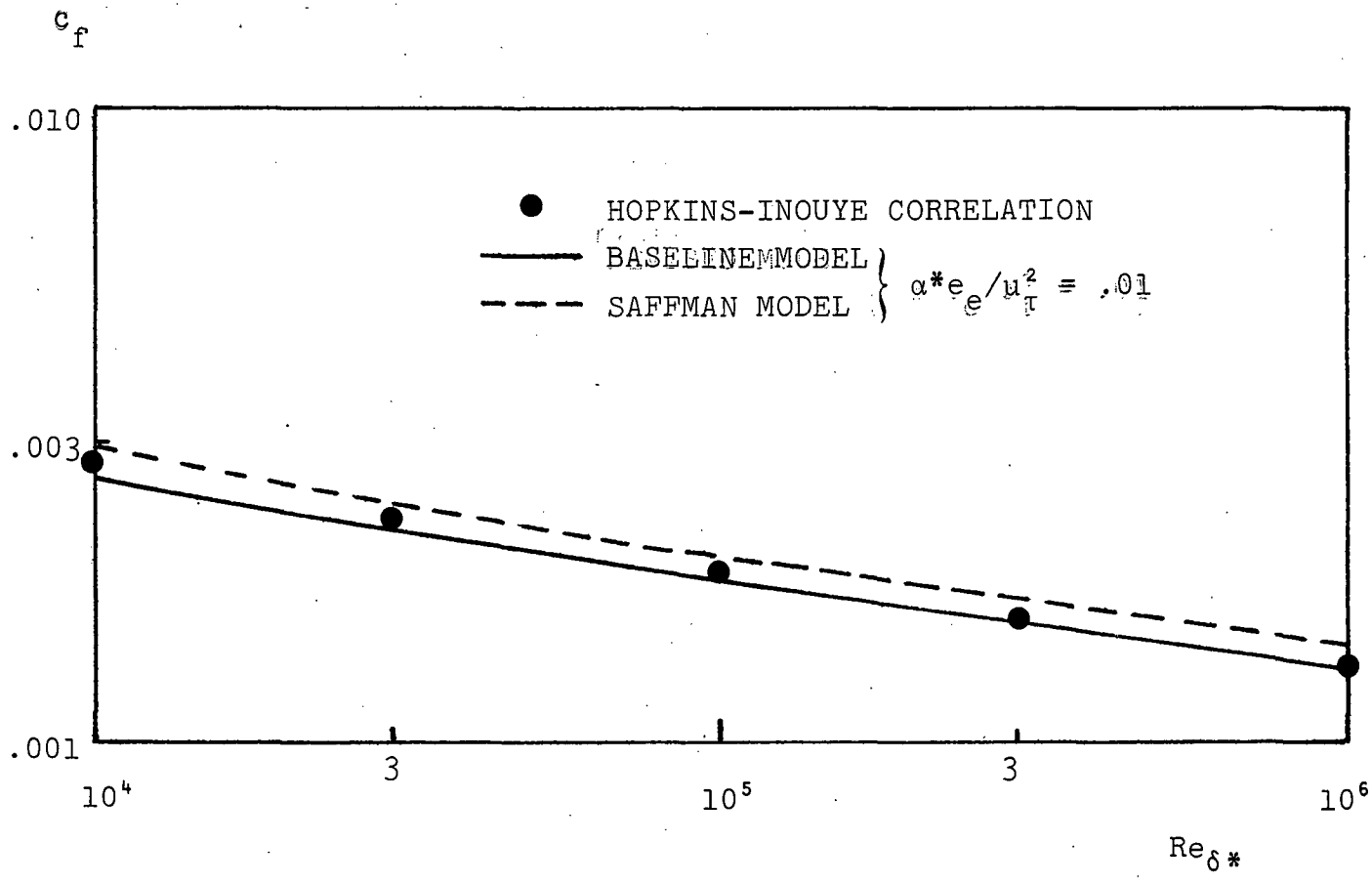

Figure 7. Comparison of computed skin friction with the Hopkins-Inouye correlation of experimental data.

$$\frac{1}{c_f} = 3.221\ (\log Re_{\delta*})^2 + 9.215 \log Re_{\delta*} + 3.373;$$

Hopkins-Inouye (53)

As shown in the figure, the Saffman-model c_f is generally about 10% higher than the Hopkins-Inouye value. This is consistent with previously computed values of c_f. The Baseline model with $\chi=2$ predicts values of c_f much closer to the Hopkins-Inouye values. It hence appears that the proposed revision holds promise for significantly improving Saffman-model accuracy.

2.3 TWO-EQUATION MODEL COMPARISON

To further test the Baseline model, a series of boundary-layer computations were performed. Since the objective of this study was to establish the most solid foundation possible for future research with the RSE model, we left the possibility open that a formulation other than the Baseline or Saffman models might be more accurate. Hence, a comparison of the Baseline, Saffman, Jones-Launder, and Ng-Spalding turbulence models was conducted. There is no need to consider additional models as all current two-equation models are variants of these four.

This comparison provides an objective basis for determining which of these models is most accurate overall. While previous comparisons of two-equation formulations have been made,[12,13] no one has made more than a cursory examination. Until now, no one has presented parallel numerical solutions for the various models. In this study, the models were tested under exactly the same conditions using the same numerics, boundary conditions, and starting profiles. Hence from the results of these computations, it is possible to determine precisely how well the models perform relative to each other and which model should serve as the basis for further analysis of streamline curvature/system rotation effects on turbulent boundary layers. Table 1 lists the flows considered and the data sources used.

Table 1. Flows Computed in Two-Equation-Model Comparisons

FLOW	DATA SOURCES
• Flat Plate Boundary Layer	Hopkins-Inouye[11] skin friction correlation; Klebanoff[10] flat plate data; Wieghardt[14] flat plate data.
• Bradshaw Adverse Pressure Gradient	Bradshaw[3] data; Coles'[14] version of Bradshaw data.
• Andersen Adverse Pressure Gradient	Andersen[4] data.
• Ludwieg-Tillmann Favorable Pressure Gradient	Ludwieg-Tillmann[14] data; Coles'[14] version of Ludwieg-Tillmann data.
• So-Mellor Constant Pressure Flow over convex wall	So-Mellor[15] data; Meroney[16] correlation.

Before proceeding to results of the computations, Subsections 2.3.1 through 2.3.3 present (a) the equations which constitute the various models, (b) boundary conditions used in the computations, and (c) initial profiles.

2.3.1 The Model Equations

The inviscid-incompressible forms (i.e., negligible Mach number and molecular viscosity) of the model equations were solved. The inviscid (i.e., high Reynolds number) forms were chosen because of the nonuniversality in the way viscous effects are included in the various turbulence models. In this way we help eliminate any preferential treatment of a given model. For all models, the conservation of mass and momentum equations are identical, viz,

Mass Conservation

$$\frac{\partial u}{\partial x} + \frac{\partial v}{\partial y} = 0 \tag{54}$$

Momentum Conservation

$$u\frac{\partial u}{\partial x} + v\frac{\partial u}{\partial y} = -\frac{1}{\rho}\frac{dp}{dx} + \frac{\partial}{\partial y}\left[\varepsilon \frac{\partial u}{\partial y}\right] \tag{55}$$

The two model equations for each formulation are as follows.

Saffman Model

Turbulent Mixing Energy

$$u\frac{\partial e}{\partial x} + v\frac{\partial e}{\partial y} = \left[\alpha^* \left|\frac{\partial u}{\partial y}\right| - \beta^*\omega\right]e + \frac{\partial}{\partial y}\left[\sigma^*\varepsilon\frac{\partial e}{\partial y}\right] \tag{56}$$

Dissipation Rate

$$u\frac{\partial \omega^2}{\partial x} + v\frac{\partial \omega^2}{\partial y} = \left[\alpha\left|\frac{\partial u}{\partial y}\right| - \beta\omega\right]\omega^2 + \frac{\partial}{\partial y}\left[\sigma\varepsilon\frac{\partial \omega^2}{\partial y}\right] \tag{57}$$

The values of the constants are

$$\beta = .15 \quad \beta^* = .09 \quad \alpha = \beta/\alpha^* - 4\sigma\kappa^2 = .1638$$
$$\sigma = .50 \quad \sigma^* = .50 \quad \alpha^* = .30$$

while the ratio of e and ω is the kinematic eddy viscosity, ε, i.e.,

$$\varepsilon = e/\omega \tag{58}$$

The Baseline model differs from the Saffman model only by the addition of one term to the dissipation rate equation as explained in the previous section.

Baseline Model

Turbulent Mixing Energy

$$u\frac{\partial e}{\partial x} + v\frac{\partial e}{\partial y} = \left[\alpha^*\left|\frac{\partial u}{\partial y}\right| - \beta^*\omega\right]e + \frac{\partial}{\partial y}\left[\sigma^*\varepsilon\frac{\partial e}{\partial y}\right] \qquad (59)$$

Dissipation Rate

$$u\frac{\partial \omega^2}{\partial x} + v\frac{\partial \omega^2}{\partial y} = \left[\alpha\left|\frac{\partial u}{\partial y}\right| - \beta\omega\right]\omega^2 + \frac{\partial}{\partial y}\left[\sigma\varepsilon\frac{\partial \omega^2}{\partial y}\right] - 2\sigma\left(\frac{\partial \ell}{\partial y}\right)^2\omega^3 \qquad (60)$$

Note that χ has been set equal to 2. All constants are the same as in the Saffman model except for α which is now given by the following expression:

$$\alpha = \beta/\alpha^* - 2\sigma\kappa^2$$

The kinematic eddy viscosity is given by Equation 58.

As noted earlier, similar to the Saffman and Baseline models, the Jones-Launder model uses turbulent mixing energy for one "turbulence density"; the second turbulence density is the dissipation function, ε_d.

Jones-Launder

Turbulent Mixing Energy

$$u\frac{\partial e}{\partial x} + v\frac{\partial e}{\partial y} = \varepsilon\left(\frac{\partial u}{\partial y}\right)^2 - \varepsilon_d + \frac{\partial}{\partial y}\left(\frac{\varepsilon}{\sigma_e}\frac{\partial e}{\partial y}\right) \qquad (61)$$

Dissipation Function

$$u\frac{\partial \varepsilon_d}{\partial x} + v\frac{\partial \varepsilon_d}{\partial y} = c_{\varepsilon 1}\frac{\varepsilon_d}{e}\varepsilon\left(\frac{\partial u}{\partial y}\right)^2 - c_{\varepsilon 2}\frac{\varepsilon_d^2}{e} + \frac{\partial}{\partial y}\left(\frac{\varepsilon}{\sigma_\varepsilon}\frac{\partial \varepsilon_d}{\partial y}\right) \qquad (62)$$

where

$$c_1 = 1.55, \quad c_2 = 2, \quad \sigma_e = 1.0, \quad \sigma_\varepsilon = 1.3$$

and the kinematic eddy viscosity takes on the following form:

$$\varepsilon \equiv .09\ e^2/\varepsilon_d \tag{63}$$

Finally, the Ng-Spalding model uses turbulent mixing energy and turbulent length scale.

Ng-Spalding

Turbulent Mixing Energy

$$u\frac{\partial e}{\partial x} + v\frac{\partial e}{\partial y} = \varepsilon\left(\frac{\partial u}{\partial y}\right)^2 - c_D\ \frac{e^{3/2}}{\ell} + \frac{\partial}{\partial y}\left(\frac{\varepsilon}{\sigma_e}\frac{\partial e}{\partial y}\right) \tag{64}$$

Length Scale

$$u\frac{\partial}{\partial x}(e\ell) + v\frac{\partial}{\partial y}(e\ell) = c_p \ell\varepsilon\left(\frac{\partial u}{\partial y}\right)^2 - \left(c_m + c_w\left(\frac{\ell}{y}\right)^6\right)e^{3/2} + \frac{\partial}{\partial y}\left[\frac{\varepsilon}{\sigma_z}\frac{\partial}{\partial y}(e\ell)\right] \tag{65}$$

where

$$c_D = .09, \quad c_p = .98, \quad c_m = .059, \quad c_w = 702, \quad \sigma_e = 1.0, \quad \sigma_z = 1.0$$

and

$$\varepsilon = e^{1/2}\ \ell \tag{66}$$

All four models use a turbulent mixing energy equation. Commonly, e is assumed to be the turbulent kinetic energy. However, Wilcox and Chambers have shown[1] that more appropriately e should be interpreted as $9/4\langle v'^2\rangle$ where v' is the fluctuating component of the velocity component normal to the surface. The

above fact is essential when determining such things as starting profiles.

The second turbulence parameter differs for the Saffman and Baseline (ω), Ng-Spalding (ℓ), and Jones-Launder (ε_d) models. The eddy viscosity, ε, is used in the same manner in each model as an integral part of approximating the Reynolds shear stress. Hence the various expressions for ε can be equated and relations between ω, ε_d, and ℓ can be derived. It is necessary to have such relations in order to impose the same boundary layer edge boundary conditions and initial profiles for each of the models. In terms of e and ℓ, the dissipation rate and dissipation function are

$$\omega = e^{1/2}/\ell \tag{67}$$

and

$$\varepsilon_d = 0.09 e^{3/2}/\ell \tag{68}$$

In addition to comparing the four models, results of the computations yield two important conclusions about all the models. One, accurate starting profiles can be obtained by knowing only the mean velocity profile and the Reynolds shear stress profile at the starting location. Two, the models are not sensitive to either initial e and ℓ profiles or to the boundary layer edge boundary conditions on e and ℓ as long as reasonable values are used.

2.3.2 Boundary Conditions

Since the inviscid forms of the four models are considered, it is not possible to integrate through the viscous sublayer. Hence, it is necessary to assume that the sublayer has zero thickness and then match to the law of the wall. A singular

perturbation solution of the model equations, valid as $y \to 0$, yields the proper boundary conditions. Such a perturbation solution (valid for boundary layers with and without pressure gradient) for all four models is listed below.

$$\left.\begin{aligned} \frac{u}{u_\tau} &= \frac{1}{\kappa} \ln \frac{u_\tau y}{\nu} + B \\ e &= u_\tau^2/\alpha^* \\ \ell &= \sqrt{\alpha^*}\, \kappa y \end{aligned}\right\} \qquad (69)$$

The quantity u_τ is the friction velocity, κ is Karman's constant, α^* is the constant in the Saffman formulation and B is the constant in the law of the wall. In all calculations, the constant B was held fixed at 5.5.

The boundary conditions in Equation 69 must be applied close to the surface, viz, at least closer than a y^+ (defined as $u_\tau y/\nu$) of 20 and preferably at a y^+ of about 10. Applying the conditions closer than y^+ of 10 made little difference while applying them above 20 significantly affected the solutions. On first inspection, it may seem inaccurate to apply the boundary conditions so close to the surface that the law of the wall does not actually hold (i.e., $y^+ \lesssim 30$). However, Equations 69 are the rigorous solution to the inviscid momentum equation as y approaches 0. That is, by assuming that the sublayer has negligible thickness, Equations 69 are the singular perturbation solutions for the various models and are the appropriate boundary conditions in the limit as y approaches 0.

The perturbation analysis of the defect layer described in Subsections 2.1 and 2.2 indicates the appropriate boundary-layer-edge value of the turbulent mixing energy. The analysis shows that a value of e corresponding to $\alpha^* e/u_\tau^2 = .01$ is the largest value consistent with the equations that yields accurate defect

layer velocity profiles; using smaller values of e make little difference. Since the larger value is somewhat eastier to handle numerically, all computations were performed with $\alpha^* e/u_\tau^2 \doteq .01$.

Because the model equations predict existence of a sharp turbulent-nonturbulent interface at the boundary-layer edge, imposing $\partial \ell/\partial y = 0$ (Equation 35) proves to be very difficult. Hence, consistent with mixing-length approximations, a value of $\ell/\sqrt{\alpha^*}\delta = .09$ at the boundary layer edge was imposed. Varying the edge value of $\ell/\sqrt{\alpha^*}\delta$ over the range of .06 to .12 made little difference in the numerical solutions. Hence, an important conclusion is that the models are not inordinately sensitive to the edge values of e and ℓ.

2.3.3 Initial Profiles

Prior to this study, determining reliable initial profiles for the turbulence quantities was always an area of uncertainty. As will now be demonstrated, this uncertainty has been eliminated.

Starting profiles for all models are most conveniently formulated in terms of the length scale, ℓ; Equations 67 and 68 are then used to determine ω and ε_d. Noting that e is interpreted as $9/4\langle v'^2\rangle$, starting profiles can be easily obtained if $\langle v'^2\rangle$, $\langle -u'v'\rangle$, and u data are available at the starting location. That is, e can be determined directly from the $\langle v'^2\rangle$ data while ℓ can be found from the following equation

$$e^{1/2}\,\ell\,\frac{\partial u}{\partial y} = \langle -u'v'\rangle \qquad (70)$$

However, such complete information is not always available. Nevertheless, good profiles can still be determined with only $\langle -u'v'\rangle$ and u data at the starting location. This is done using the following procedure.

First, it is assumed that an arbitrary e starting profile can be written as

$$e = \Psi^2 e_{FPBL} \tag{71}$$

where Ψ is a constant to be determined and e_{FPBL} is the high-Reynolds-number FPBL e profile.† From empirical observation, this is a good approximation for equilibrium boundary layers. The FPBL $9/4\langle v'^2\rangle$ profile can be approximated by

$$e_{FPBL} = \frac{u_\tau^2}{\alpha^*} \cos^2\left(\frac{\pi}{2}\frac{y}{\delta}\right) \tag{72}$$

Next it is noted that as $y \to 0$, $\varepsilon \to \kappa u_\tau y$. Since ε also equals $e^{1/2}\ell$, any augmentation in the e profile must be reflected in the ℓ profile as well. Therefore, ε can be rewritten as

$$\varepsilon = \Psi\, e_{FPBL}^{1/2} \cdot \Psi^{-1} \ell_{FPBL}$$

so that we must approximate the ℓ profile as

$$\ell = \Psi^{-1} \ell_{FPBL} \tag{73}$$

where ℓ_{FPBL} is the high Reynolds number FPBL length scale which empirically has been found to have the following character:

$$\ell_{FPBL} = \begin{cases} \kappa\sqrt{\alpha^*}\, y & y \le .09\delta/\kappa \\ .09\sqrt{\alpha^*}\,\delta & y > .09\delta/\kappa \end{cases} \tag{74}$$

Therefore it is only necessary to determine the value of Ψ for each particular flow. It is known that across a FPBL, $\langle -u'v'\rangle / 9/4\langle v'^2\rangle \approx 0.3$. This implies that the $\langle -u'v'\rangle$ and $\langle v'^2\rangle$ profiles are similar. It is possible that this is nearly the case for

† Note that Equation 71 fails to satisfy the boundary condition $e \to u_\tau^2/\alpha^*$ as $y \to 0$. Experience has shown that the computations correct this error in a reasonably short distance.

other flows. If this is indeed true, then it is a straightforward operation to find Ψ. If the $\langle -u'v' \rangle$ and $\langle v'^2 \rangle$ profiles are similar, then the ratio of the maximum value to the wall value is the same for each profile. This ratio has the value Ψ^2 (see Figure 8).

This procedure was studied in great detail for the three cases for which extensive data are available, viz, Andersen's adverse pressure gradient flow, Bradshaw's adverse pressure gradient flow, and FPBL flow. For example, in the Andersen case, only $\langle -u'v' \rangle$ data are available at the initial location, x=2 ft (.61 m). However, $\langle -u'v' \rangle / 9/4 \langle v'^2 \rangle \approx 0.26$ almost uniformly for $y/\delta < 3/4$ at x=6 ft (1.83 m). Hence, the profiles were assumed nearly similar at the starting location, x=2 ft (.61 m). The ratio of the maximum value of $\langle -u'v' \rangle$ to the surface shear stress at x=2 ft (.61 m) is 1.5. The e and ℓ profiles were then generated using $\Psi^2 = 1.5$. As a check on this procedure, we noted that Andersen also lists mixing-length profiles at x=2 ft (.61 m). The inferred values of ℓ are compared with the mixing-length data in Figure 9; agreement is excellent.

Sufficient data are available to directly obtain e and ℓ profiles for the Bradshaw adverse pressure gradient flow. Using Ψ=1 gives a length scale profile close to the Bradshaw data with the exception of the measured decrease in ℓ near the boundary layer edge as shown in Figure 10. The Bradshaw case was run both with the actual ℓ profile and with the profile constructed with Ψ=1; results differed only slightly. Figure 11 compares the initial e profile constructed with Ψ=1 with experimental data; the figure shows that the $\cos^2$ fit is quite accurate.

The ℓ profile used in the FPBL computations is shown in Figure 12. This profile does not quite coincide with the one constructed with Ψ=1. The difference occurs because the FPBL flow was initiated

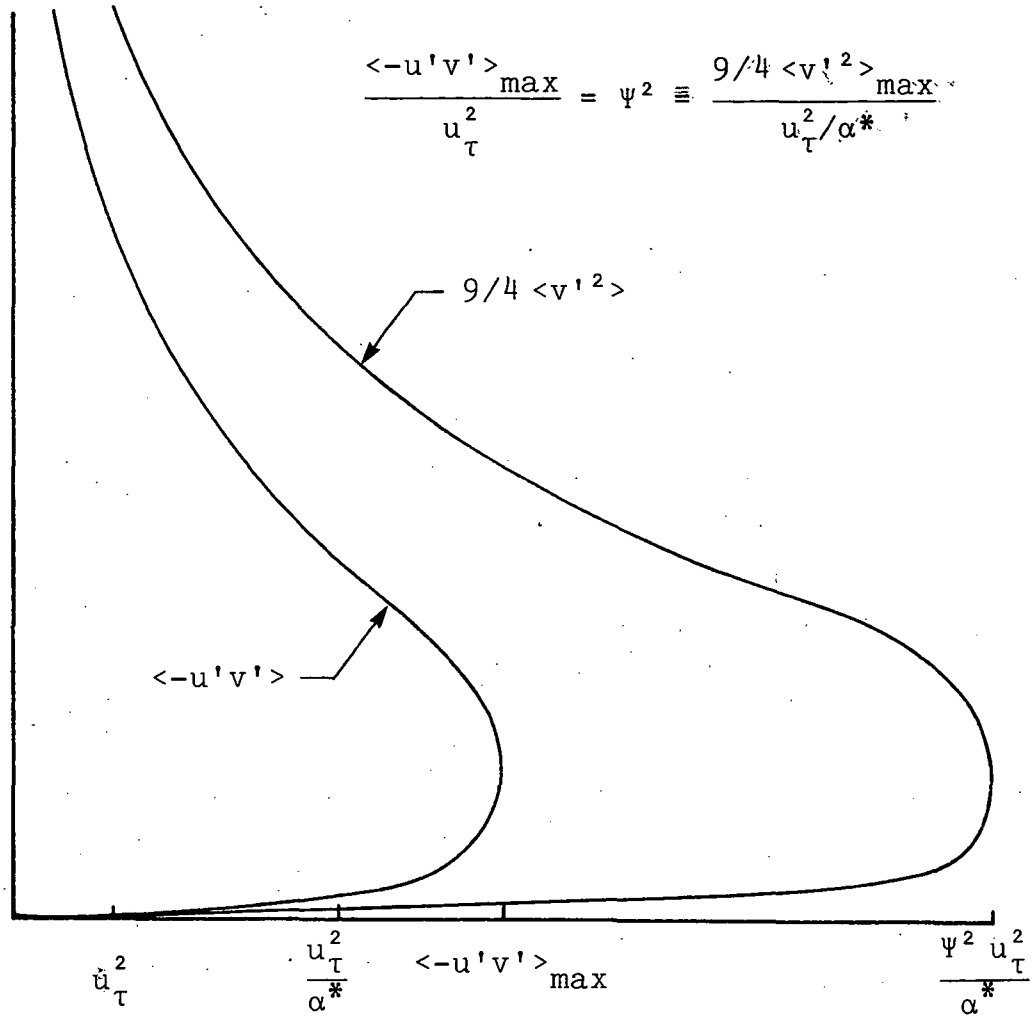

Figure 8. Use of similar <-u'v'> and e profiles to determine Ψ.

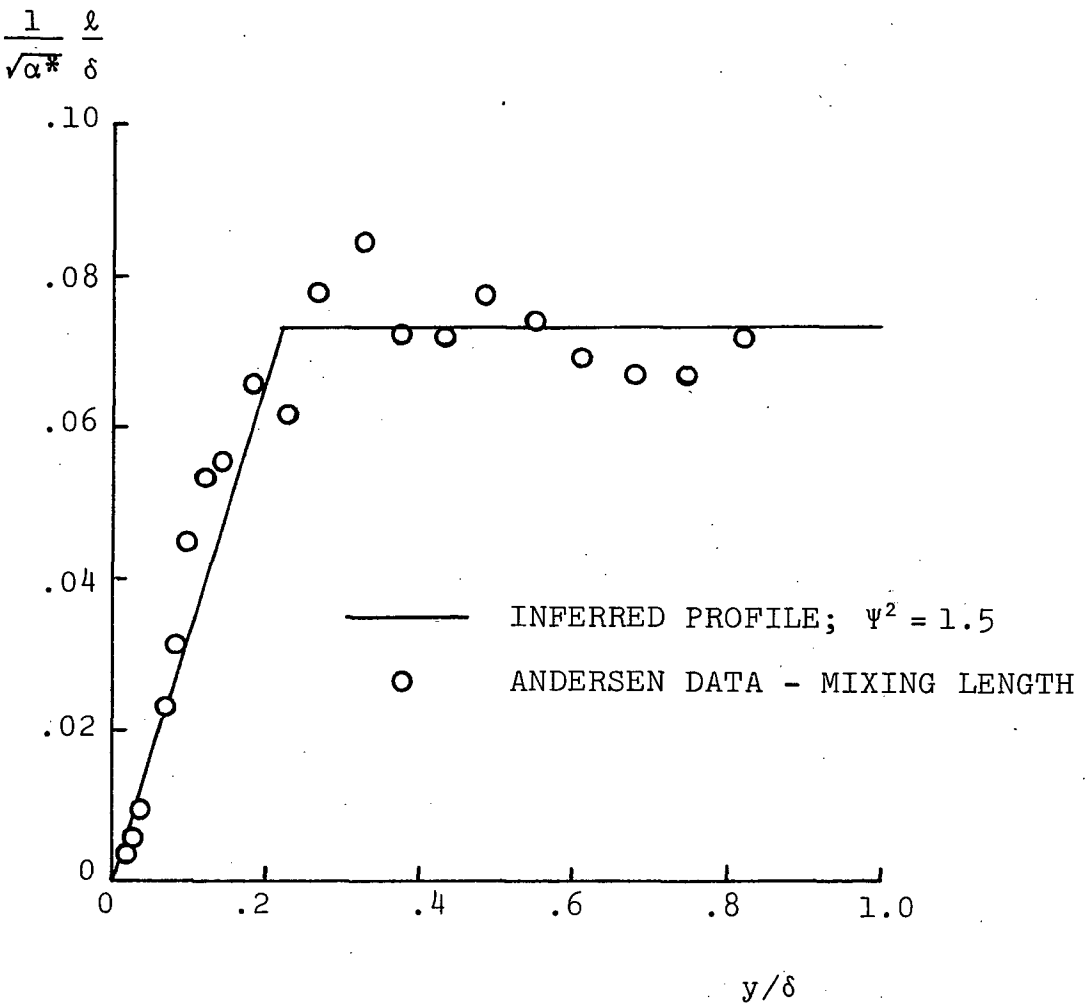

Figure 9. Comparison of inferred and measured initial mixing length profiles for the Andersen adverse pressure gradient flow; x=2 ft (.61 m).

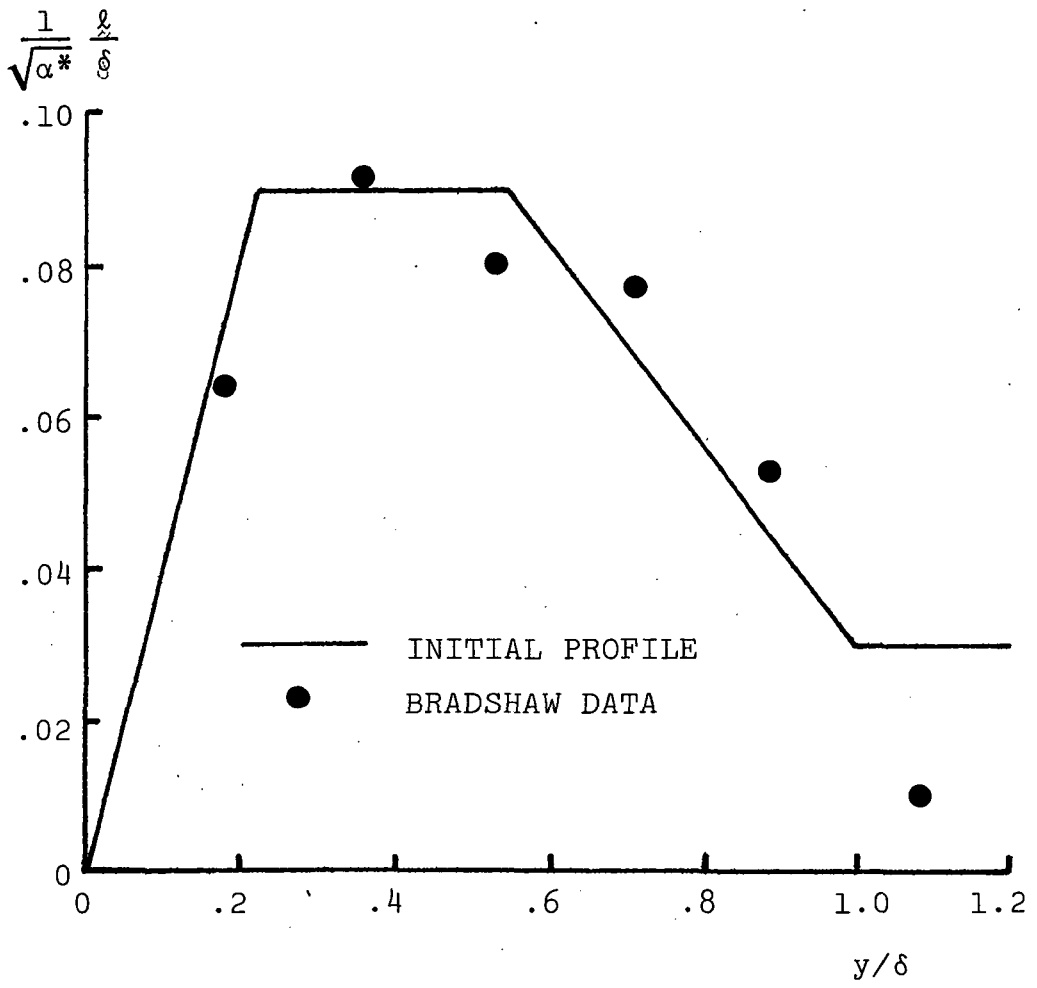

Figure 10. Initial length scale profile for the Bradshaw adverse-pressure-gradient flow; x=2 ft (.61 m).

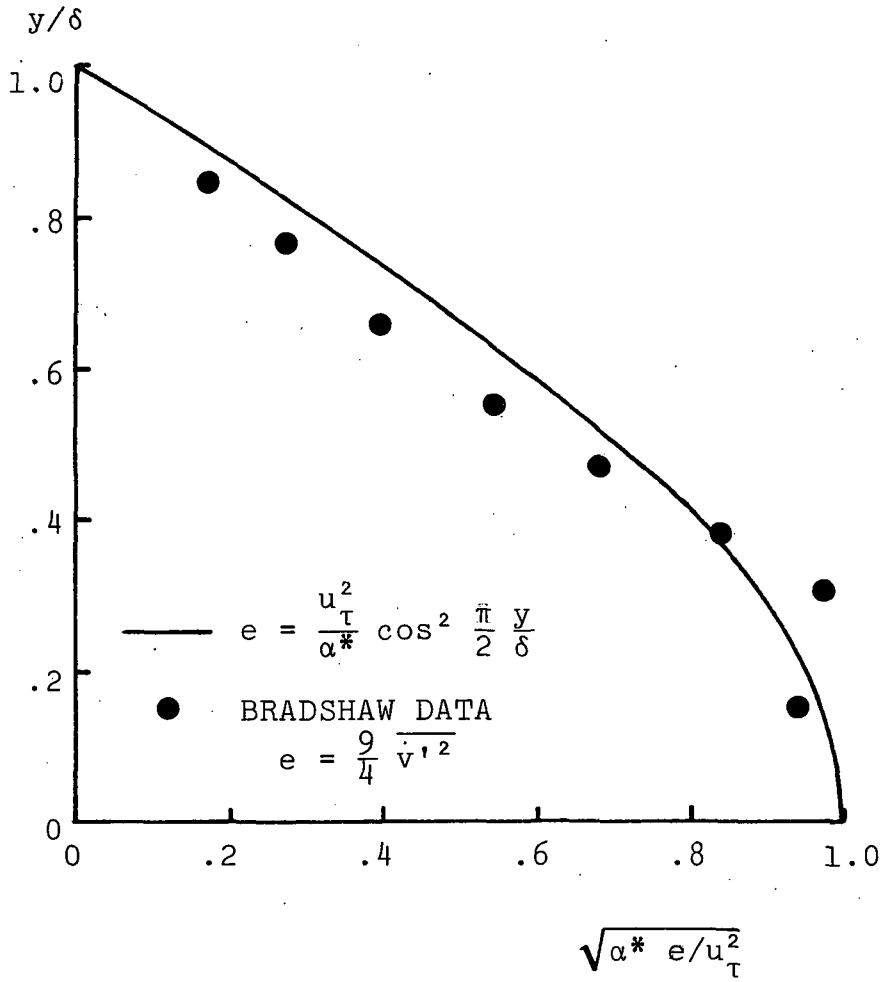

Figure 11. Initial turbulent mixing energy profile for the Bradshaw adverse-pressure-gradient flow; x=2 ft (.61 m).

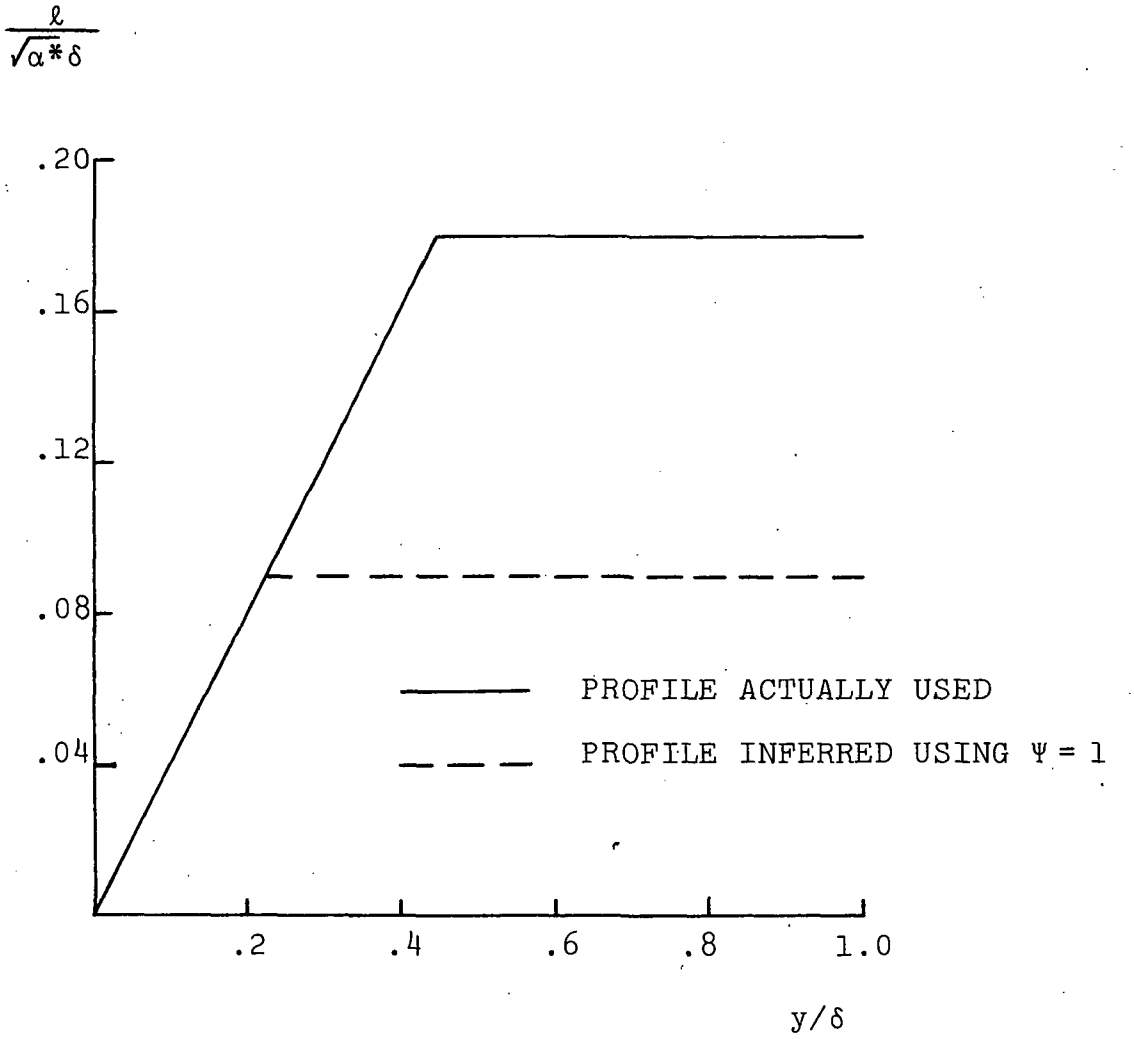

Figure 12. Initial length scale profiles used for FPBL flow.

at a very low Reynolds number; hence the peak length scale had to be enhanced to be consistent with empirical observations for low Reynolds number flows. The FPBL cases were also computed with a profile using $\Psi=1$; a transient was present in the early part of the computation but quickly settled out. The standard FPBL e profile defined in Equation 72 was used in both runs.

In summary, by using both the inferred and actual ℓ profiles, we have shown that the computations are not overly sensitive to the starting profiles as long as a reasonable peak length scale is used. Hence, the starting profiles defined by Equations 71-74 are suitable for equilibrium boundary layers. Simple FPBL profiles ($\Psi=1$) were used for both the Ludwieg-Tillmann and So-Mellor flows.

2.3.4 Computations

As noted earlier in this Subsection, the Saffman, Baseline, Ng-Spalding, and Jones-Launder turbulence models were applied to the following five flows: (1) FPBL flow; (2) Bradshaw adverse pressure gradient flow; (3) Andersen adverse pressure gradient flow; (4) Ludwieg-Tillmann favorable pressure gradient flow; (5) So-Mellor constant pressure flow over a convex wall. The results of these computations are shown in Figures 13-20.

All of the models are accurate for FPBL flow. Computed properties for the Baseline, Ng-Spalding, and Jones-Launder models agree closely with measurements, while Saffman-model predictions generally differ from corresponding data by about 10%. The Baseline model yields a velocity profile in linear coordinates which agrees most closely with experimental data (see Figure 13).

The Baseline and Ng-Spalding models yield the closest agreement between computed and measured properties for both adverse pressure gradient flows, whereas Jones-Launder-model and Saffman-model

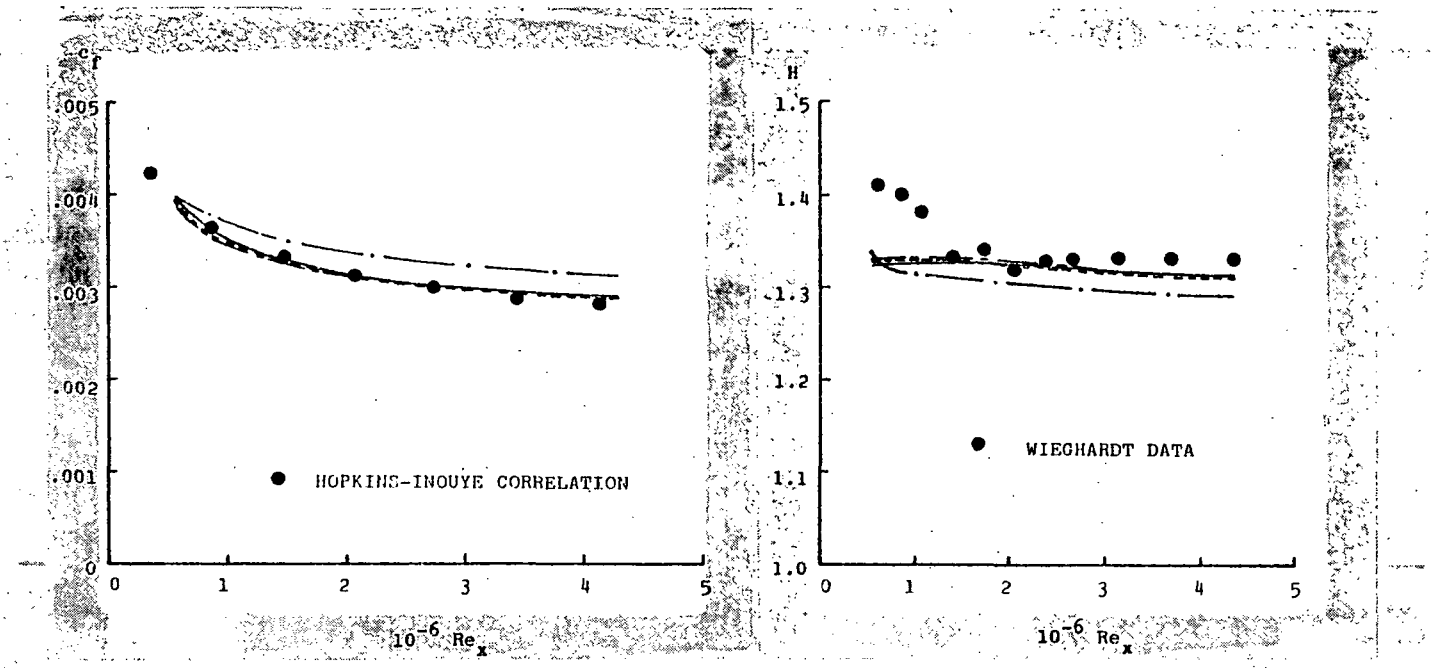

Skin Friction

Shape Factor

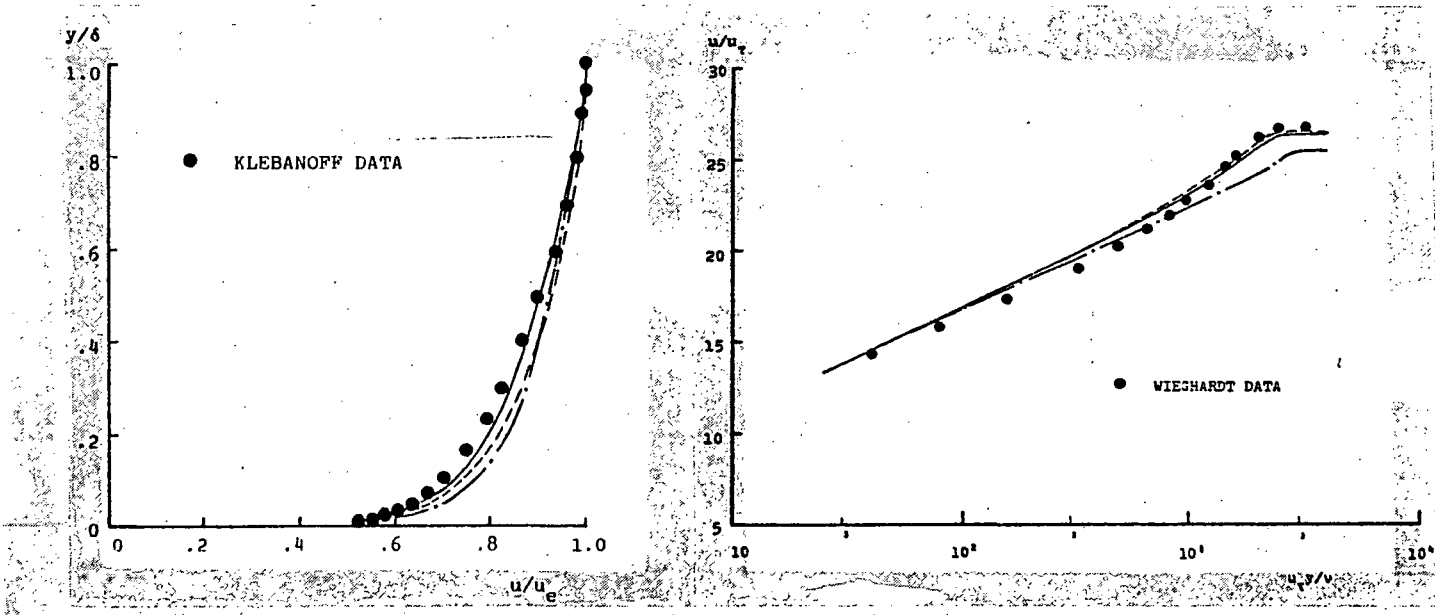

Velocity Profile; $Re_x = 4.20 \cdot 10^6$

Velocity Profile; $Re_x = 4.34 \cdot 10^6$

Figure 13. Comparison of computed and measured flow properties for flat-plate boundary-layer flow; ——— Baseline, —·— Saffman, - - - - Jones-Launder and Ng-Spalding.

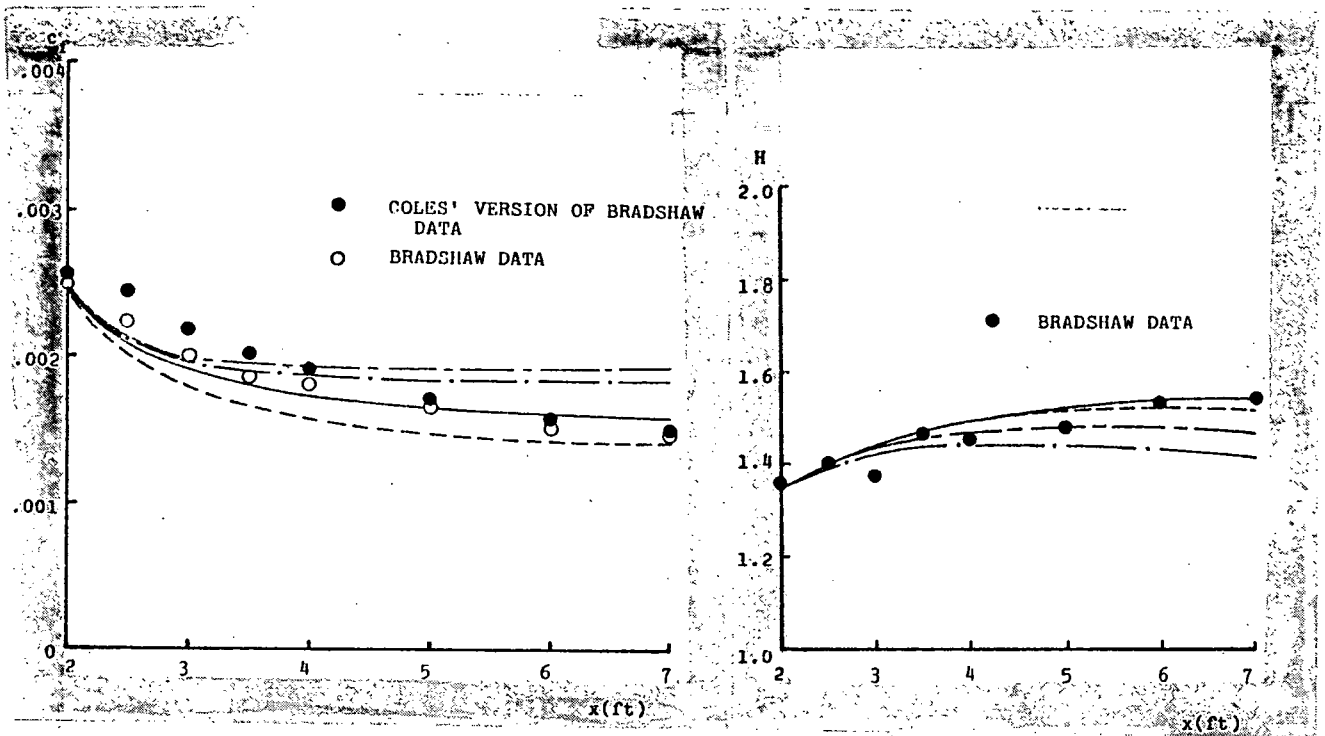

Skin Friction

Shape Factor

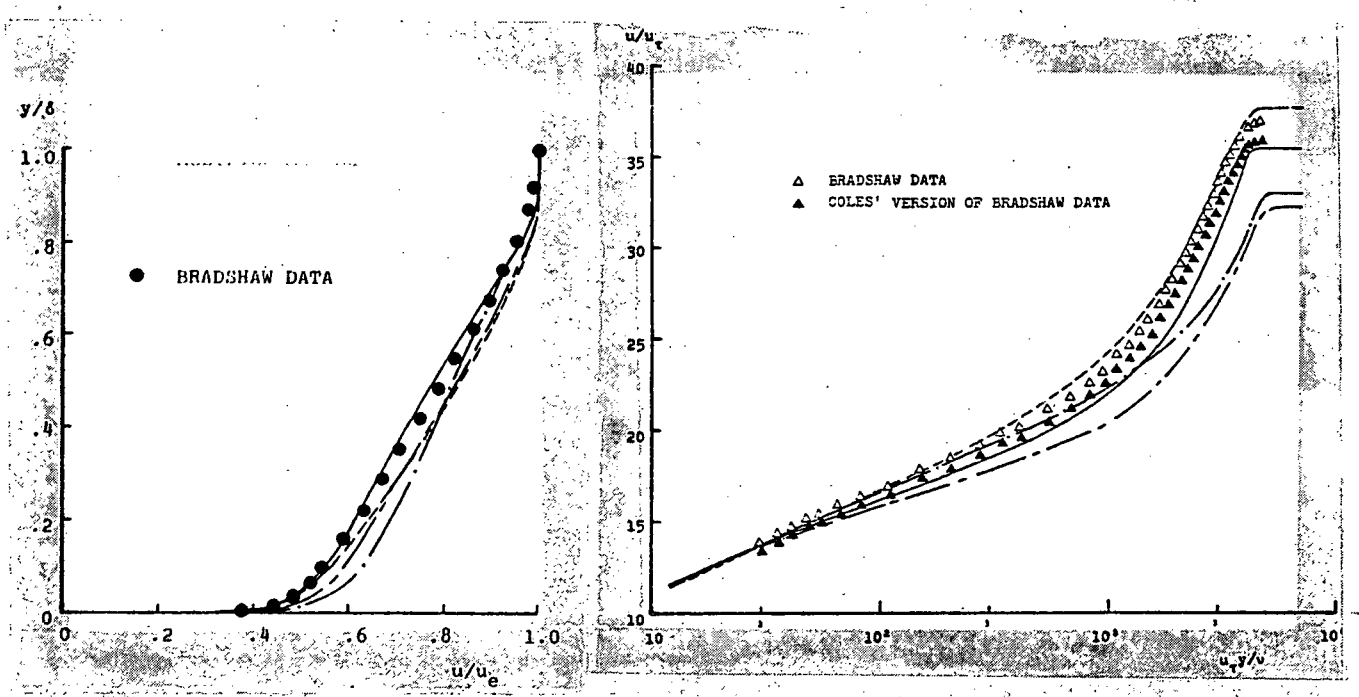

Velocity Profile; x=7 feet

Velocity Profile; x=7 feet

Figure 14. Comparison of computed and measured flow properties for the Bradshaw adverse-pressure-gradient flow; ——— Baseline, ci, ·—·— Saffman, n, - - - - Ng-Spalding, —·— Jones-Launder.

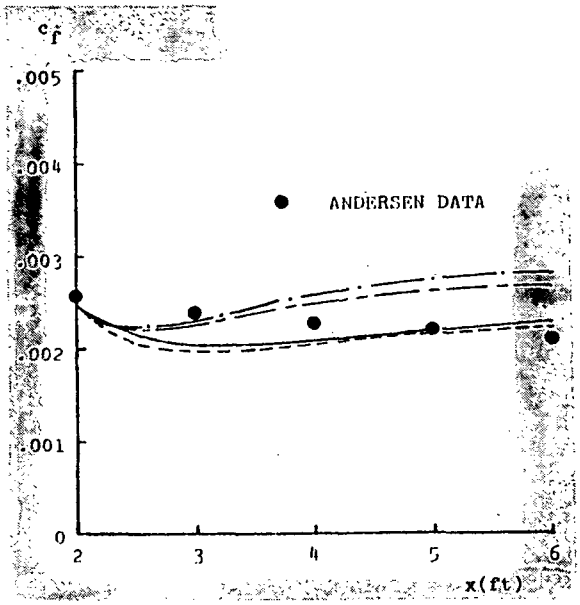

Skin Friction

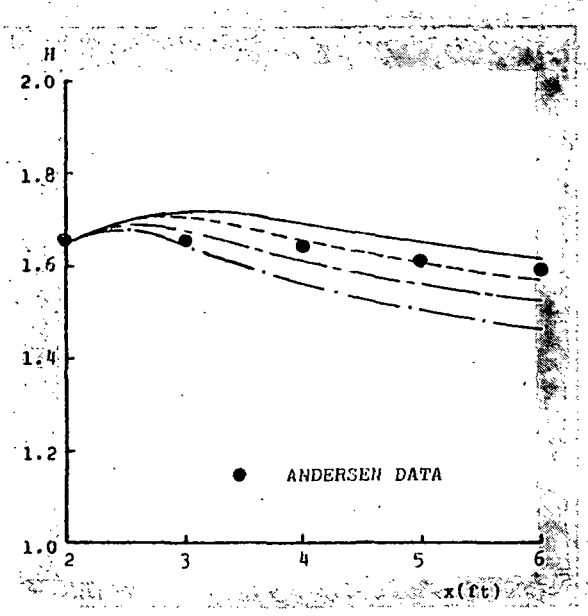

Shape Factor

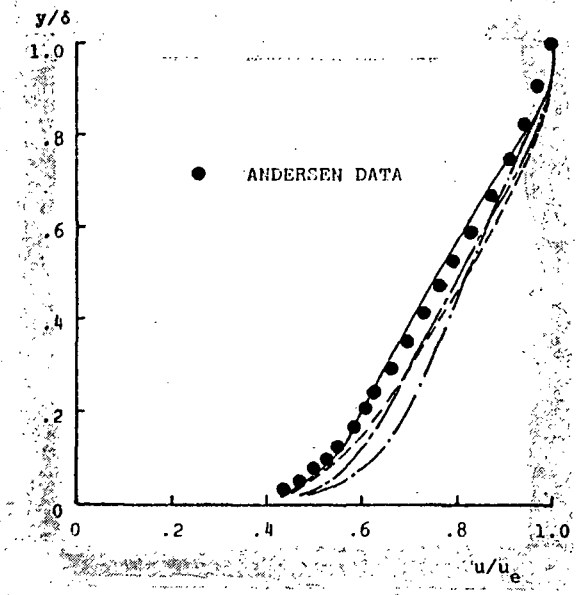

Velocity Profile; x=6 feet

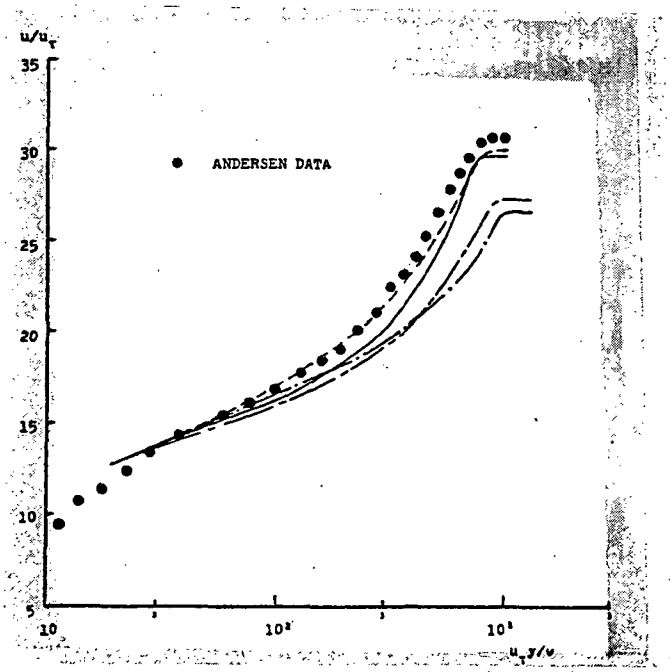

Velocity Profile; x=6 feet

Figure 15. Comparison of computed and measured flow properties for the Andersen adverse-pressure-gradient flow; ——— Baseline, —·—·— Saffman, ---- Ng-Spalding, —-—- Jones-Launder.

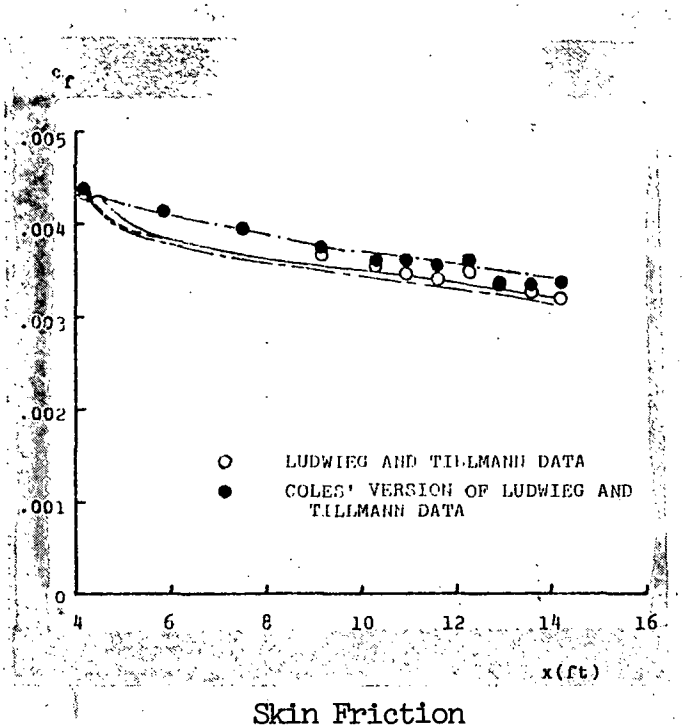

Skin Friction

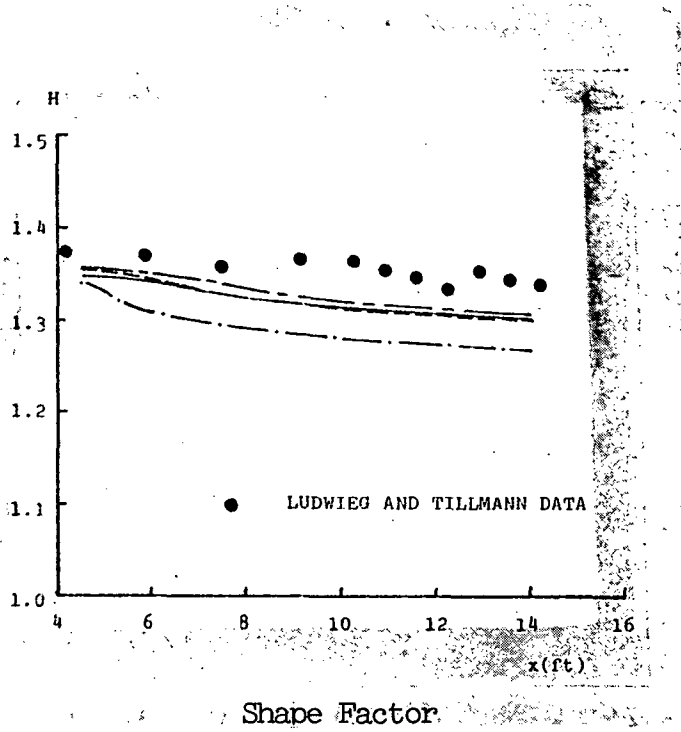

Shape Factor

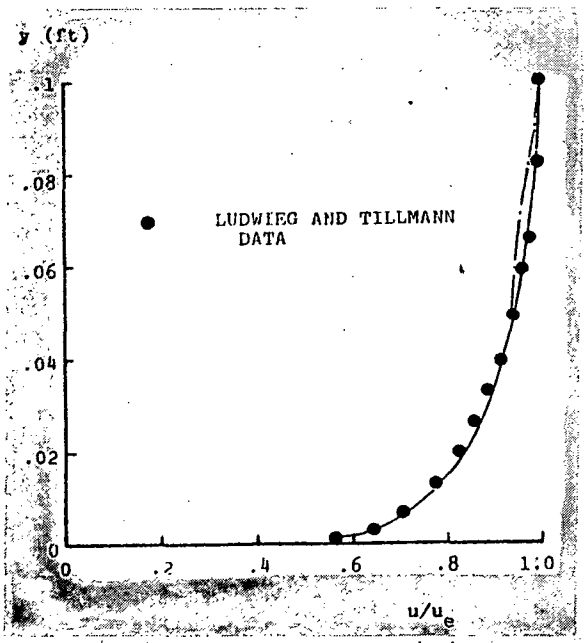

Velocity Profile; x=14.4 feet

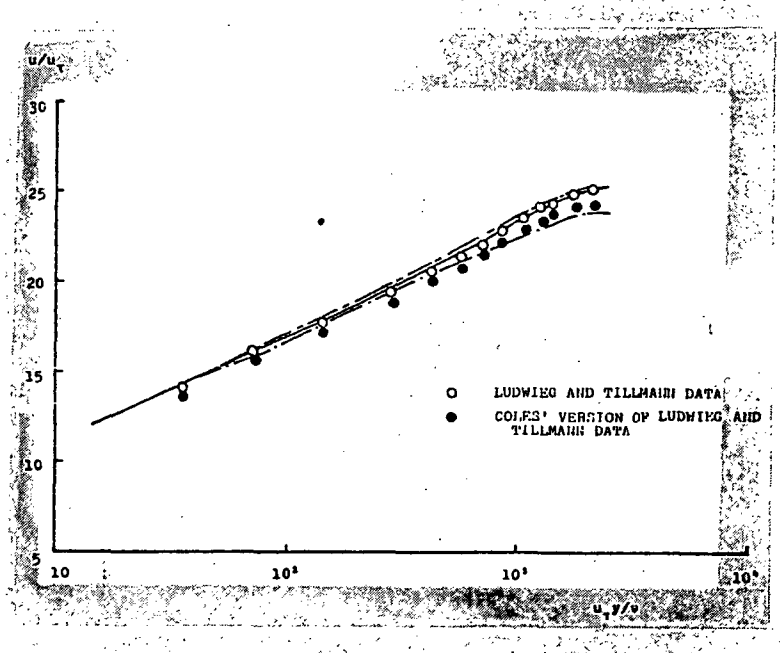

Velocity Profile; x=14.4 feet

Figure 16. Comparison of computed and measured flow properties for the Ludwieg-Tillmann favorable-pressure-gradient flow; ——— Baseline, —·—·— Saffman, - - - - - Ng-Spalding, ——- —— Jones-Launder.

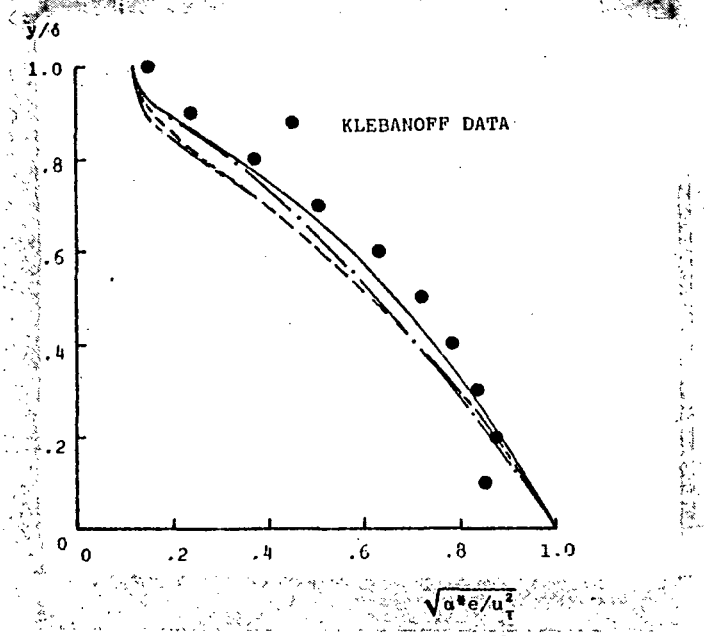

FPBL Flow; $Re_x = 4.20 \cdot 10^6$

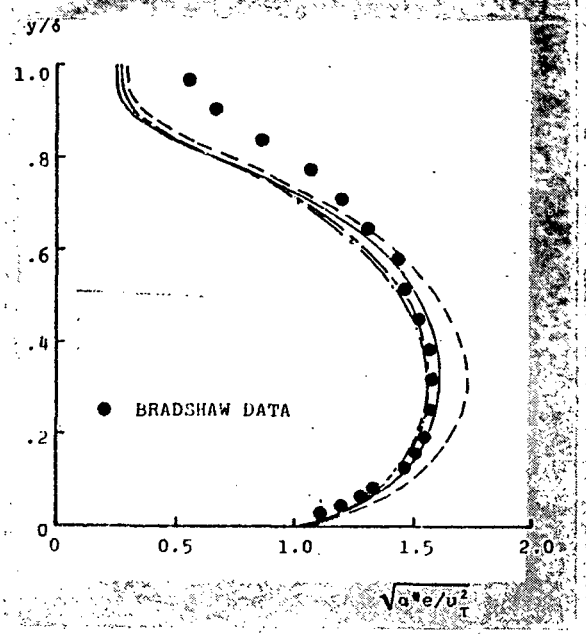

Bradshaw Adverse-Vp flow; x=7 feet

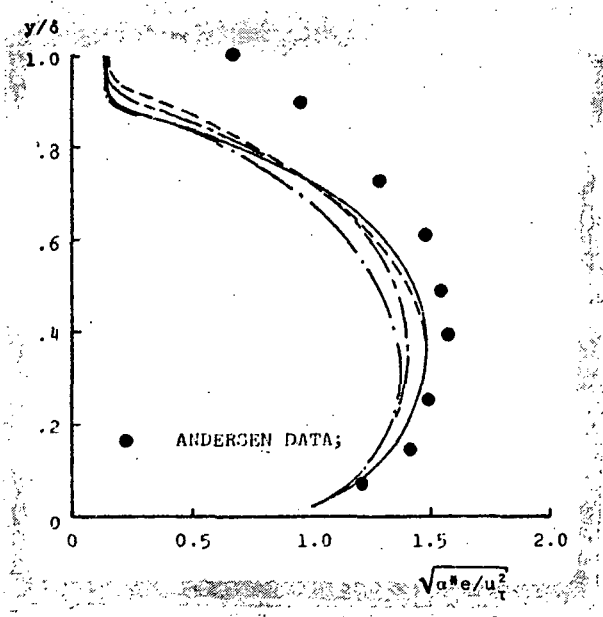

Andersen Adverse-Vp flow; x=6 feet

Figure 17. Comparison of computed and measured ($e = 9/4\langle v'^2 \rangle$) turbulent mixing energy profiles; ——— Baseline, —·—·— Saffman, - - - - Ng-Spalding, ——— Jones-Launder.

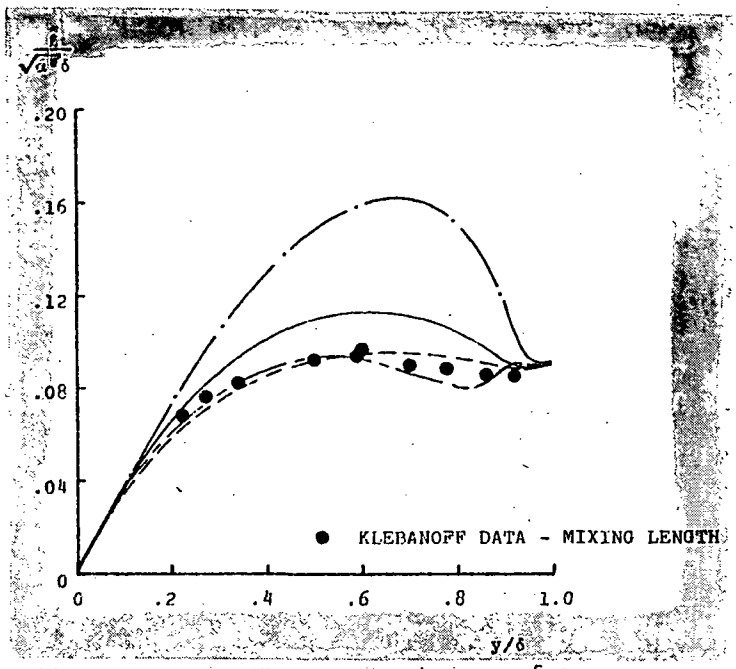

FPBL Flow; $Re_x = 4.20 \cdot 10^6$

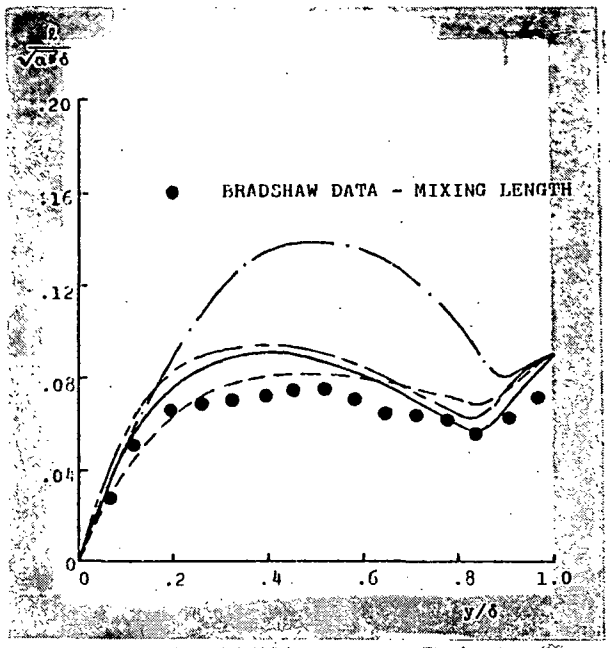

Bradshaw Adverse-Vp Flow; x=7 feet

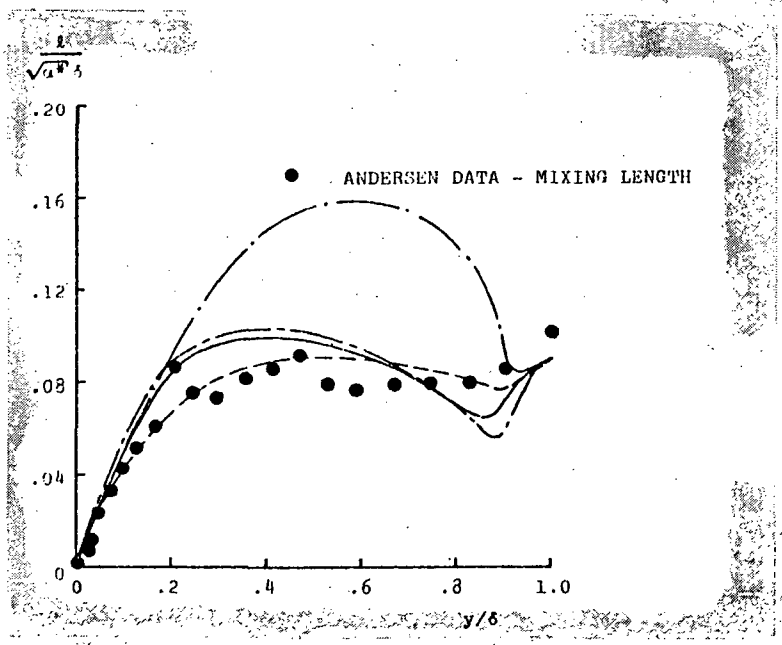

Andersen Adverse-Vp Flow; x=6 feet

Figure 18. Comparison of computed and measured length scale profiles; ——— Baseline, —·—·— Saffman, - - - - Ng-Spalding, ——— Jones-Launder.

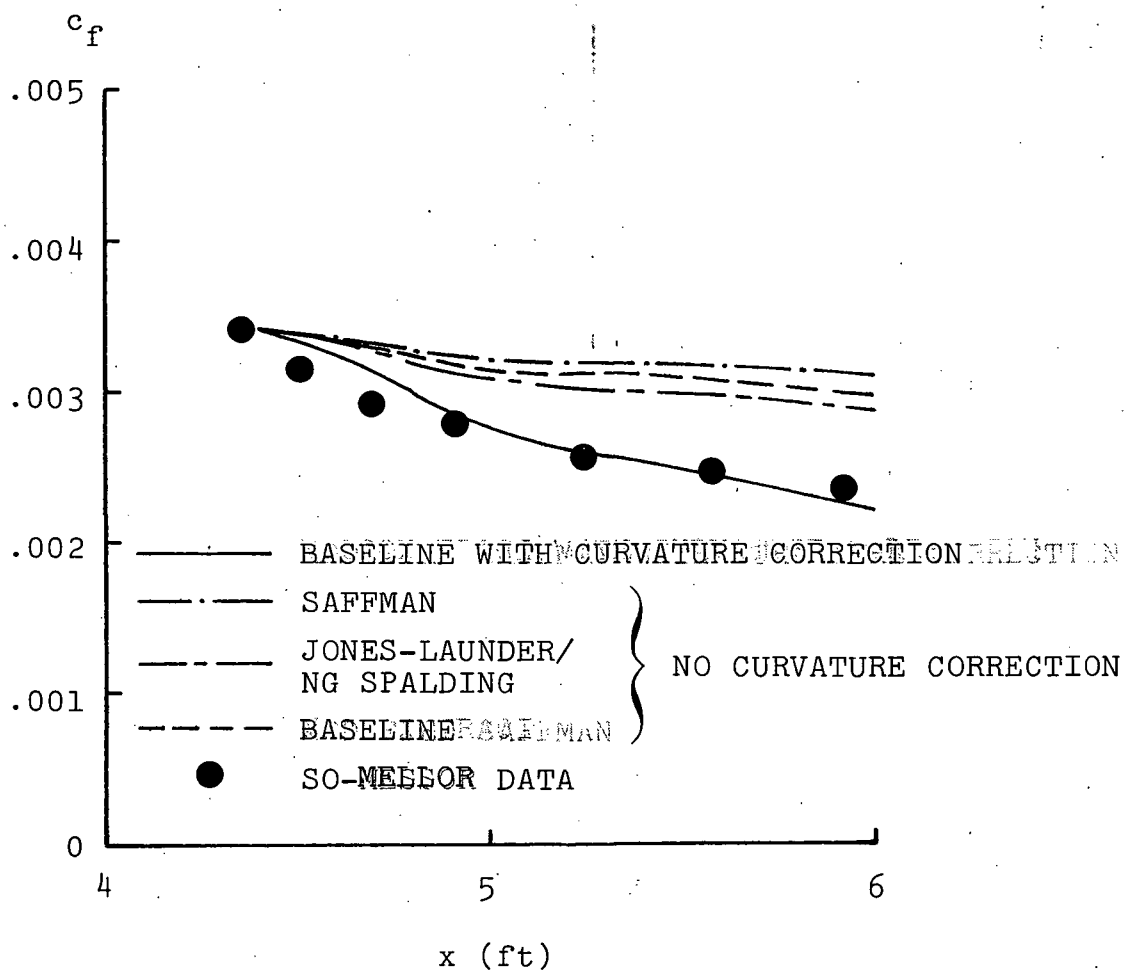

Figure 19. Comparison of computed and measured skin friction for flow over a curved surface.

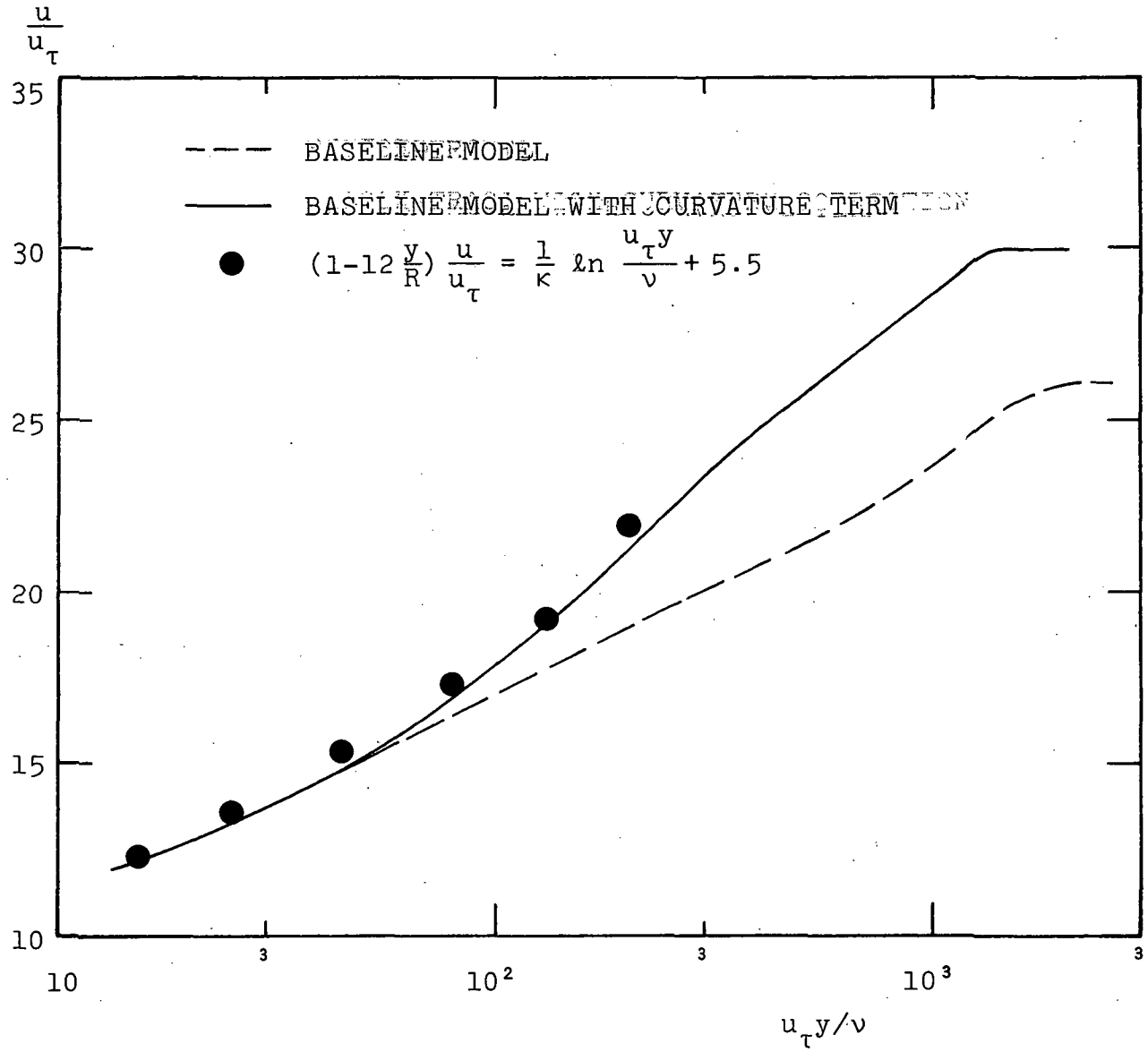

Figure 20. Comparison of computed velocity profiles with the law of the wall for flow over a curved surface with radius of curvature, R.

predictions differ from the data substantially.† Most particularly, note the excellent agreement between experimental and computed velocity profiles in linear coordinates for the Baseline model (see Figures 14 and 15). The Ng-Spalding-model velocity profiles in linear coordinates do not agree nearly as well with the data. However, with the exception of the velocity profile in linear coordinates, the Ng-Spalding model yields closest overall agreement to the Andersen data.

For the Ludwieg-Tillmann favorable pressure gradient flow, the Baseline, Jones-Launder and Ng-Spalding models yield predictions very close to the experimental data (Figure 16). The Saffman model does not do quite as well; the velocity profile in linear coordinates serves as a reminder of the Saffman model's deficiency in the defect layer.

Figures 17 and 18 compare computed e and ℓ profiles with experimental data for $9/4 \langle v'^2 \rangle$ and mixing length, respectively. Consistent with the defect-layer analysis of Subsections 2.1 and 2.2, in all three cases shown the Baseline model has length scale profiles much closer to the measured mixing-length profiles than does the Saffman model. All models do a good job of reproducing the $9/4 \langle v'^2 \rangle$ data indicating that the efficacy of a two-equation model is controlled by the accuracy with which the turbulent length scale can be computed.

Of these four flows, the models do poorest on the Andersen flow. However, the Andersen flow has a relatively low Reynolds number and, without suitable viscous corrections, the models are realistically only applicable at high Reynolds numbers. This is best exemplified in Figure 15. The Baseline and Ng-Spalding models

† The Saffman-model solutions generated by Wilcox and Chambers[1] (see Figure 1) were done with a value for $\ell_e/\sqrt{\alpha^*}\delta$ of less than .02; although accurate skin friction and shape factor were obtained, the inflected profiles shown in Figure 1 attended the very small value of ℓ_e.

stray from skin friction data early in the computation. However, agreement is much better by the end of the computation, where the boundary layer is finally approaching a well-developed turbulent state.

As a final part of the comparisons, the models' ability to predict effects of streamline curvature was tested. Computed skin friction for So-Mellor's constant pressure flow over a convex wall (Figure 19) shows that two-equation models in their original form fail for flows with streamline curvature. However, as shown by Wilcox and Chambers,[1] better agreement between theory and experiment can be obtained by adding a curvature correction term to the turbulent-mixing-energy equation. Using this curvature term, the So-Mellor flow was recomputed with the Baseline model. As shown in Figures 19 and 20, close agreement between calculated and measured skin friction and velocity profiles is then obtained. The correction term will be discussed in detail in Section 3 when other flows with streamline curvature are considered.

2.3.5 Summary

For the flows without streamline curvature, the Baseline and the Ng-Spalding models yield results in much closer agreement with the data than do the Jones-Launder and Saffman models. Furthermore, the Baseline model's velocity profiles in linear coordinates are in very close accord with the data and consistently closer than any of the other models'. Hence, the Baseline model appears to be the most accurate of the various two-equation models. Computation of the curved-wall case shows that none of the models in their original form accurately predicts effects of streamline curvature. However, by adding a streamline curvature correction term, accurate predictions can be obtained with the Baseline model for flow over a convex wall. This curvature correction will be shown to work well for a number of flows with curved streamlines in Section 3.

2.4 VISCOUS COMPUTATIONS

The utility of the Baseline model would be severely limited if it were applicable only where the law of the wall holds close to a boundary. It would be inapplicable for transitional and separating flows for example and, more generally, it would perform poorly for boundary layers with arclength Reynolds numbers less than a million. Hence, encouraged by the success of the Baseline model in the matching computations, viscous calculations were performed. The objective of performing viscous computations is to test the model's ability to predict low Reynolds number effects. The four flows with no streamline curvature considered in the preceding Subsection were recomputed. In addition, a viscous solution of a flat plate boundary layer with uniform blowing was obtained. Table 2 lists the specific flows considered and the corresponding data sources.

Table 2. Incompressible Viscous Calculations

FLOW	DATA SOURCES
• Flat plate boundary layer • Bradshaw adverse pressure gradient • Andersen adverse pressure gradient • Ludwieg-Tillmann favorable pressure gradient	Same as in matching calculations (Table 1).
• Andersen flat plate with uniform blowing	Andersen[4] data.

In order to proceed with viscous computations, viscous modifications to the model equations had to be included. Wilcox and Traci[17] used perturbation techniques to study the sublayer of a turbulent boundary layer. They found that in addition to adding molecular diffusion to the momentum and model equations, the following straightforward modifications to α and α^* are needed to obtain accurate viscous computations:

$$\left.\begin{aligned} \frac{\alpha^*}{\alpha^*_\infty} &= 1 - (1-\lambda)\, e^{-2Re_T} \\ \frac{\alpha}{\alpha_\infty} &= 1 - (1-\lambda)\, e^{-Re_T/2} \end{aligned}\right\} \tag{75}$$

where

$$\lambda = 1/11 \ , \quad \alpha^*_\infty = 3/10 \ , \quad \alpha_\infty = \beta/\alpha^*_\infty - 2\sigma\kappa^2 = .3319$$

and Re_T is the turbulent Reynolds number defined by

$$Re_T = \frac{e}{\omega\nu} \tag{76}$$

Boundary-layer-edge boundary conditions and initial profiles were the same as those used in the preceding subsection; for the blowing case, FPBL initial profiles were used. At the surface, the no-slip boundary condition was imposed while e and ω were given by

$$\left.\begin{aligned} e &= 0 \\ \omega &= \frac{S}{\alpha^*}\,\frac{u_\tau^2}{\nu} \end{aligned}\right\} \tag{77}$$

The quantity S is a function of surface roughness and blowing velocity and, as shown by Traci,[18]

$$S^{-1} = S_B^{-1} + S_R^{-1} \tag{78}$$

where

$$S_B = 6\,\frac{(v_w/u_\tau)^{-1}}{1 + v_w/u_\tau} \tag{79}$$

and

$$S_R = \left(\frac{36}{ku_\tau/\nu}\right)^2 + \left(\frac{8}{ku_\tau/\nu}\right)^{1/2} \qquad (80)$$

In Equations 79 and 80, v_w is blowing velocity and k is roughness height. The nonblowing computations were performed with very small values of k to simulate a perfectly smooth wall; we have found empirically that the smooth wall limit in which $S \to \infty$ is very closely approximated with finite values of S in excess of about 300.

Figures 21 through 27 show the results of the viscous computations for the boundary layers with no mass injection. The viscous solutions for the FPBL, Bradshaw adverse pressure gradient, Andersen adverse pressure gradient, and Ludwieg-Tillmann flows are very similar to the inviscid solutions (Figures 13-18). For the blowing case, skin friction corresponds well with data, computed shape factor is within 10% of data, and velocity profiles are within 15% of the data (Figure 25).

Results of the FPBL and Andersen adverse pressure gradient flows best exhibit the model's ability to accurately predict viscous effects. For FPBL flow, Figure 21 shows close agreement between the predicted and experimental shape factor for a wide range of Reynolds numbers. Additionally, the figure exhibits the Baseline model's ability to handle viscous effects by displaying velocity profiles in sublayer coordinates for three different Reynolds numbers. Note that the Andersen adverse pressure gradient calculation was initiated near the leading edge of the plate, whereas the matching calculation was begun at a plate length of 2 ft (.61 m). By including viscosity and integrating from near the leading edge, the results are in much closer agreement with measurements than those obtained by matching to the law of the wall. Figure 23 shows velocity profiles in sublayer coordinates for two different Reynolds numbers.

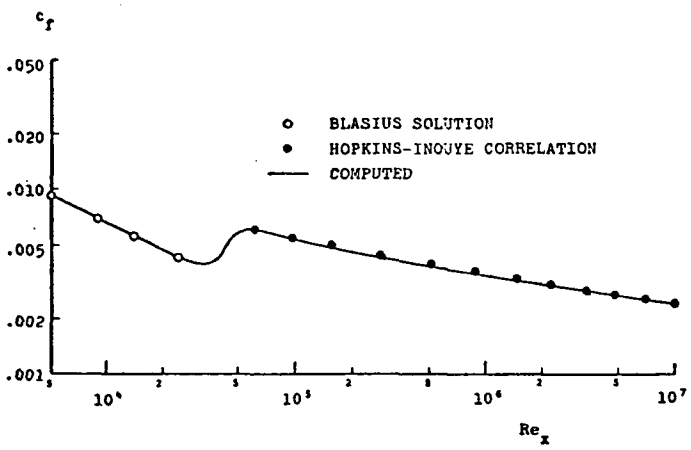

Skin Friction

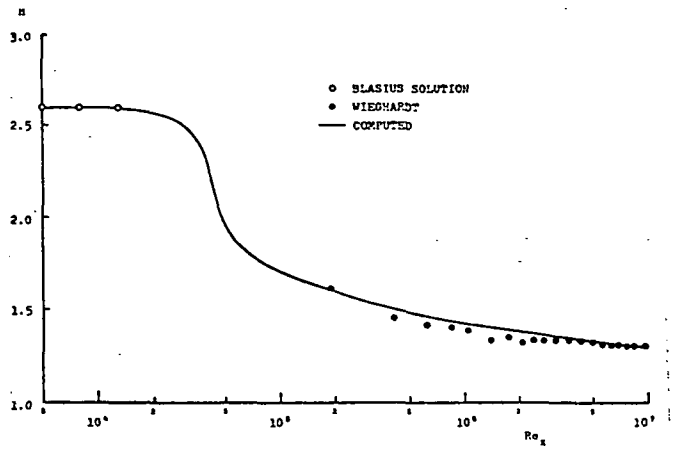

Shape Factor

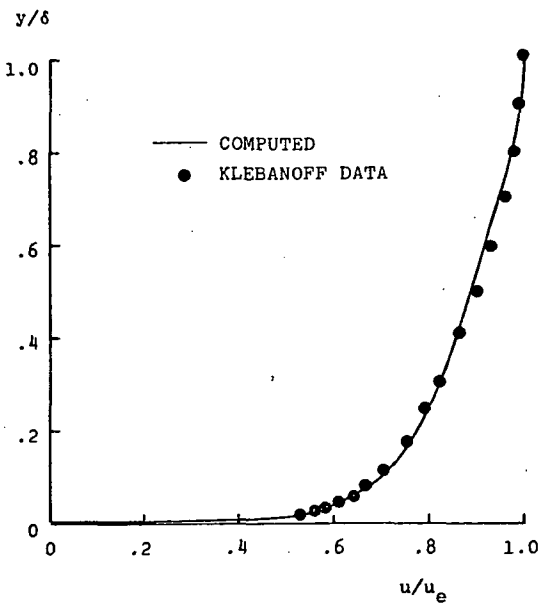

Velocity Profile; $Re_x = 4.20 \cdot 10^6$

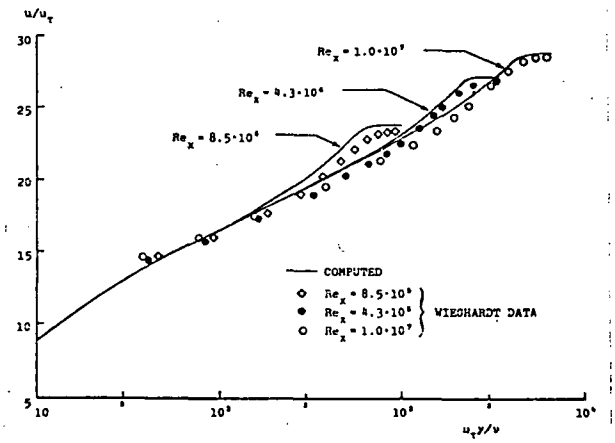

Velocity Profiles

Figure 21. Comparison of computed and measured flow properties for flat-plate boundary-layer flow.

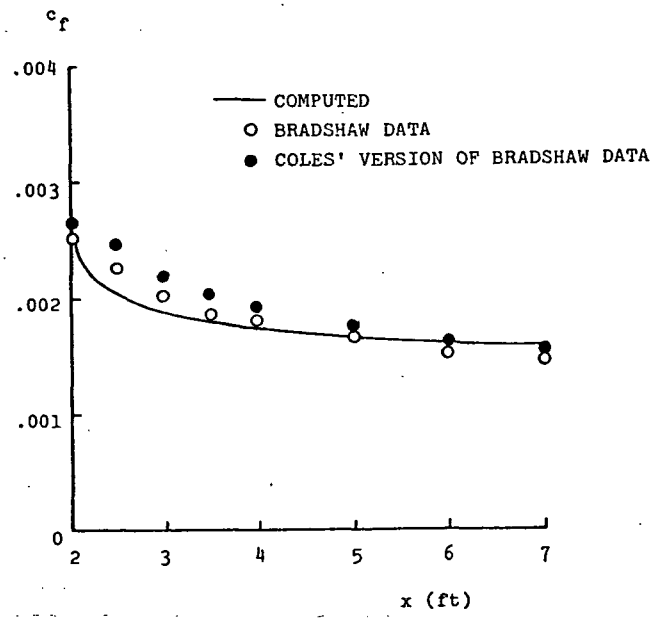

SkSkin Friction

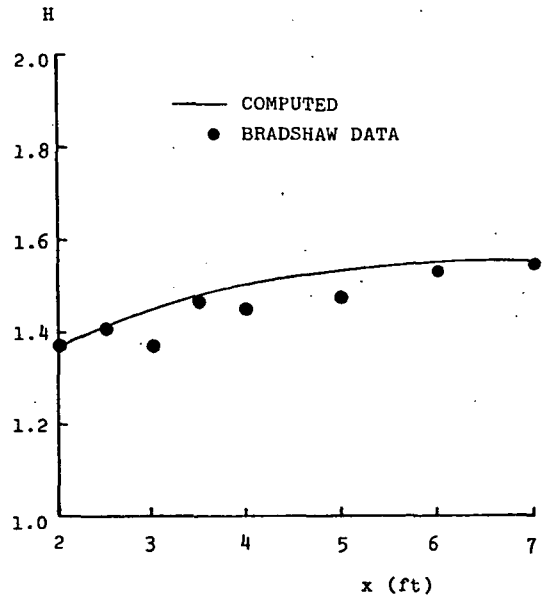

Shape Factor

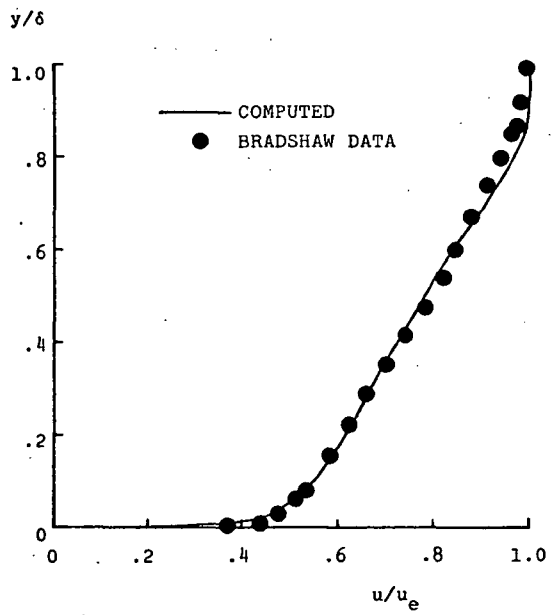

Velocity Profile; x=7 feet

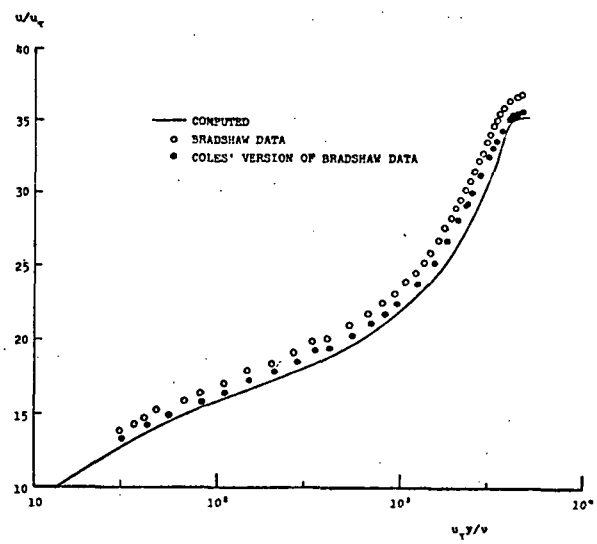

Velocity Profile; x=7 feet

Figure 22. Comparison of computed and measured flow properties for the Bradshaw adverse pressure gradient flow.

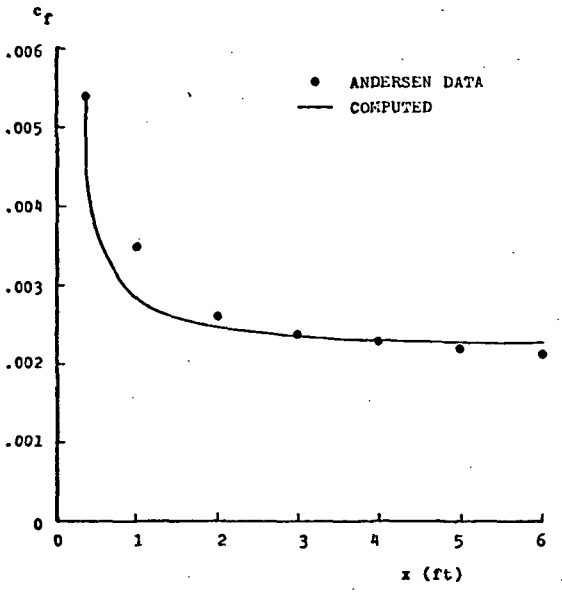

Skin Friction

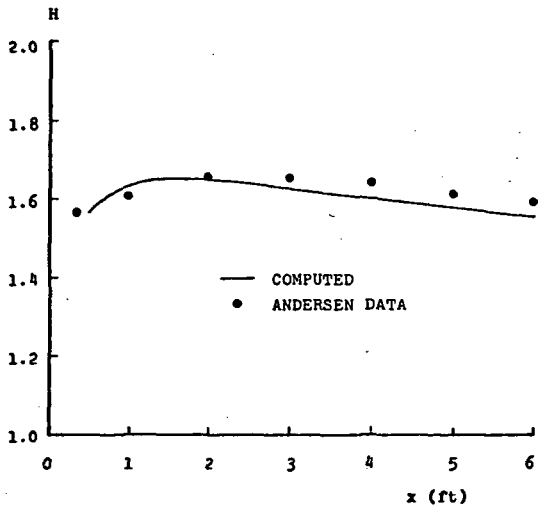

Shape Factor

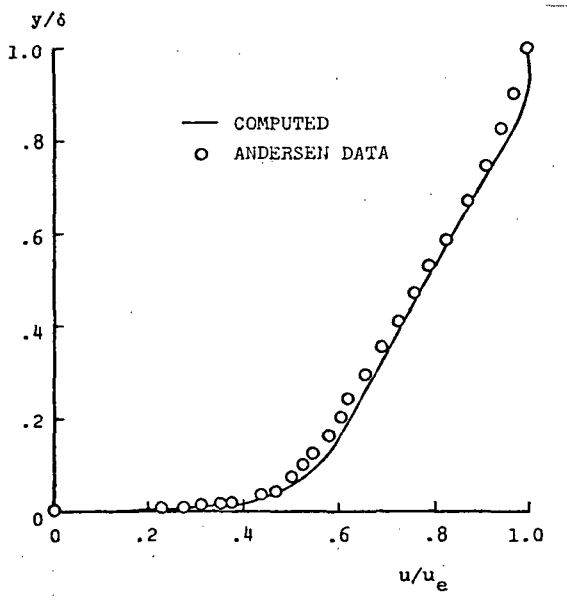

Velocity Profile; x=6 feet

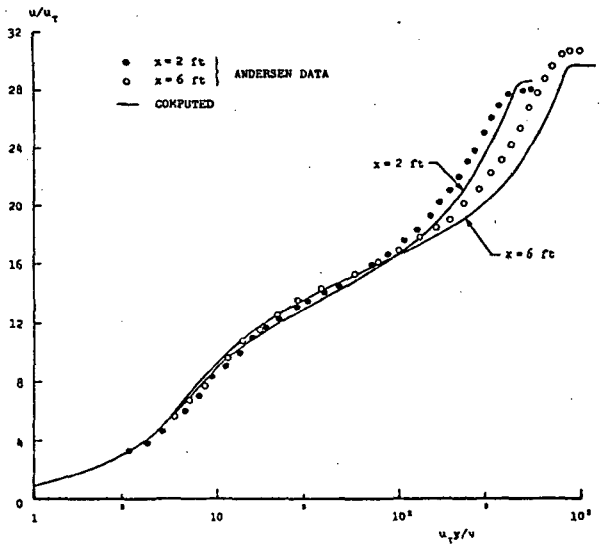

Velocity Profiles

Figure 23. Comparison of computed and measured flow properties for the Andersen adverse pressure gradient flow.

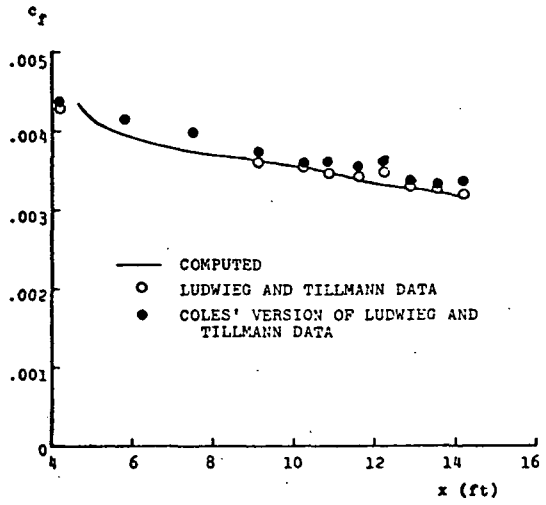

Skin Friction

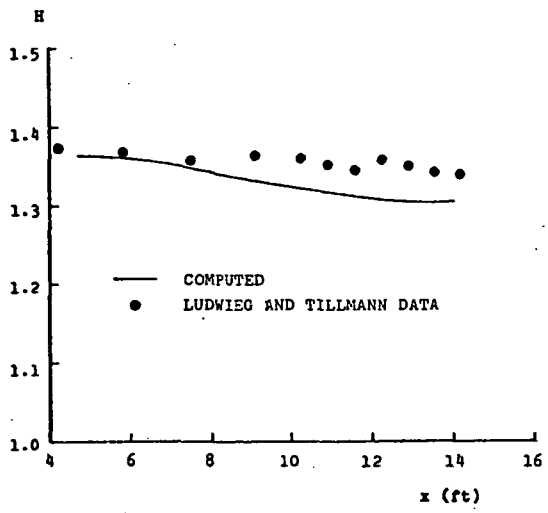

Shape Factor

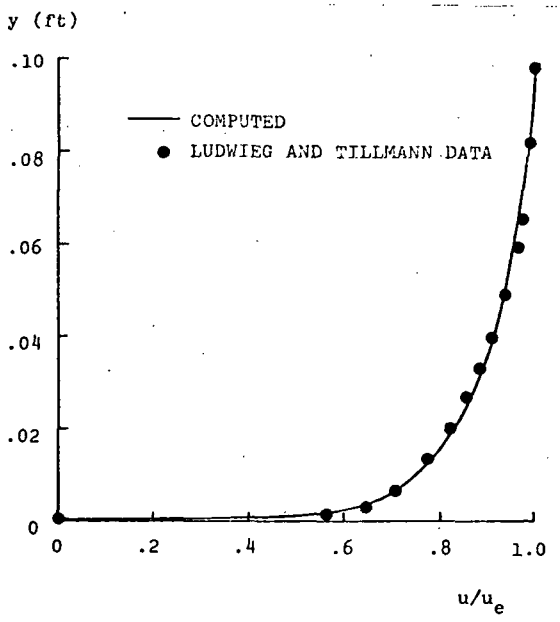

Velocity Profile; x=14.4 feet

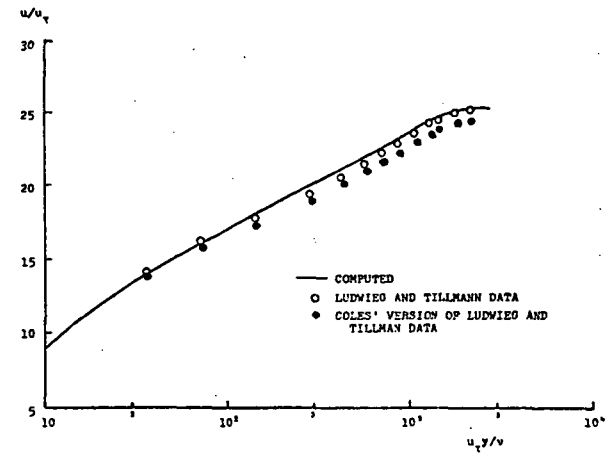

Velocity Profile; x=14.4 feet

Figure 24. Comparison of computed and measured flow properties for the Ludwieg-Tillmann favorable pressure gradient flow.

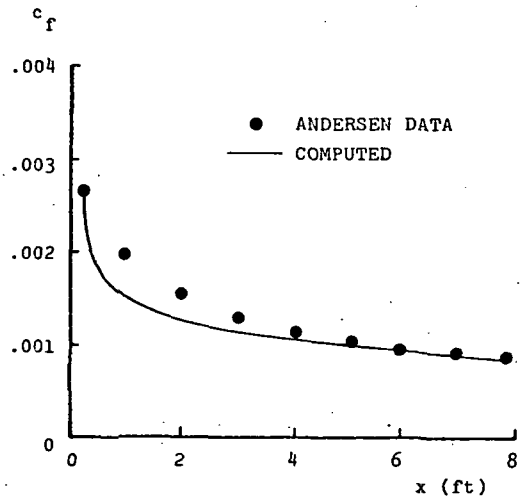

Skin Friction

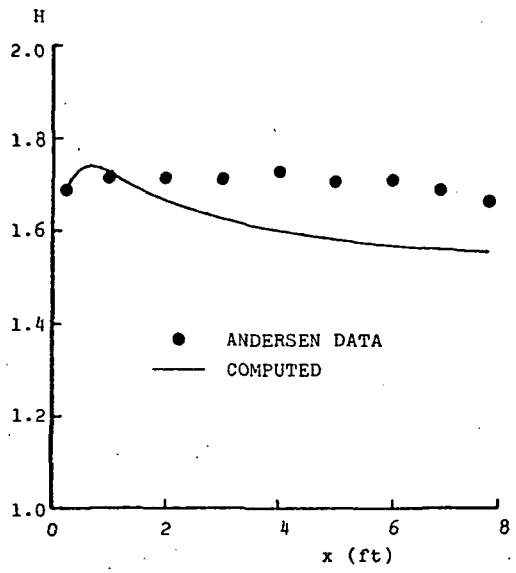

Shape Factor

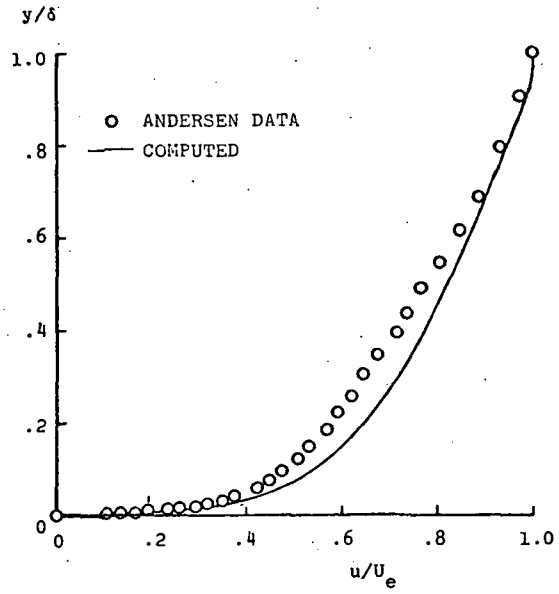

Velocity Profile; x=90 inches

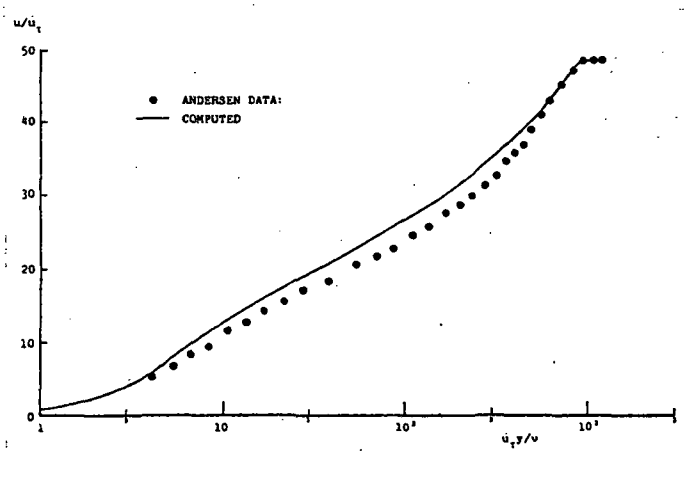

Velocity Profile; x=90 inches

Figure 25. Comparison of computed and measured flow properties for flat-plate boundary-layer flow with uniform blowing.

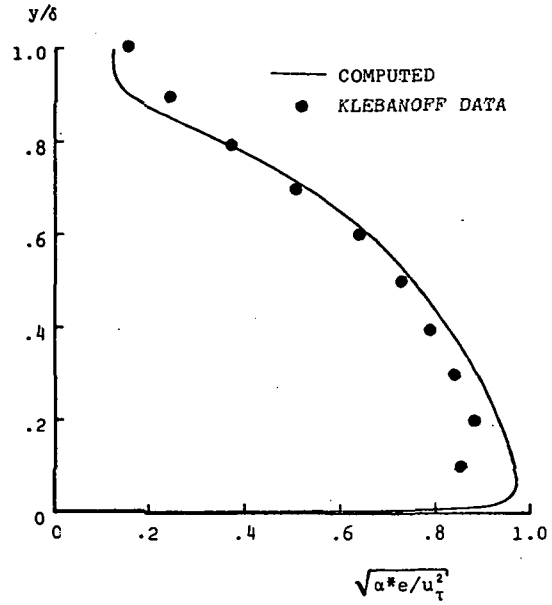

FPBL Flow; $Re_x = 4.20 \cdot 10^6$

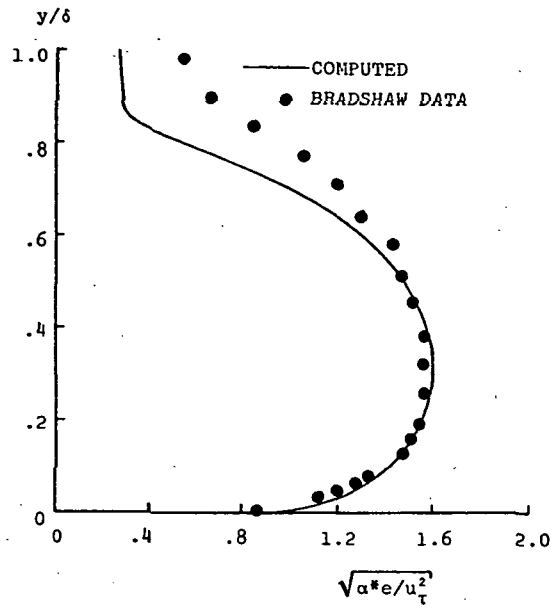

Bradshaw Adverse-Vp Flow; x=7 feet

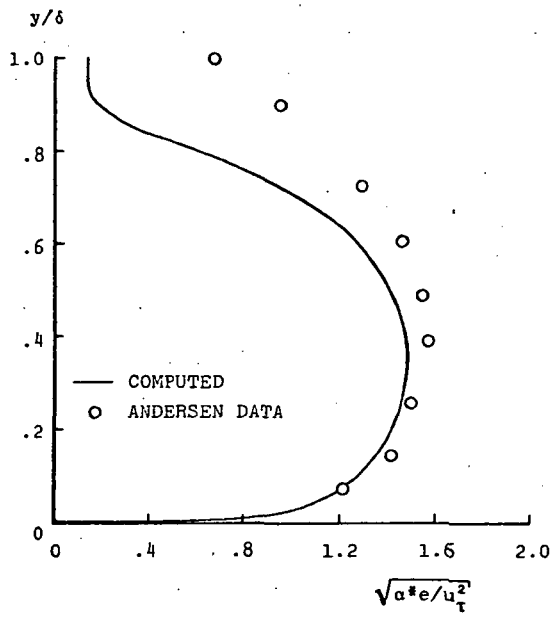

Andersen Adverse-Vp Flow; x=6 feet

Figure 26. Comparison of computed and measured ($e = 9/4\langle v'^2 \rangle$) turbulent mixing-energy profiles.

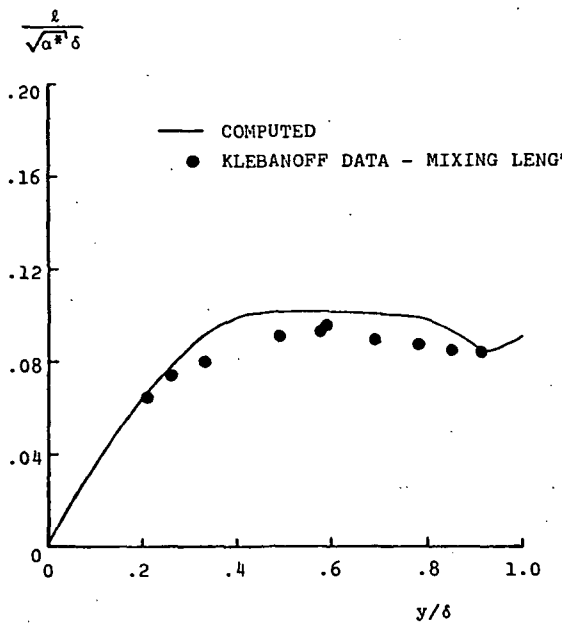

FPBL Flow; $Re_x = 4.20 \cdot 10^6$

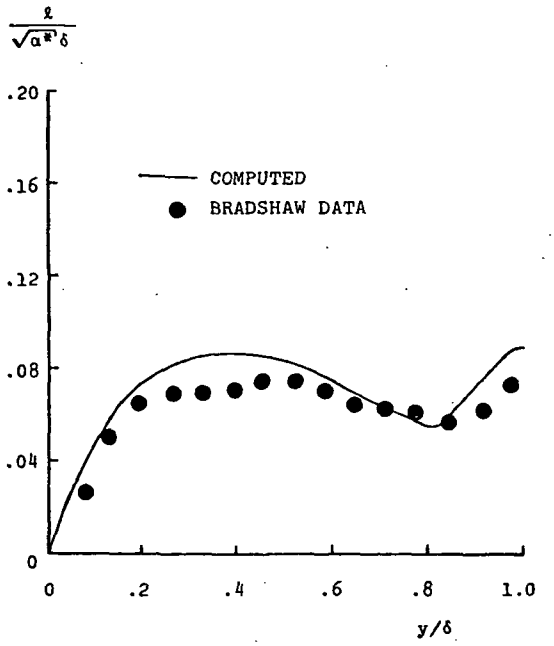

Bradshaw Adverse-∇p Flow; x=7 feet

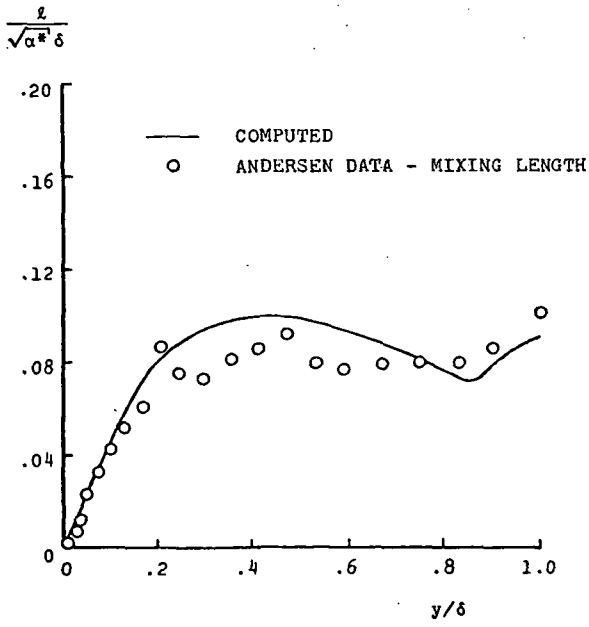

Andersen Adverse-∇p Flow; x=6 feet

Figure 27. Comparison of computed and measured length scale profiles for flat-plate boundary-layer flow.

Results using the Baseline model for both the inviscid and viscous calculations of equilibrium boundary layers are most encouraging. The inviscid results indicate that the Baseline model performs at least as well as any of the other models and usually better. The viscous computations show that the model equations can easily and successfully be integrated through the viscous sublayer and that they yield solutions that correspond well with data for flows with adverse, zero, and favorable pressure gradients and for flows with blowing. Since the Baseline model has these capabilities, it can be regarded as a reliable foundation for analyzing flows with streamline curvature and coordinate system rotation.

3. BOUNDARY LAYERS ON CURVED SURFACES

We now turn our attention to effects of streamline curvature and system notation on turbulent boundary layers. As stated in Subsection 2.3.4, the Baseline model in its original form does not accurately predict the effects of streamline curvature. However with the addition of a straightforward curvature correction term, the Baseline model can successfully be applied to flows with curved streamlines. This section gives a brief overview of the development of the correction term and tests it for boundary layers with curved streamlines and for rotating channel flow. Both compressible and incompressible flows are considered.

3.1 STREAMLINE CURVATURE/SYSTEM-ROTATION MODIFICATIONS

With an understanding of some of the physics of flow over curved walls and the proper interpretation of the turbulence quantity, e, a straightforward curvature correction can be derived. This is explained in detail by Wilcox and Chambers.[1] Hence only a brief description will be presented here.

Three points are essential to the argument. The first important point is that the mixing energy is directly proportional to $\langle v'^2 \rangle$ (the component of the fluctuating velocity normal to the surface); ω is the rate at which $\langle v'^2 \rangle$ kinetic energy is converted to other modes of energy (e.g., mean kinetic energy, thermal energy, other fluctuation modes). The second key point is that the equation for e should be regarded as the $\langle v'^2 \rangle$ component of the full Reynolds stress equations. The final key observation is that if the tensor transformation properties of the $\langle v'^2 \rangle$ equation are endowed upon the equation for e, straightforward curvature (and system rotation) correction terms can be added which account for altered turbulence structure.

Implementing Point 3 proceeds as follows. In a curved-streamline coordinate system with local radius of curvature, R, the equation for the instantaneous vertical velocity, v, has a Coriolis acceleration term, viz,

$$\frac{\partial v}{\partial t} + \underline{u}\cdot\nabla v - \frac{u^2}{R} = -\frac{1}{\rho}\frac{\partial p}{\partial y} + \text{diffusion} \qquad (81)$$

Hence, multiplying Equation 81 by v' and time averaging, we obtain

$$\frac{\partial \langle v'^2/2\rangle}{\partial t} + \bar{\underline{u}}\cdot\nabla\langle v'^2/2\rangle - \frac{\bar{u}}{R}\langle u'v'\rangle = \text{other terms} \qquad (82)$$

where, for simplicity, $\bar{\underline{u}}$ denotes mean value. Then, defining $e \equiv 9/4\langle v'^2\rangle$ and approximating $\langle -u'v'\rangle \doteq \frac{e}{\omega}\frac{\partial u}{\partial y}$, Equation 82 becomes (with overhead bars dropped for convenience)

$$\frac{\partial e}{\partial t} + \underline{u}\cdot\nabla e = -\frac{9}{2}\frac{u}{R}\frac{e}{\omega}\frac{\partial u}{\partial y} + \text{other terms} \qquad (83)$$

The term multiplied by 9/2 is the curvature correction term.† Similarly, for flow in a coordinate frame rotating with angular velocity Ω, we obtain

$$\frac{\partial e}{\partial t} + \underline{u}\cdot\nabla e = 9\Omega\frac{e}{\omega}\frac{\partial u}{\partial y} + \text{other terms} \qquad (84)$$

The e and ω equations used for the boundary layer flows with curved streamlines and for rotating channel flow are hence assumed to be:

† Note that the correction term was incorrectly written by Wilcox and Chambers[1] as being proportional to 9.

Boundary Layers with Curved Streamlines

Turbulent Mixing Energy

$$u\frac{\partial e}{\partial x} + v\frac{\partial e}{\partial y} = [\alpha^*\left|\frac{\partial u}{\partial y} - \frac{u}{R}\right| - \beta^*\omega]e + \frac{\partial}{\partial y}[(\nu+\sigma^*\frac{e}{\omega})\frac{\partial e}{\partial y}] - \frac{9}{2}\frac{u}{R}\frac{e}{\omega}\frac{\partial u}{\partial y} \quad (85)$$

Dissipation Rate

$$u\frac{\partial \omega^2}{\partial x} + v\frac{\partial \omega^2}{\partial y} = [\alpha\left|\frac{\partial u}{\partial y} - \frac{u}{R}\right| - (\beta + 2\sigma(\frac{\partial \ell}{\partial y})^2)\omega]\omega^2 + \frac{\partial}{\partial y}[(\nu+\sigma\frac{e}{\omega})\frac{\partial \omega^2}{\partial y}] \quad (86)$$

Rotating Channel Flow

Turbulent Mixing Energy

$$\frac{d}{dy}[(\nu+\sigma^*\frac{e}{\omega})\frac{de}{dy}] + (\alpha^*\left|\frac{du}{dy}\right| - \beta^*\omega)e + 9\,\Omega\,\frac{e}{\omega}\frac{du}{dy} = 0 \quad (87)$$

Dissipation Rate

$$\frac{d}{dy}[(\nu+\sigma\frac{e}{\omega})\frac{d\omega^2}{dy}] + [\alpha\left|\frac{du}{dy}\right| - (\beta+2\sigma(\frac{d\ell}{dy})^2)\omega]\omega^2 = 0 \quad (88)$$

3.2 INCOMPRESSIBLE APPLICATIONS

The Baseline model with the curvature correction term was first applied to several incompressible flows (Table 3).

Table 3. Incompressible Viscous Calculations for Boundary Layers with Curvature

FLOW	DATA SOURCE
• Low Reynolds number turbulent flow past a cylinder	Patel[19] data.
• Constant pressure flow over a convex wall	So-Mellor[15] data; Meroney[16] correlation.
• Separating flow over a convex wall	So-Mellor[15] data.
• Rotating channel flow	Johnston[20] data.

The most difficult test of all the incompressible cases considered is low Reynolds number turbulent flow past a cylinder. In addition to having streamline curvature and adverse pressure gradient, the flow is dominated by viscous phenomena. Results of the computation are shown in Figures 28-30. All computed quantitites are in close agreement with the experimental data of Patel.[19] Computed and measured velocity profiles are compared in Figure 28. The largest discrepancies are less than 10% throughout the flow. Even the predicted and measured separation points are reasonably close; the computed separation occurs at circumferential angle $\phi=101°$ while separation was observed to occur at $\phi=110°$. As shown in Figures 29 and 30, computed shape factor and momentum-thickness Reynolds number differ from corresponding measured values by no more than 6%, even as the flow nears separation.

Figures 31-33 exhibit computed and measured flow properties for flow over a convex wall with constant pressure and with adverse pressure gradient. Figure 31 shows that computed and measured skin friction are within a few percent. In the separating flow, separation was observed between 5.50 and 5.83 feet (1.68 and 1.78 m) downstream of the leading edge, while the computation indicates separation will occur a little farther downstream. As seen from Figure 32, predicted shape factors show somewhat larger discrepancies from the measured values; the largest discrepancy is 12%. Finally, Figure 33 shows that computed and measured velocity profiles differ by no more than 6%.

The final incompressible application is to rotating channel flow (Figures 34-36). Figures 34 and 35 show the contrast between nonrotating and rotating channel velocity profiles. Figure 36 presents the ratio of the rotating friction velocity, u_τ, to the nonrotating friction velocity u_{τ_o}, for a range of rotation numbers. The predictions are generally within 10% of corresponding measurements.

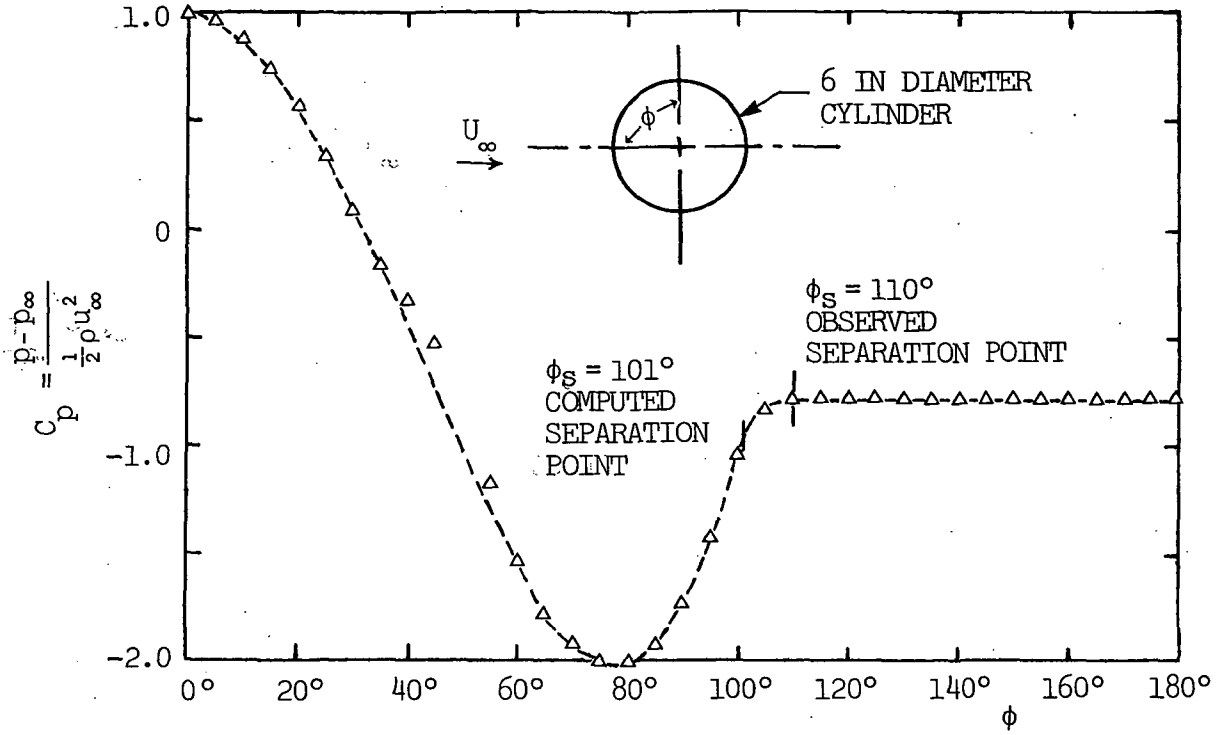

Experimental arrangement of cylinder and measured pressure distribution.

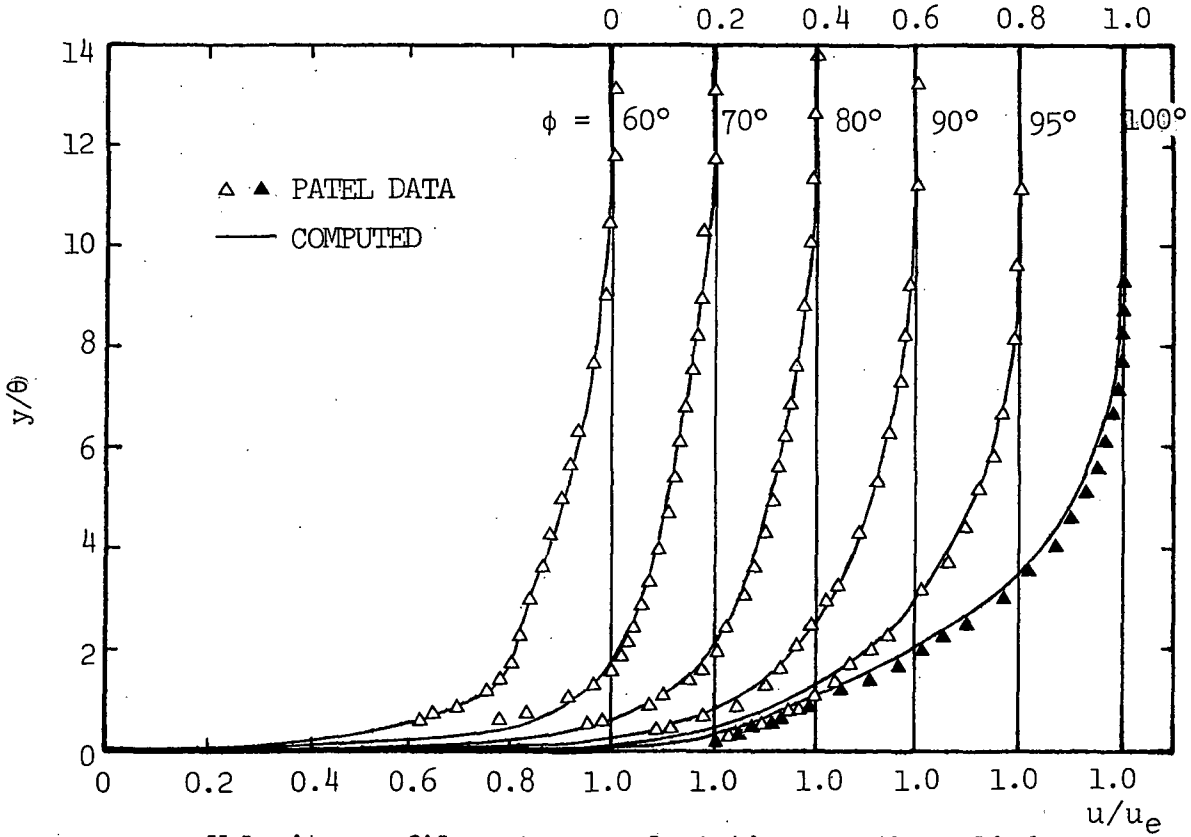

Velocity profiles at several stations on the cylinder.

Figure 28. Comparison of computed and measured flow properties for Patel's low-Reynolds-number turbulent flow past a cylinder; $Re_D = 5.01 \cdot 10^5$.

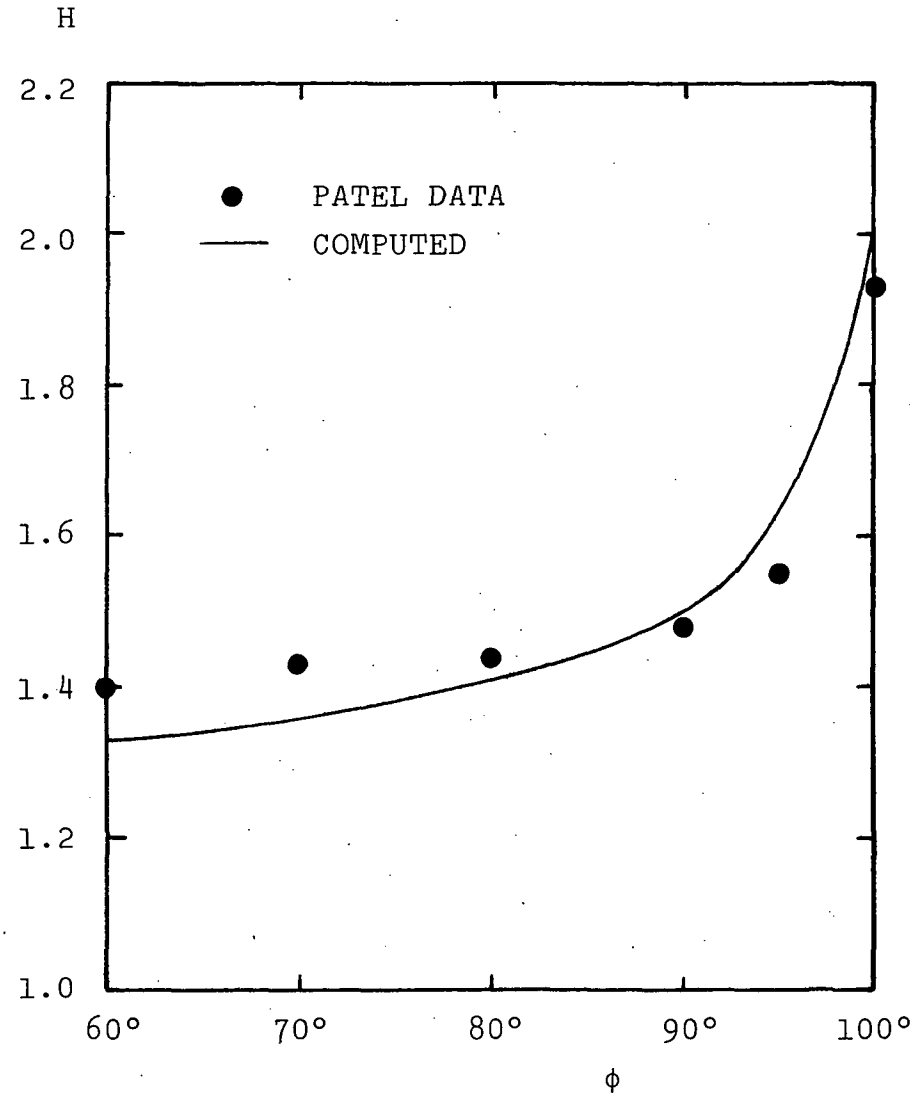

Figure 29. Comparison of computed and measured shape factor for Patel's low-Reynolds-number turbulent flow past a cylinder; $Re_D = 5.01 \cdot 10^5$.

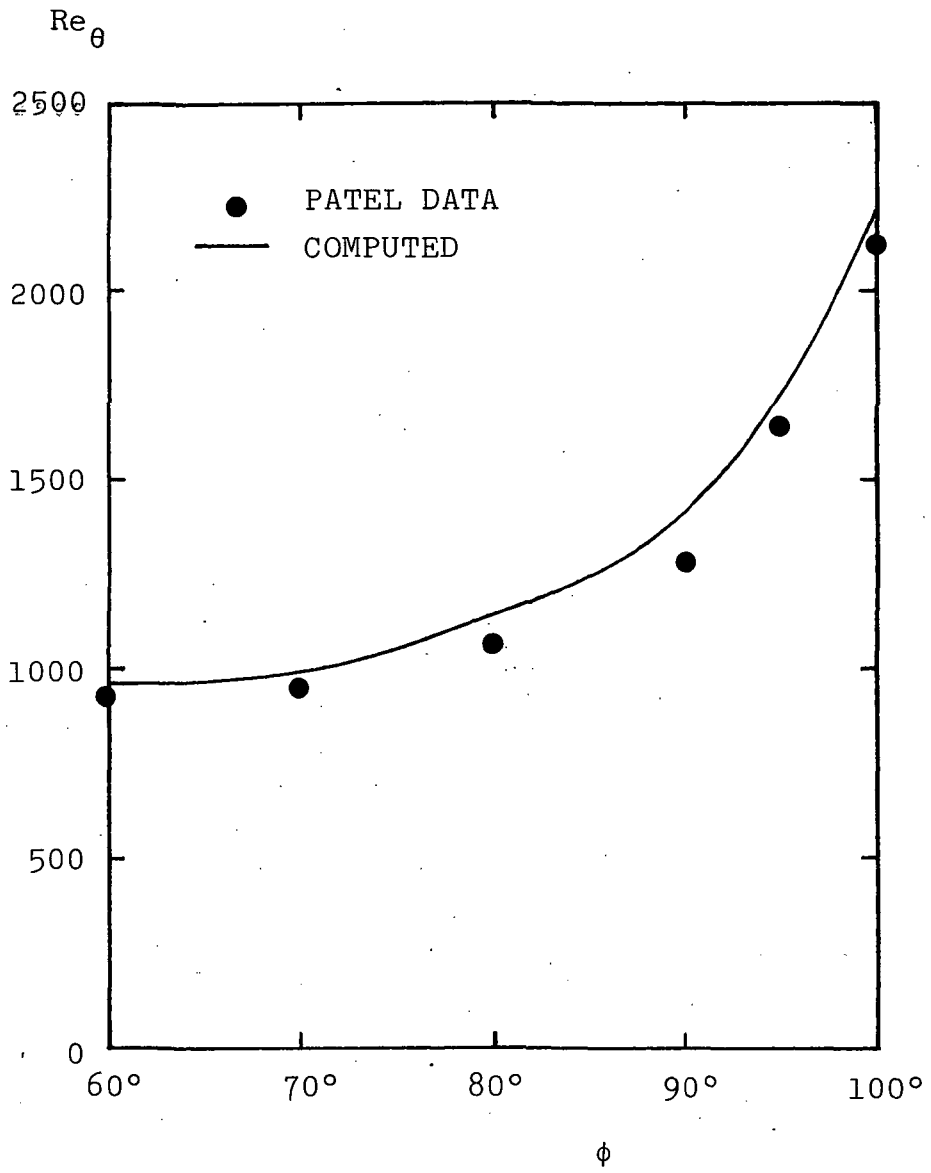

Figure 30. Comparison of computed and measured momentum-thickness Reynolds number for Patel's low-Reynolds-number turbulent flow past a cylinder; $Re_D = 5.01 \cdot 10^5$.

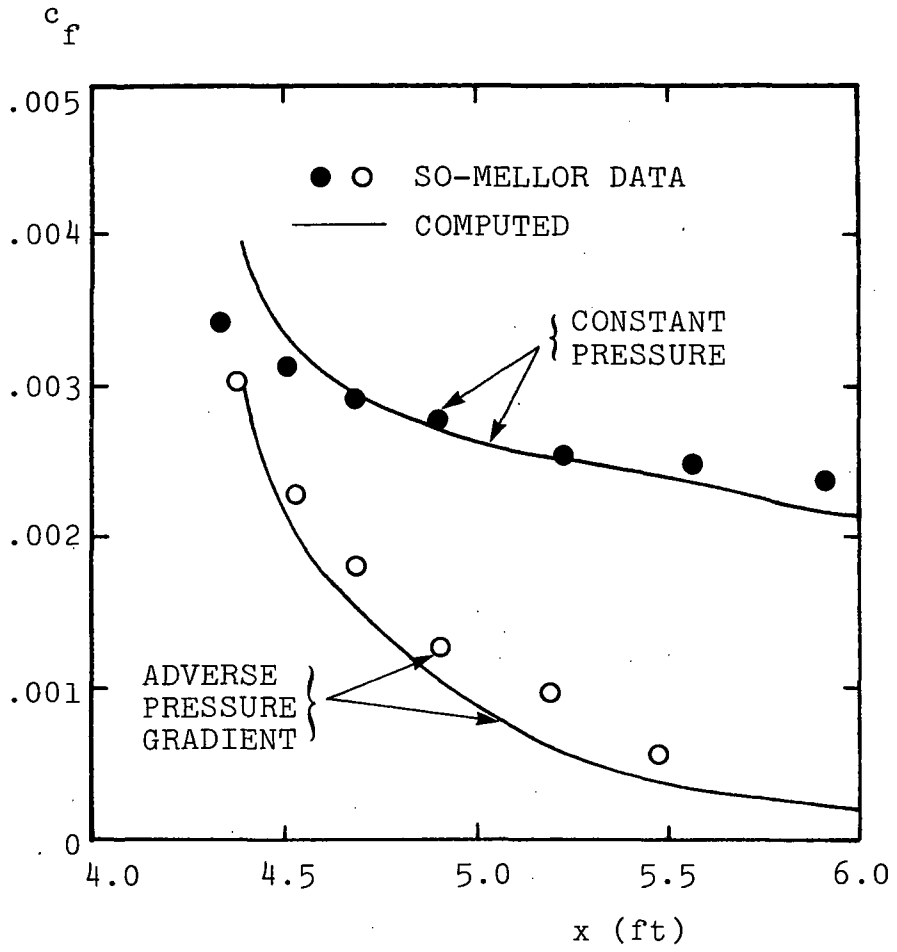

Figure 31. Comparison of computed and measured skin friction for flow over a convex surface.

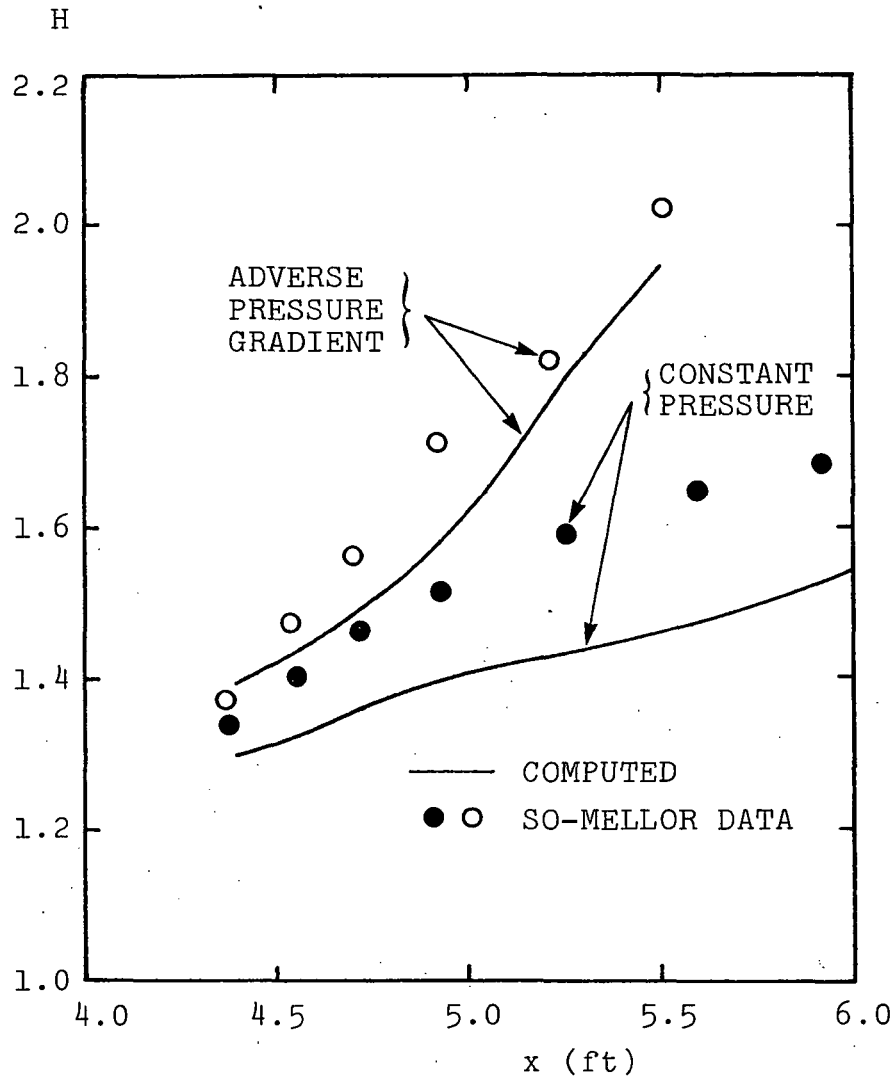

Figure 32. Comparison of computed and measured shape factor for flow over a convex surface.

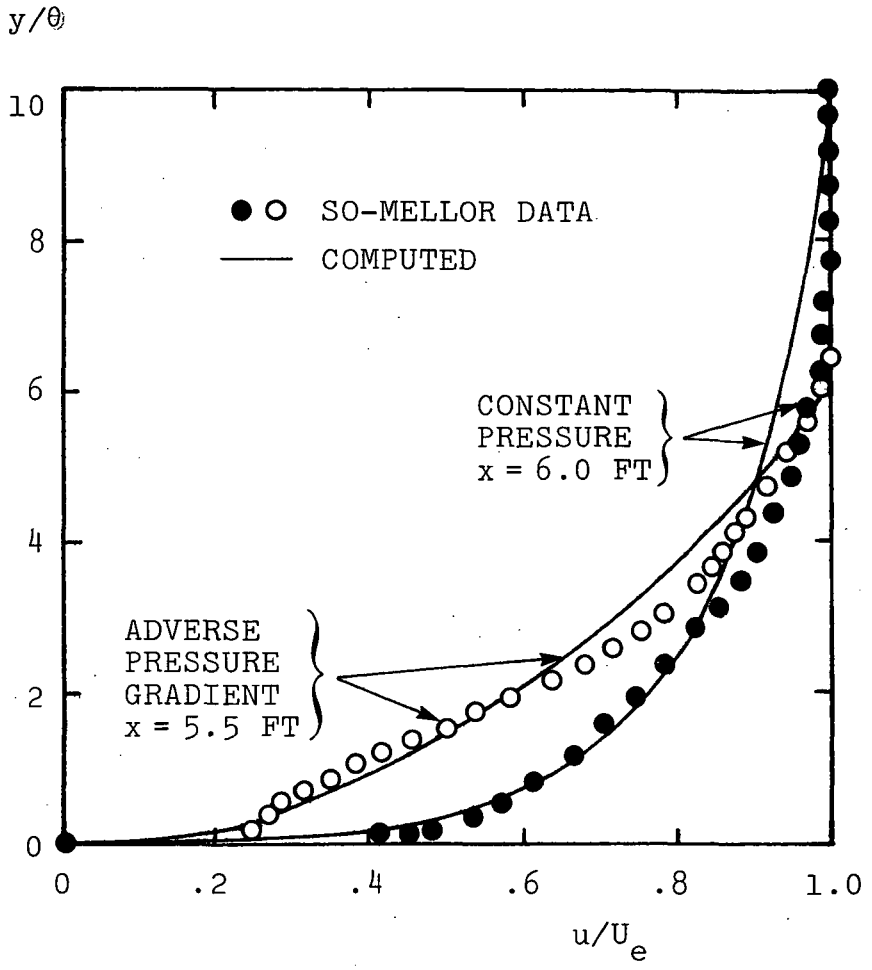

Figure 33. Comparison of computed and measured velocity profiles for flow over a convex surface.

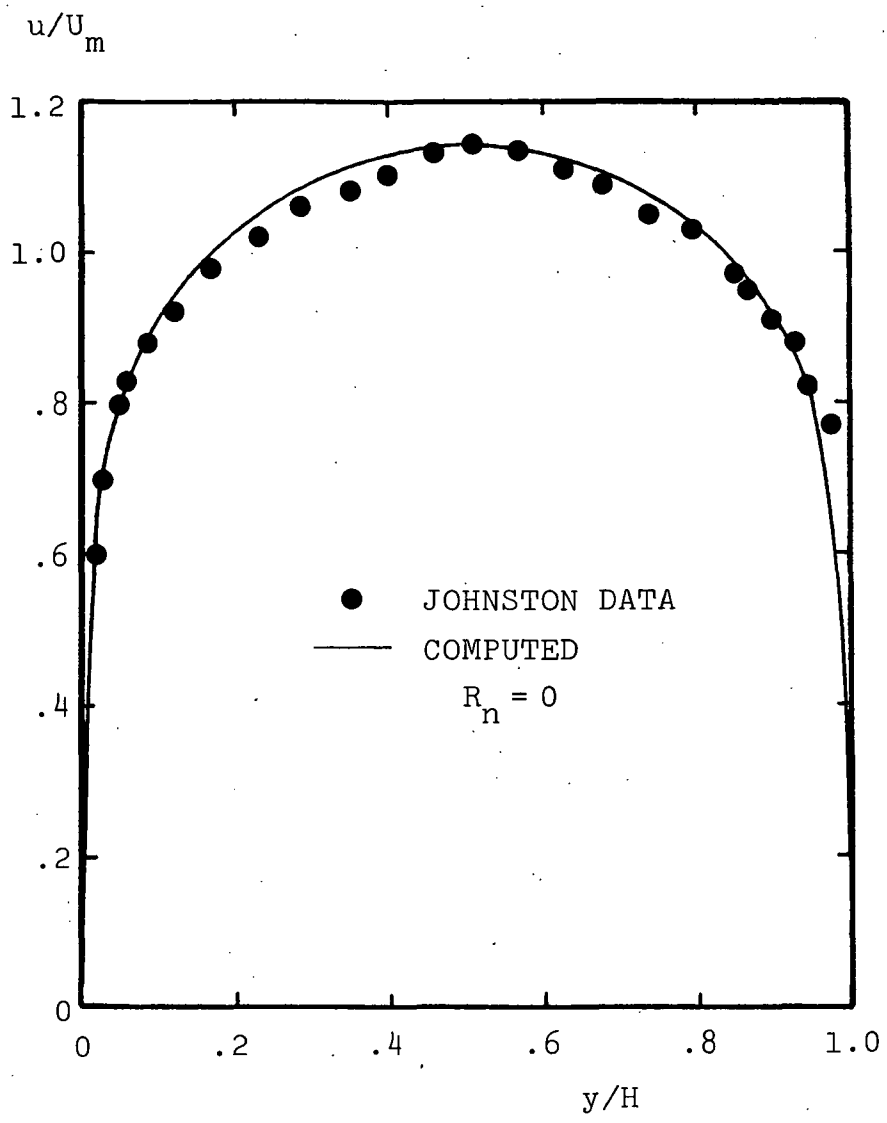

Figure 34. Comparison between computed and measured flow properties for non-rotating channel flow. $R_n = \Omega H/U_m$ where U_m is the average flow velocity.

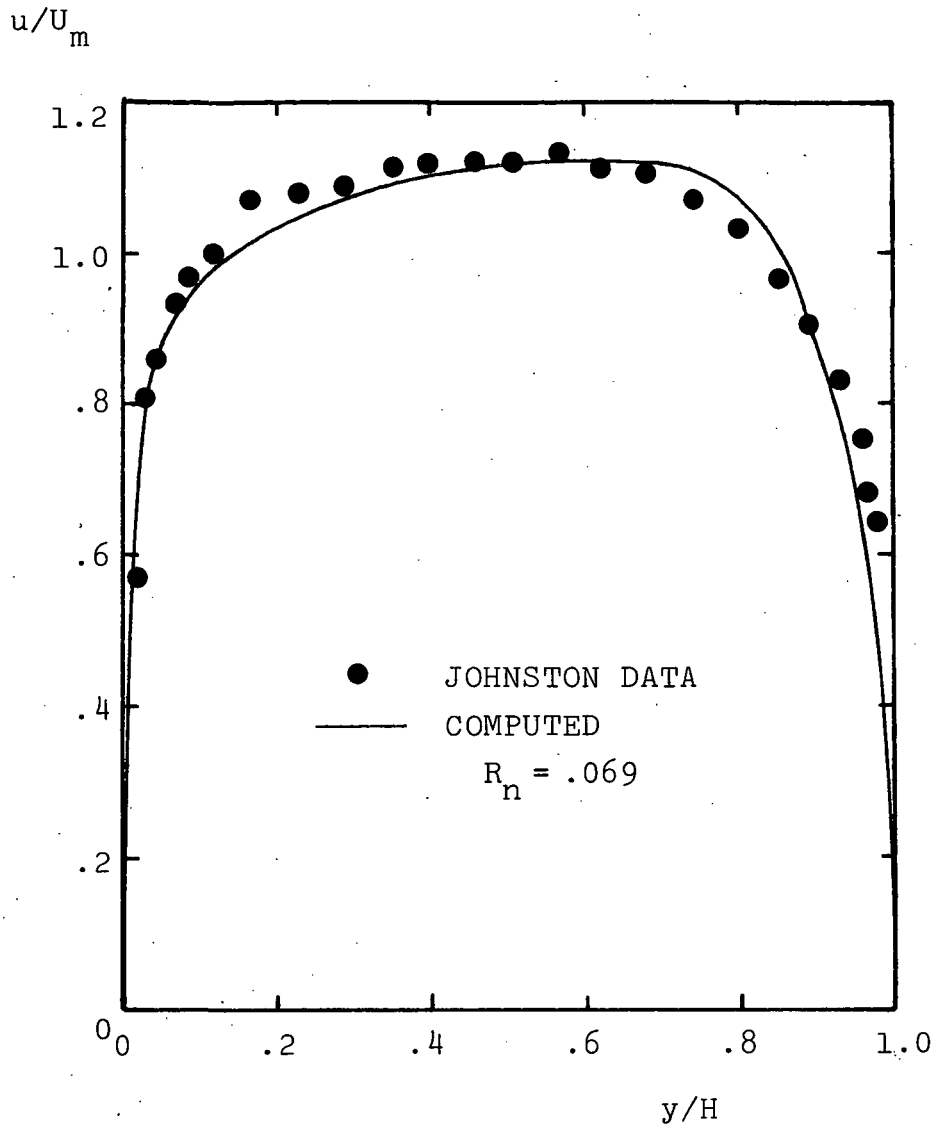

Figure 35. Comparison between computed and measured flow properties for rotating channel flow. $R_n = \Omega H/U_m$ where U_m is the average flow velocity.

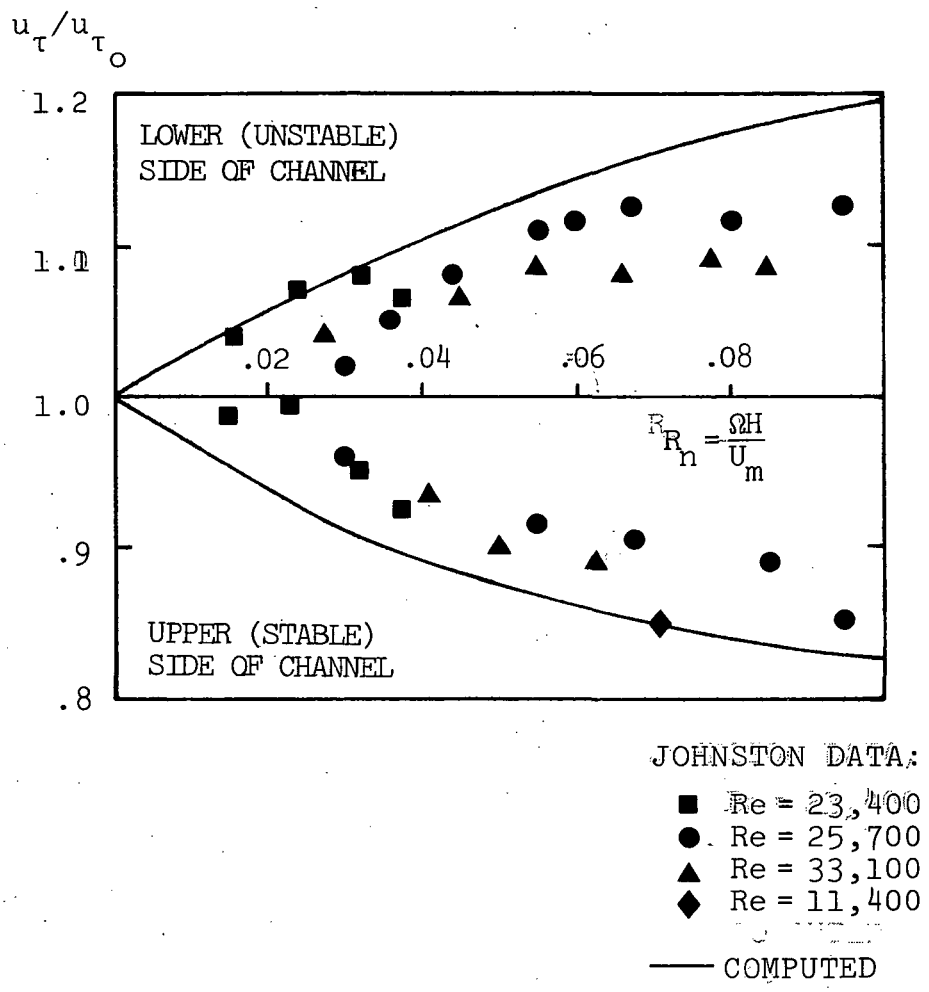

Figure 36. Comparison of computed and experimentally measured values of u_τ/u_{τ_o} as a function of the rotation number, $\Omega H/U_m$ for rotating channel flow; Ω = rotation speed, H = channel width, U_m = average velocity, Re = Reynolds number based on the average velocity.

3.3 COMPRESSIBLE APPLICATIONS

As a final test of the theory, the Baseline model was applied to two compressible flows (Table 4). Following Wilcox and

Table 4. Compressible Viscous Calculations with Streamline Curvature

FLOW	DATA SOURCE
• Mach 2.5 flow with heat transfer over a convex wall	Thomann[22] data.
• Mach 3.5 nearly adiabatic flow over a concave wall	Sturek-Danberg[23] data.

Alber,[21] we introduce the specific turbulent dissipation rate, Ω, so that the boundary layer form of the compressible model equations with the curvature modification are as follows.

Specific Turbulent Mixing Energy

$$\rho u \frac{\partial e}{\partial x} + \rho v \frac{\partial e}{\partial y} = [\alpha^* \left| \frac{\partial u}{\partial y} - \frac{u}{R} \right| - \beta^* \rho \Omega] \rho e + \frac{\partial}{\partial y}[(\mu + \sigma^* \frac{e}{\Omega}) \frac{\partial e}{\partial y}] - \frac{9}{2} \frac{e}{\Omega} \frac{u}{R} \frac{\partial u}{\partial y} \quad (89)$$

Specific Turbulent Dissipation Rate

$$\rho u \frac{\partial \Omega^2}{\partial x} + \rho v \frac{\partial \Omega^2}{\partial y} = \left\{ \alpha \left| \frac{\partial u}{\partial y} - \frac{u}{R} \right| - [\beta + 2\sigma (\frac{\partial \ell}{\partial y})^2] \rho \Omega \right\} \rho \Omega^2 + \frac{\partial}{\partial y}[(\mu + \sigma \frac{e}{\Omega}) \frac{\partial \Omega^2}{\partial y}] \quad (90)$$

The quantities ρ and μ denote density and molecular viscosity (given by Sutherland's law), respectively.

The Baseline model was first applied to the Thomann flow using a wall boundary condition on Ω that simulates a smooth wall (the case of actual interest). As a generalization of the

incompressible boundary condition (Equation 77), the wall value of the dissipation rate is given by

$$\Omega_w = \frac{S \dot{u}_\tau^2}{\alpha^* \mu_w} \tag{91}$$

where S is the universal function defined in Equations 78-80 and μ_w is the molecular viscosity at the wall. Using a value of S corresponding to a smooth wall (S of the order of 10^4) gave skin friction that was below the Hopkins-Inouye compressible skin friction correlation by about 20%. Also, for this value of S, the Stanton number, S_t, was as much as 18% too low (Figure 37). However, it was found that by simulating a rough wall (S on the order of 10), good skin friction and Stanton number distributions for the equilibrium portion of the boundary layer were obtained as shown in Figures 37 and 38.

The necessity of simulating flow over a rough wall is not as yet understood and is an area for future research. However, by at least assuring good equilibrium solutions, it was possible to examine how the model behaves when the boundary layer is disturbed by curvature and/or pressure gradient.

In the region where curvature begins, consistent with measurements, the model predicts a 10% reduction in Stanton number (relative to the plane-wall value). However, the model fails to predict the observed rapid decrease in S_t beyond x=1.25 ft (.38 m). The discrepancy may be due to the fact that curvature affects the heat transfer differently from the way it affects skin friction.

The Sturek-Danberg calculation proceeded as did the Thomann case. The appropriate large value of S resulted in skin friction as much as 19% lower than the Hopkins-Inouye skin friction

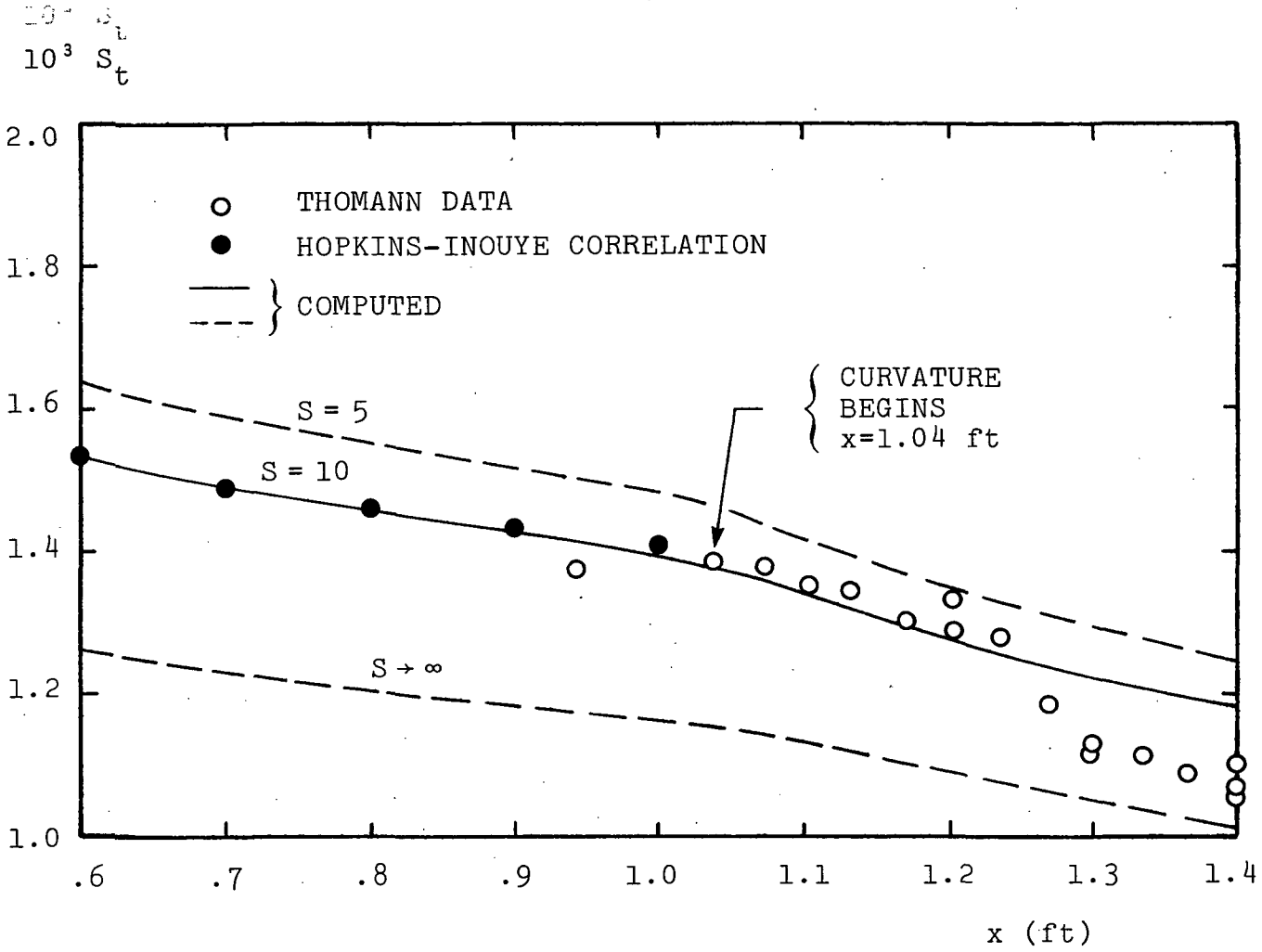

Figure 37. Comparison of computed and measured Stanton number for Mach 2.5 flow over a convex surface.

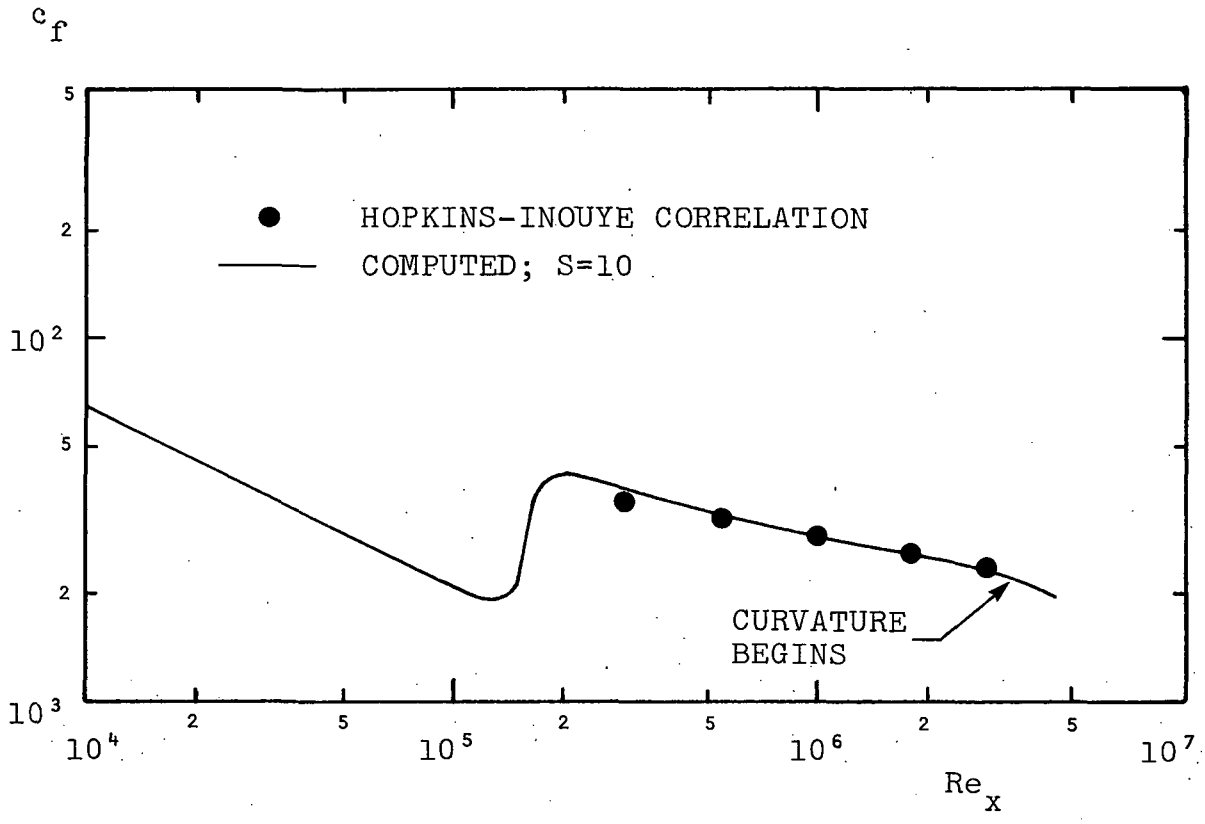

Figure 38. Comparison of computed skin friction with the Hopkins-Inouye correlation for Mach 2.5 flow over a convex surface.

correlation (Figure 39). Hence, as in the Thomann case, the computation was performed with S=10. As shown in Figure 39, the predicted c_f is very close to the Hopkins-Inouye value, yet is considerably higher than the measured values in the equilibrium portion of the flow. However, the data are suspect in this region since even Sturek and Danberg note that their measuring techniques were only accurate to within 15%.

The predicted overall decrease in surface shear stress is consistent with the measurements although differences of about 20% of scale are present. The discrepancies in the curved region of the flow may also be caused by the inaccuracies in the measurements so that this case does not provide a definitive test of the theory.

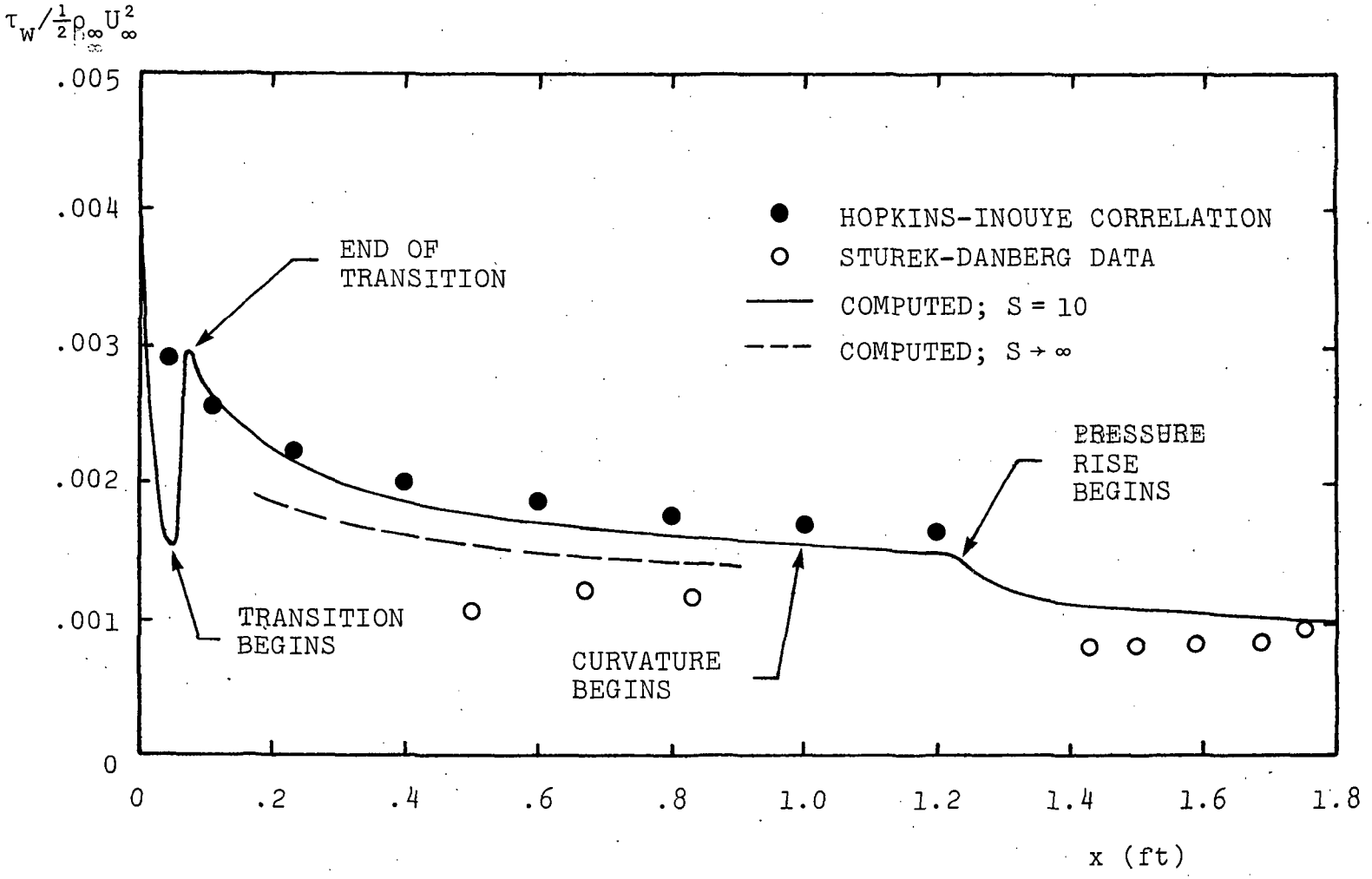

Figure 39. Comparison of computed and measured skin friction for Mach 3.5 flow over a concave surface.

4. DISCUSSION

Perhaps the most important conclusion that can be drawn is that the Baseline model is at a state of development where it can be used for general engineering applications. In particular, results of the viscous equilibrium-boundary-layer computations in Section 2 show that the Baseline model is as accurate as mixing-length theory where mixing-length theory is expected to apply. Furthermore, because of the model's generality and more-solid physical foundation, its range of applicability extends far beyond that of mixing-length theory's. The model's range of applicability includes flows with curved streamlines and coordinate system rotation. Using the Baseline model, excellent quantitative agreement between theory and experiment has been obtained for effects of curvature and rotation on incompressible boundary layers. Although more work remains to be done for compressible boundary layer applications, results for the two supersonic flows considered in Section 3 are also encouraging.

Consistent with the project objective, the path is now cleared for proceeding to analysis of streamline-curvature and system-rotation effects on turbulent boundary layers. Presumably, RSE model deficiencies can now be eliminated by changes analogous to those made to the Saffman model which resulted in the Baseline model. Such changes should be made. Work with the Baseline model should continue as well. That is, parallel development of the RSE and Baseline models appears to hold the most promise for yielding useful, accurate engineering tools for predicting curvature/rotation effects.

APPENDIX

As noted in the introduction, numerical solutions with the RSE model were generated in this study. The model was applied to Bissonnette and Mellor's[24] flow past a segmented cylinder. In the Bissonnette-Mellor experiments, the forebody is stationary and the aft body rotates at a constant angular velocity. The fact that the pressure is not constant in the direction normal to the surface ($\frac{\partial p}{\partial y} \neq 0$) was taken into account in the computations.

The computed mean flow properties and turbulence quantities are shown in Figures A1-A7; experimental data of Bissonnette and Mellor are included for comparison. As shown in Figure A1, predicted streamwise (c_{f_x}) and azimuthal (c_{f_z}) skin-friction coefficients are both about 20% higher than measured. Similarly, the various computed displacement and momentum thicknesses are generally 20% higher than measured (Figures A2 and A3). Figures A4-A7 present velocity and Reynolds stresses on the swirling afterbody. The figures show poor agreement between experimental and computed properties in almost every case. Inspection of the streamwise velocity profile (Figure A4) shows that the worst agreement is in the defect layer of the boundary layer. This is consistent with the results obtained in analyzing Saffman-model-predicted defect layer structure (see Subsection 2.1). That is, examination of Figure A4 shows that the computed streamwise velocity gradient, $\partial u/\partial y$, is much larger than measured in the defect layer. Too strong a gradient results in too much production in the various Reynolds stress equations, and as a result the Reynolds stresses are overestimated. With the exception of $<-u'w'>$, the Reynolds stress components are overpredicted as can be seen in Figures A6 and A7.

The large discrepancies between theory and experiment for the rate of growth of the swirling boundary layer are directly attributable to the excess production of turbulent energy. High turbulent energy levels are synonymous with greater turbulent mixing; because of the overpredicted mixing, the swirling boundary layer grows too quickly and hence the swirling displacement thickness, δ_z^*, and swirling angular momentum thickness, θ_{xz}, are too large.

In summary, results of this computation lend further credence to the claim that the problems plaguing the RSE formulation have the same origin as the deficiencies of the Saffman model.

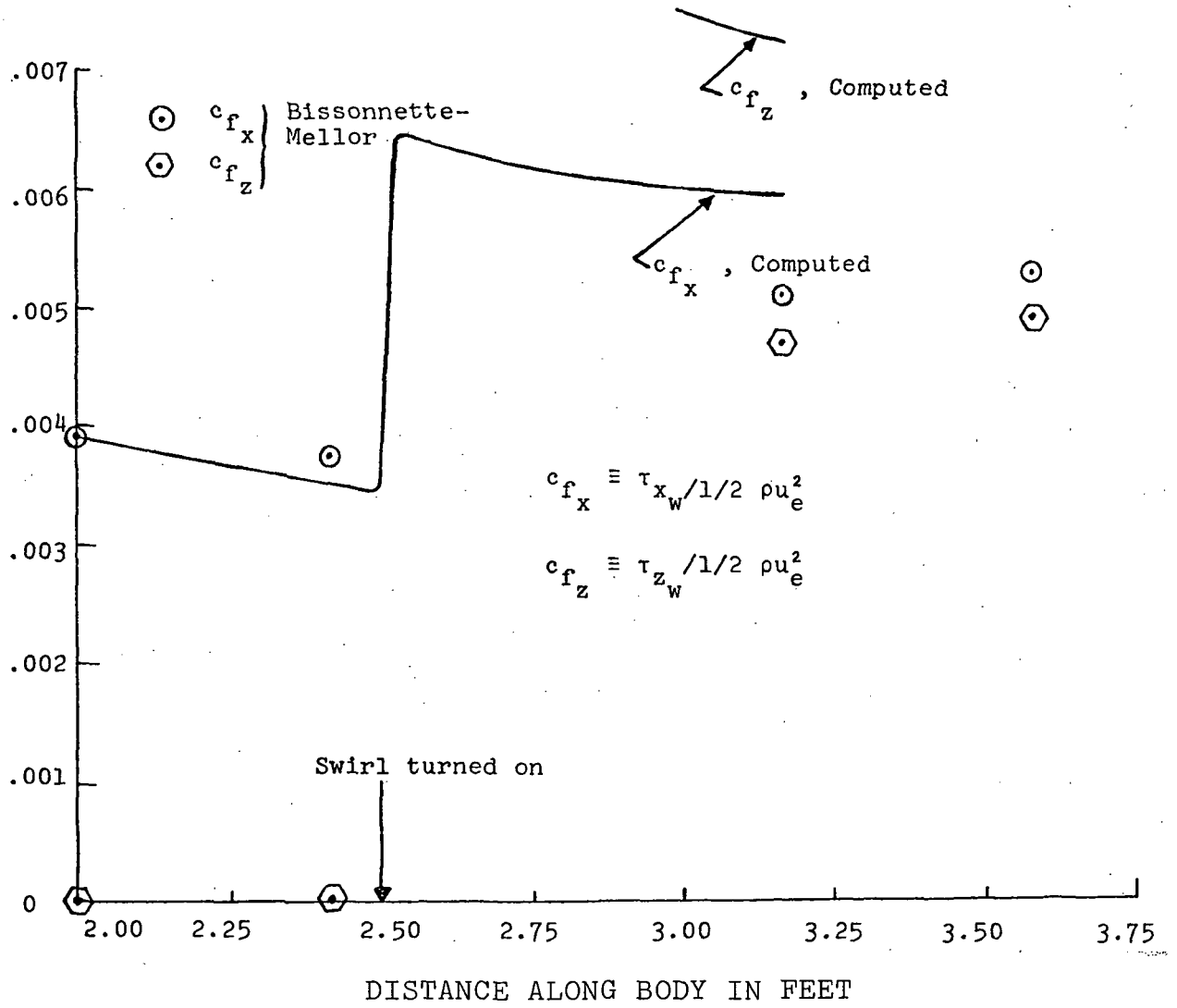

Figure A1. Comparison between computed and measured skin friction coefficients.

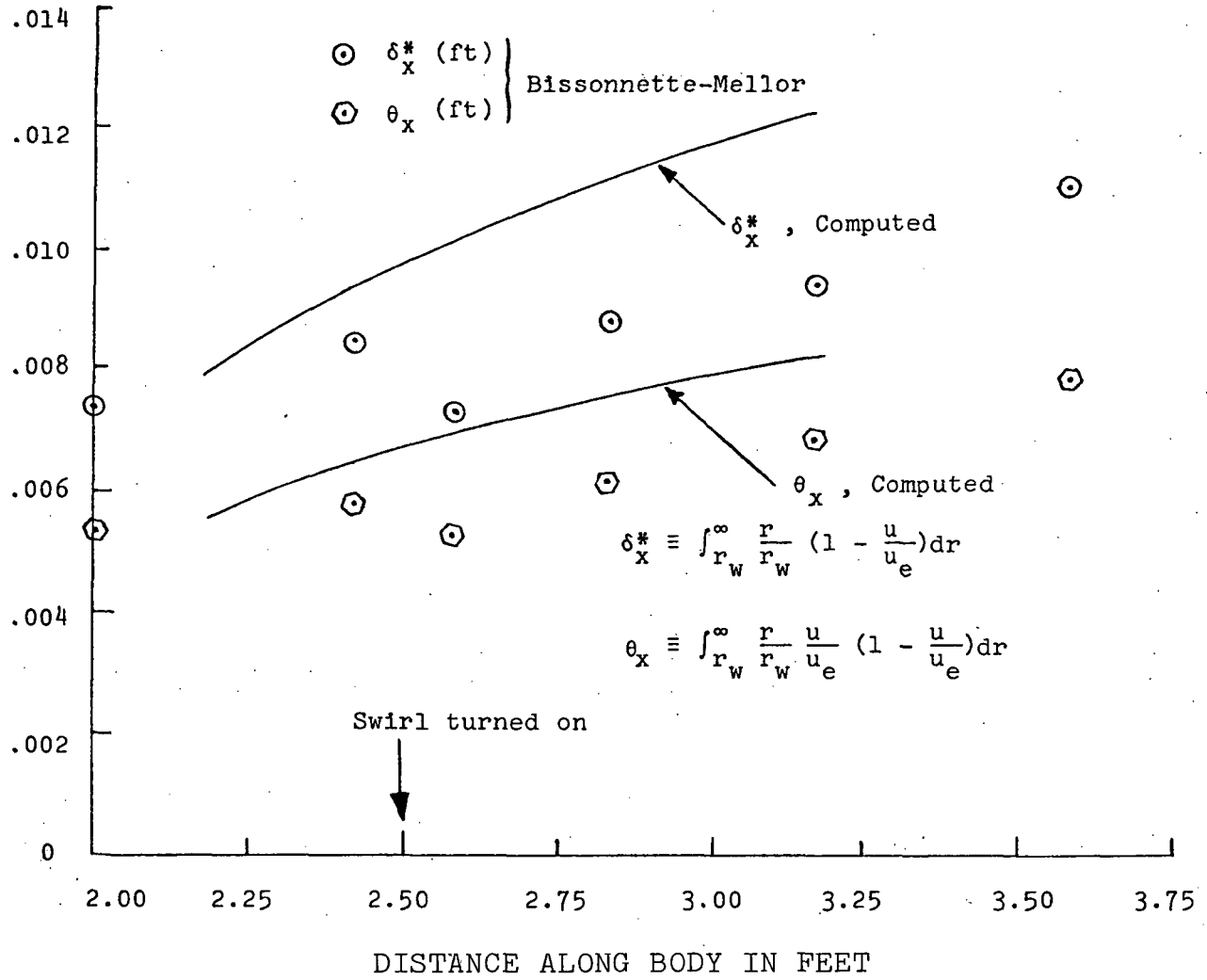

Figure A2. Comparison between computed and measured streamwise-boundary-layer thicknesses.

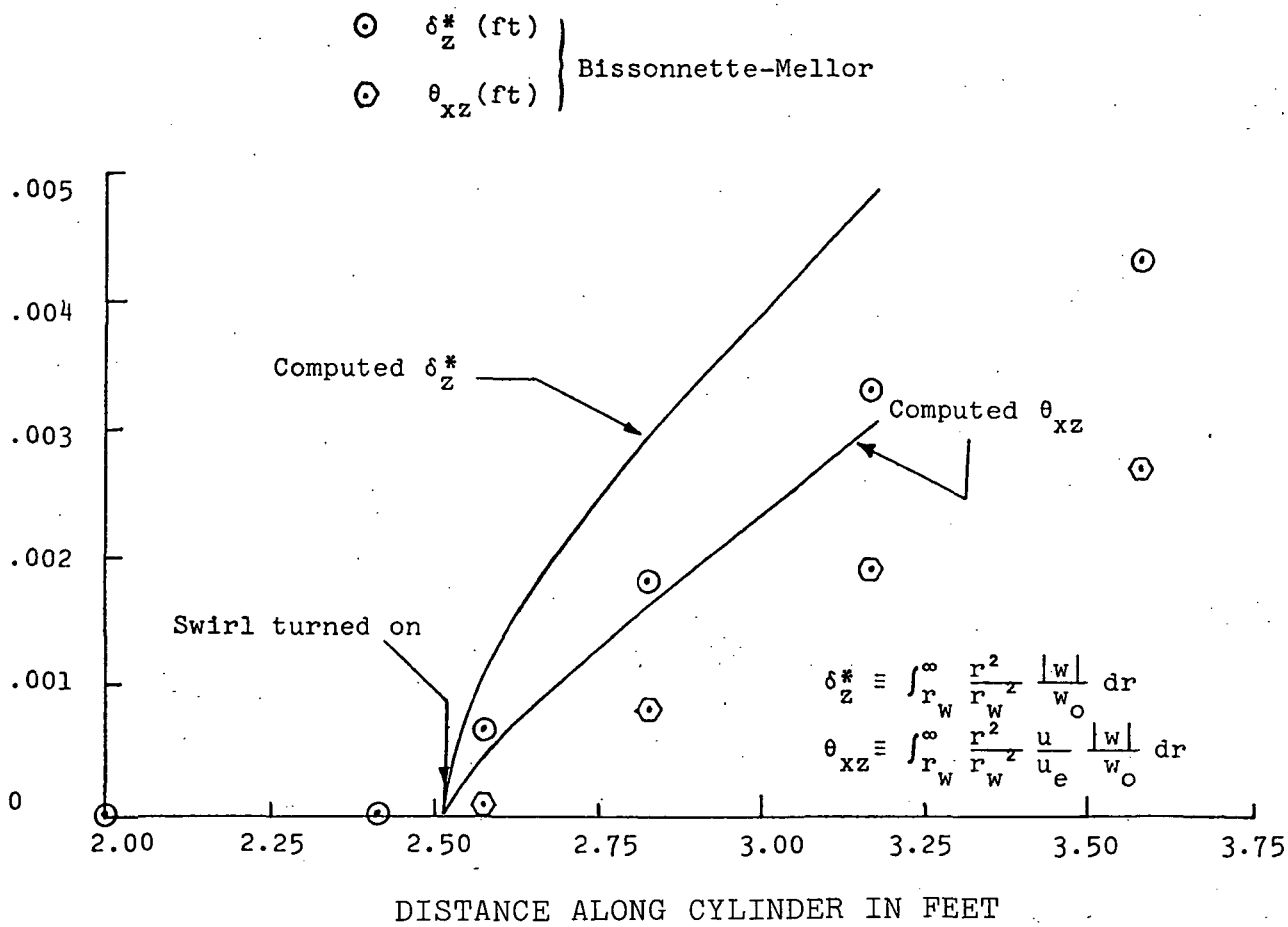

Figure A3. Comparison between computed and measured swirl-boundary-layer thicknesses.

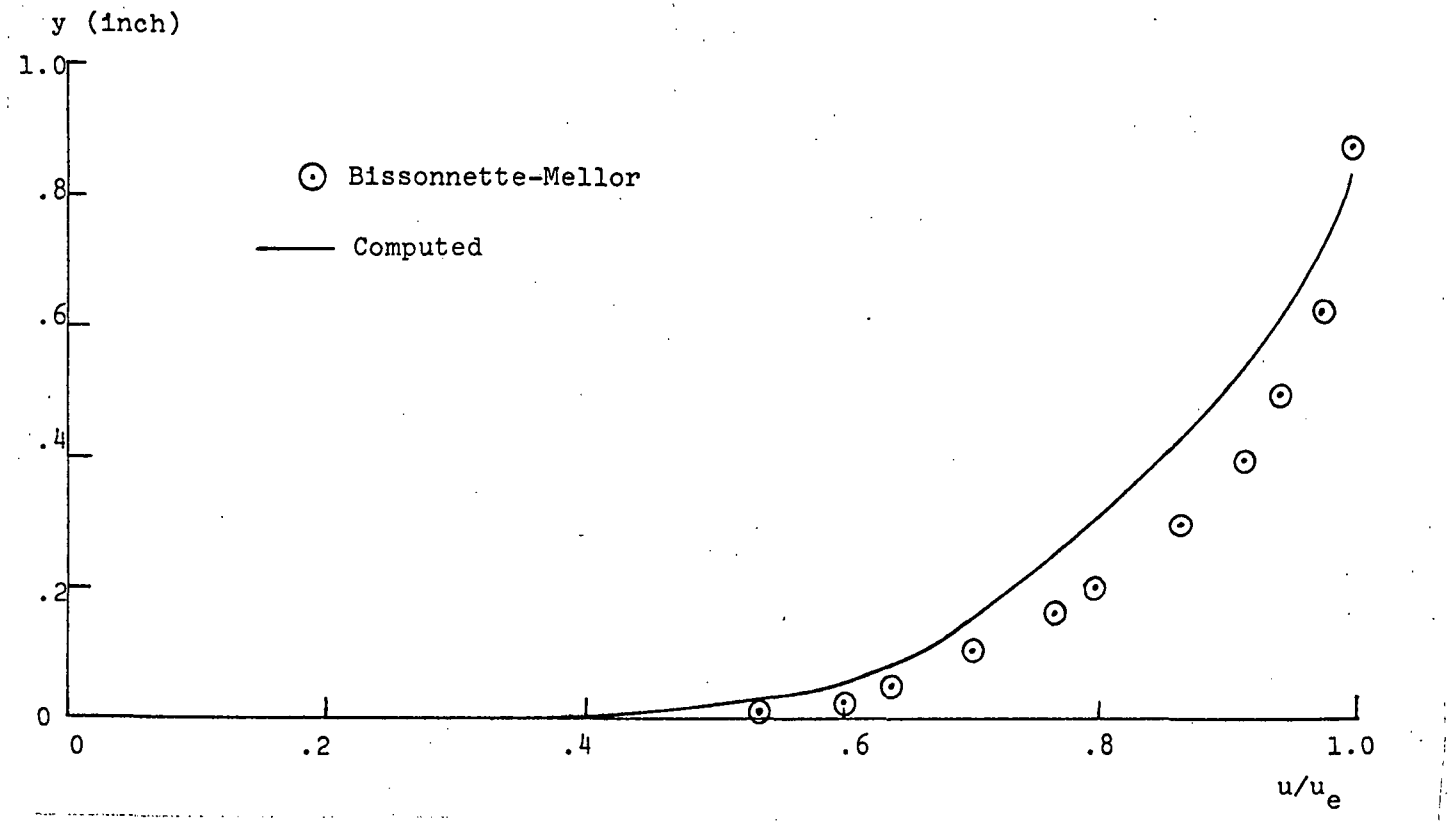

Figure A4. Comparison between computed and measured streamwise velocity profile at x=3.17 ft.

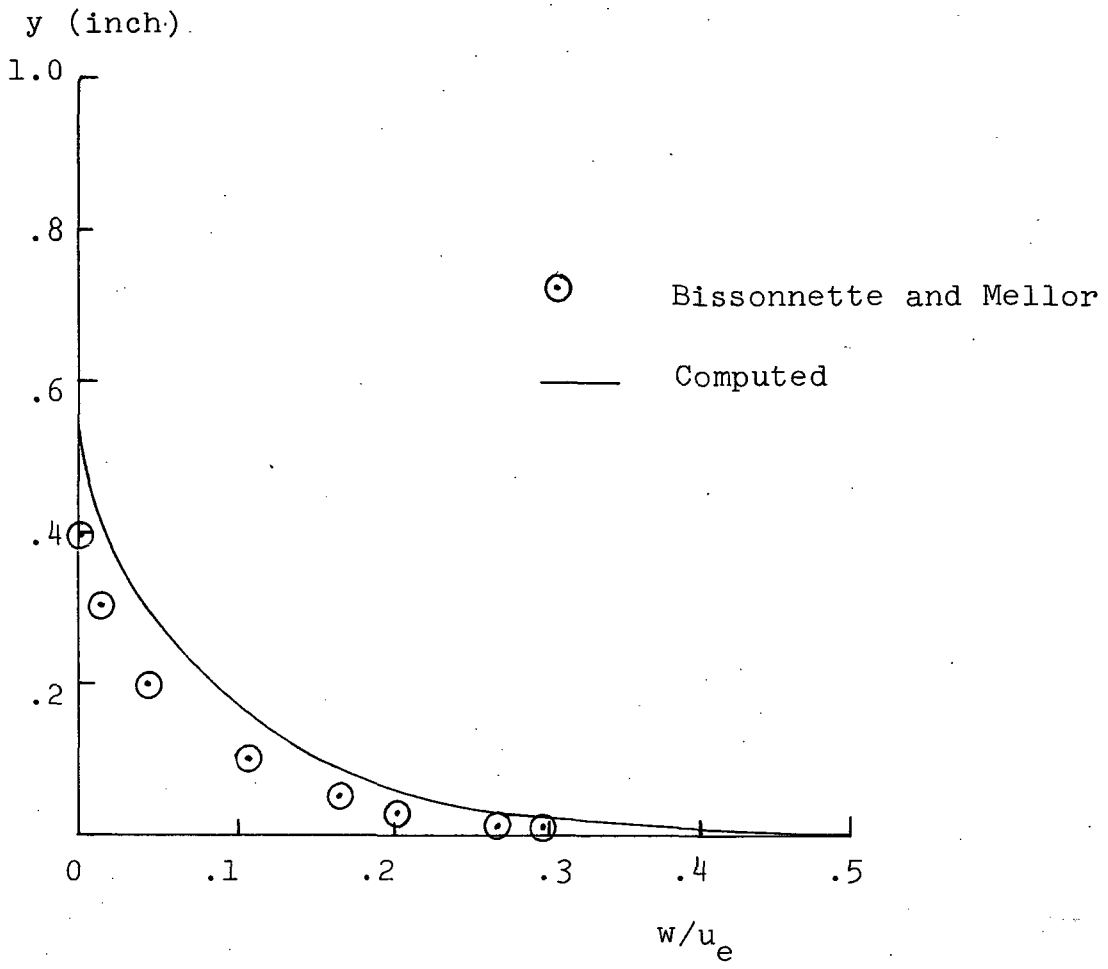

Figure A5. Comparison between computed and measured circumferential velocity profiles at x=3.17 ft.

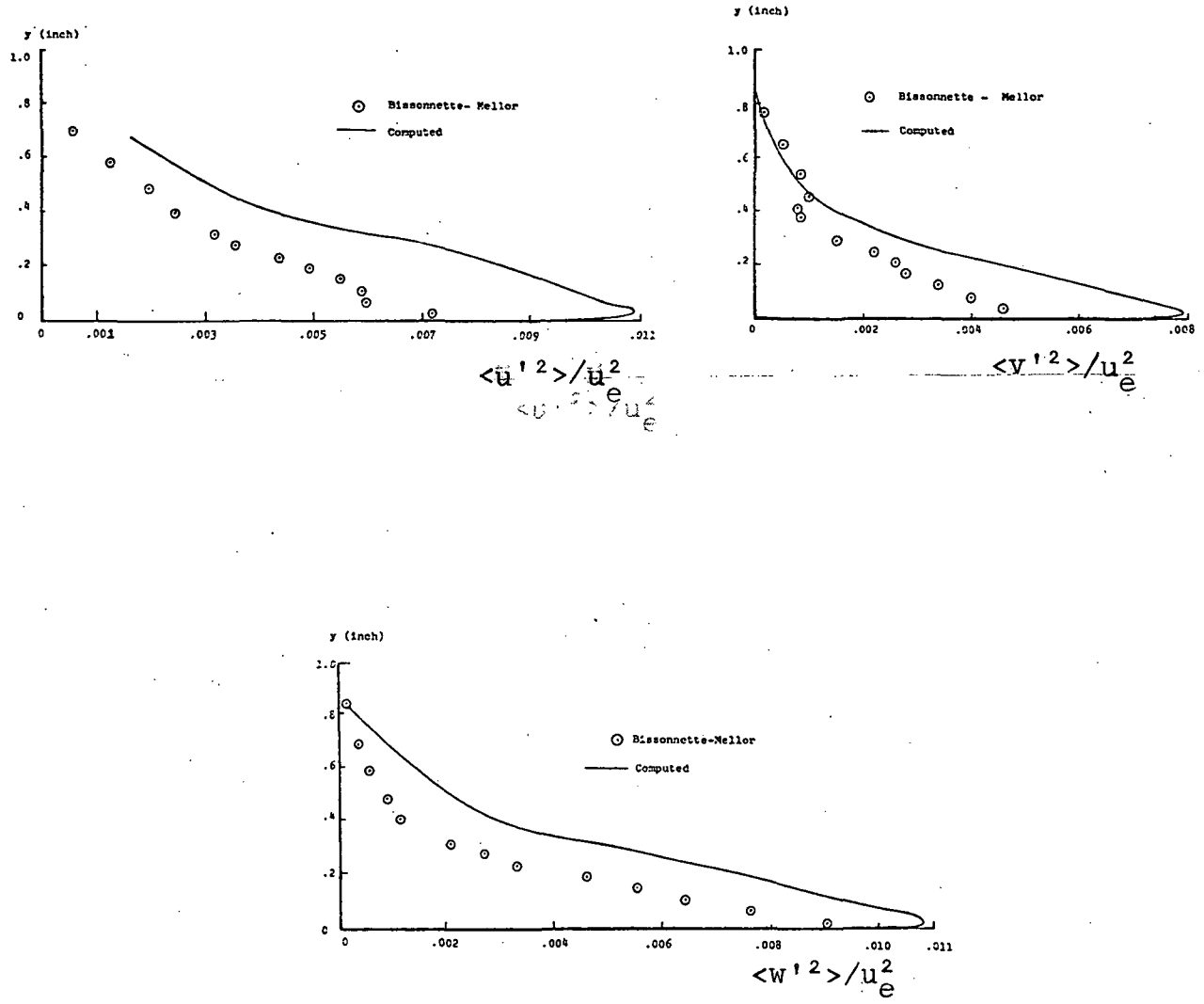

Figure A6. Comparison between computed and measured profiles at x=3.17 ft.

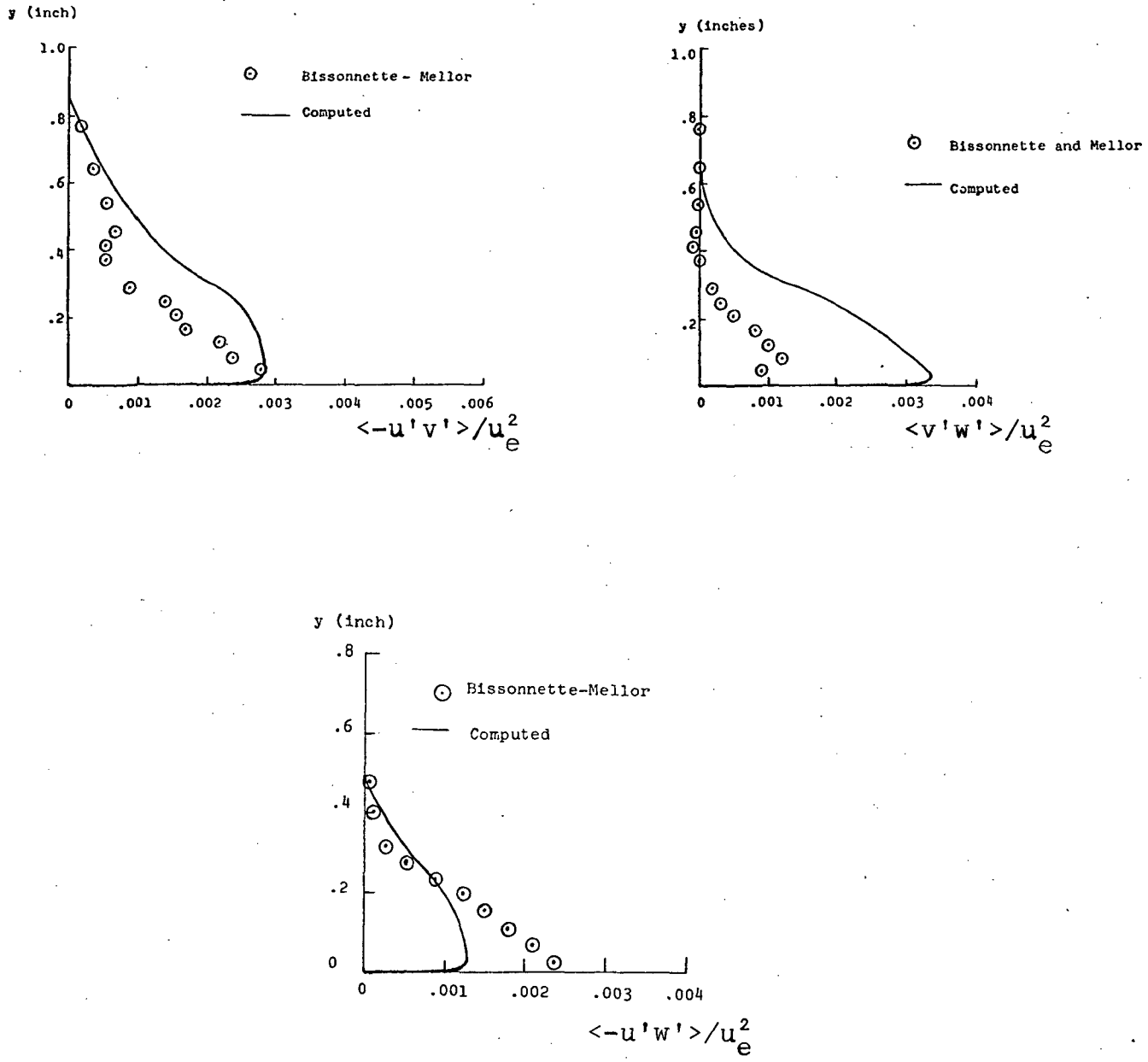

Figure A7. Comparison between computed and measured profiles at x=3.17 feet.

REFERENCES

1. Wilcox, D.C. and Chambers, T.L., "Streamline Curvature Effects on Turbulent Boundary Layers," DCW Industries Report DCW-R-04-01 (February 1975).

2. Saffman, P.G., "A Model for Inhomogeneous Turbulent Flows," Proc Roy Soc Lond A317, pp 417-433 (1970).

3. Bradshaw, P., "The Response of a Constant-Pressure Turbulent Boundary Layer to the Sudden Application of an Adverse Pressure Gradient," ARC R&M 3575 (1969).

4. Andersen, P.S., Kays, W.M., and Moffat, R.J., "The Turbulent Boundary Layer on a Porous Plate: An Experimental Study of the Fluid Mechanics for Adverse Free-Stream Pressure Gradients," Rpt No HMT-15, Dept Mech Engr, Stanford University, CA (1972).

5. Saffman, P.G. and Wilcox, D.C., "Turbulence-Model Predictions for Turbulent Boundary Layers," AIAA Journal, Vol 12, No 4, pp 541-546 (1974).

6. Bush, W.B. and Fendell, F.E., "Asymptotic Analysis of Turbulent Channel and Boundary-Layer Flow," JFM, Vol 56, Part 4, pp 657-681 (1972).

7. Ng, K.H. and Spalding, D.B., "Turbulence Model for Boundary Layers near Walls," Physics of Fluids, Vol 15, No 1, pp 20-30 (1972).

8. Maise, G. and McDonald, H., "Mixing Length and Kinematic Eddy Viscosity in a Compressible Boundary Layer," AIAA Paper 67-199, New York (1967).

9. Jones, W.P. and Launder, B.E., "The Prediction of Laminarization with a Two-Equation Model of Turbulence," Int J of Heat and Mass Trans, Vol 15, pp 301-314 (1972).

10. Klebanoff, P.S., "Characteristics of Turbulence in a Boundary Layer with Zero Pressure Gradient," NACA 1247 (1955).

11. Hopkins, E.J. and Inouye, M., "An Evaluation of Theories for Predicting Turbulent Skin Friction and Heat Transfer on Flat Plates at Supersonic and Hypersonic Mach Numbers," AIAA Journal, Vol 9, No 6, pp 993-1003 (1971).

12. Launder, B.E. and Spalding, D.B., Mathematical Models of Turbulence, Academic Press, London and New York (1972).

13. Mellor, G.L. and Herring, H.J., "A Survey of Mean Turbulent Field Closure Models," AIAA Journal, Vol 11, No 5, pp 590-599 (1973).

14. Coles, D.E. and Hirst, E.A., Proceedings: Computation of Turbulent Boundary Layers - 1968 AFOSR-IFP-Stanford Conference, Vol II, Compiled Data, Dept Mech Engr, Stanford University, California.

15. So, R.M.C. and Mellor, G.L., "An Experimental Investigation of Turbulent Boundary Layers Along Curved Surfaces," NASA CR-1940 (1972).

16. Meroney, R.N., "Turbulent Boundary Layer Growth Over a Longitudinally Curved Surface," AIAA Journal, to be published.

17. Wilcox, D.C. and Traci, R.M., "A Complete Model of Turbulence," Paper to be presented at the AIAA 9th Fluid and Plasma Dynamics Conference, San Diego (July 1976).

18. Traci, R.M., "Turbulence Model Equation Treatment of Boundary Layers with Mass Injection," Paper to be presented at the AIAA 9th Fluid and Plasma Dynamics Conference, San Diego (July 1976).

19. Patel, V.C., "The Effects of Curvature on the Turbulent Boundary Layer," Reports and Memoranda No 3599, Cambridge Engr Dept (1968).

20. Johnston, J.P., Halleen, R.M., and Lezius, D.K., "Effects of Spanwise Rotation on the Structure of Two-Dimensional Fully Developed Turbulent Channel Flow," JFM, Vol 56, Part 3, pp 533-557 (1972).

21. Wilcox, D.C. and Alber, I.E., "A Turbulence Model for High Speed Flows," Proceedings of the 1972 Heat Transfer and Fluid Mechanics Institute, Stanford Univ Press, pp 231-252 (1972).

22. Thomann, H., "Effects of Streamwise Wall Curvature on Heat Transfer in a Turbulent Boundary Layer," JFM, Vol 33, Part 2, pp 283-292 (1968).

23. Sturek, W.B. and Danberg, J.E., "Experimental Measurements of the Supersonic Turbulent Boundary Layer in a Region of Moderate Adverse Pressure Gradient," AIAA Paper No 71-162, New York (1971).

24. Bissonnette, L.R. and Mellor, G.L., "Experiments on the Behavior of an Axisymmetric Turbulent Boundary Layer with a Sudden Circumferential Strain," JFM, Vol 63, Part 2, pp 369-413 (1974).